Novel Mixed-Field Neutron and Gamma Detector Development for Rock Formation Evaluation

James Greer

A thesis submitted in partial fulfilment of the requirements for the degree of Doctor of Philosophy at the University of Sheffield

Physics and Astronomy

July 2024

Abstract

Nuclear well logging employs high activity neutron sources downhole to bombard rock formations and measure the induced response. Common neutron sources in use include Americium-Beryllium (AmBe) and Californium-252, typically with activities in the giga and terabecquerel range. The presence of these high activity sources across logging sites all over the world is a concern for nuclear security and safeguarding, and a potential replacement is available in Deuterium-Tritium Pulsed Neutron Generators (D-T PNGs). These sources can be turned off when not in use, and also offer additional timing information due to their pulsed nature. This could provide improved detector capabilities when coupled with fast timing and position sensitive detectors. In this thesis, a low-cost, modular system is proposed that can measure the flux of thermal neutrons and gammas at various distances from the pulsed source. The detector modules consist of in-house manufactured plastic scintillator coupled to BN:ZnS(Ag) thermal neutron converter foils. Many detector designs are simulated for feasibility in GEANT4 optical simulations, and software tools were developed to predict readout pulses and evaluate expected figures of merit for PSD based on changing geometry and optical characteristics of detectors. These mixed-field detectors show good figure of merit for neutron-gamma discrimination at low-cost, allowing construction of positional and temporal distributions of detected neutrons and gammas when used as part of a multi-detector prototype tool. A prototype detector was constructed and tested within the University of Sheffield Neutron Facility with both radioisotope and DT neutron sources. Pulse shape discrimination algorithms were explored, along with pile-up mitigation techniques for the case of DT PNGs. The detector was finally tested using a mock rock test bench, with aims to test detector response to changes in surrounding moderator.

Declaration

I, the author, confirm that the Thesis is my own work. I am aware of the University's Guidance on the Use of Unfair Means (www.sheffield.ac.uk/ssid/unfair-means). This work has not been previously been presented for an award at this, or any other, university.

The simulations work performed in Chapters 3 and 4 was completed by me with support and guidance from Patrick Stowell and Lee Thompson. I designed the simulation geometries, performed the analyses, and collected data for necessary optical properties required for simulation. The GEANT4 wrapper package, CRESTA, developed by Patrick Stowell, Lee Thompson, and Chris Steer, was used for all simulations in this thesis. I personally wrote the PMT pulse generation software and associated PSD prediction code.

Chapter 5 details work on in-house manufacture of prototype plastic scintillators. This work, including scintillator mixing, casting, and testing, was performed by myself with significant inspiration and guidance from Sam Fargher and Patrick Stowell. This work also was made possible with the advice and equipment access granted by Andrew Parnell and other members of his group.

The construction, calibration, and characterisation of a prototype borehole detector in Chapter 6 was carried out by myself with support from Patrick Stowell and Robert Foster. The associated borehole testbench was simulated by myself, and constructed with help from several members of Sheffield's Neutrino Group, namely Patrick Stowell, Robert Foster, Steve Wilson, and Jack Fannon. Experimental testing and analysis of the detector with the pulsed neutron generator was performed by myself, with support and advice from Patrick Stowell.

This research was conducted under the supervision of Prof. Lee Thompson and Dr. Patrick Stowell at the University of Sheffield, and funded by the NuSec Nuclear Security Network, now the NTR Network.

Acknowledgements

Some time in 2019, during my undergraduate studies, I signed up to a project with Prof. Lee Thompson and Dr Patrick Stowell to design and build an IoT-enabled radiation waste bin. Little did they know at the time, Lee and Patrick would be stuck with me for a while. I cannot thank Lee and Patrick enough for their dedication and continued supervision right until the end - for Lee, even beyond his official retirement. This work absolutely would not have been possible without their support and infinite patience throughout. I also wish to thank Dr Tom Deakin of Lablogic Systems, for his invaluable insights and support over the course of both my PhD and previous projects.

I would also like to thank Sam Fargher and Andy Scarff. Sam, in the early days of my PhD, taught me to build my first muon detector with the added barrier of social distancing and COVID restrictions. Sam's 'FAFO' approach to science was ingrained in me early on in the first few months of my PhD, and helped with a great deal of the ideas in this thesis. Andy was always on hand to ensure both my safety and sanity, and was always somehow able to offer an instant solution to a problem I'd been stuck on for several weeks.

Rob, Jack, Steve, there is absolutely no way I would have made it this far without your help, ridicule, questionable humour, and aluminium-box-building skills. I owe you all many, many drinks.

And finally, a massive thank you to my family for all their support. Anna, you deserve several medals alone for listening to me talk depressingly about sand for hours on end. I would never have finished without you keeping me going. Thank you.

Contents

List of Acronyms

BGO Bismuth Germanate

PSD Pulse Shape Discrimination

OPEC Organization of the Petroleum Exporting Countries

NNSA National Nuclear Security Administration

WL Wireline Logging

LWD Logging While Drilling

NRC US Nuclear Regulatory Commission

EPA Environmental Protection Agency

DT Deuterium-Tritium

DD Deuterium-Deuterium

BN:ZnS Boron Nitride : Zinc Sulfide

PNG Pulsed Neutron Generator

RDD Radiological Dispersal Device

PNN Pulsed Neutron-Neutron

PNL Pulsed Neutron Lifetime

PPO 2,5-diphenyl-oxazole

POPOP 1,4-bis(5-phenyloxazol-2-yl) benzene

QE Quantum Efficiency

SPE Single Photoelectron

FRET Förster Resonance Energy Transfer

PMT Photomultiplier Tube

List of Figures

Chapter 1

Introduction

1.1 History of Oil and Gas Well Logging

1.1.1 Petroleum

Petroleum is generally used as an all encompassing term for crude oil and natural gas. It is composed primarily of hydrogen and carbon, with some trace amounts of sulphur, nitrogen and oxygen [1]. Hydrocarbon molecules of differing sizes and shapes compose crude oil and natural gas. These molecules may be straight chain, cyclic, saturated, or unsaturated, and crude oil is separated into these useful products using fractional distillation. The modern world is reliant on these products for all manner of purposes: from fuel to power motor vehicles and power stations, to products used in the manufacture of plastics, lubricants and solvents. Worldwide oil demand was forecast by the Organization of the Petroleum Exporting Countries (OPEC) in 2023 to reach 101.89 million barrels per day [2].

Oil and gas are present within pore-space in reservoir rocks. They are formed in a "source rock", deep in the subsurface, where organic matter is gradually converted into hydrocarbons under high temperature and pressure. The relative density of the oil and gas compared with water in the formation allows the hydrocarbons to migrate upwards, moving through pore space in the reservoir (usually made up of sandstone or limestone). The porosity of these rocks determines the quantity of fluid that can be present. This petroleum will continue to migrate until it encounters a trap, an impassable boundary which caps off the deposit (often shale or salt) [1]. Figure 1.1 shows this process and typical depths for formation of oil and gas.

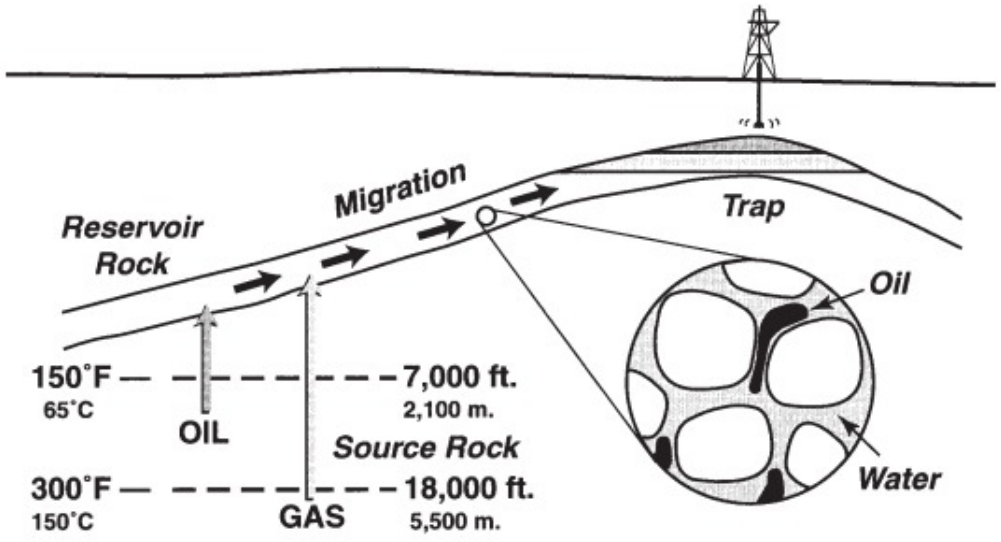

Figure 1.1: The formation and migration of oil from source rock to trap. Oil occupies small spaces in porous rocks. Taken from [1].

For the extraction of petroleum, a well is drilled into an area of oil or gas-bearing rock. The operators of such a well may drill in a known oil field, or they may choose to drill what is known as a "wildcat" or exploratory well [3]. A wildcat well is drilled in an area where little is known of the subsurface. Well-logging techniques can be used to better understand the rock surrounding both wildcat wells and wells in known oil-bearing regions. To extract commercially useful quantities of petroleum, it is necessary to have a thorough understanding of the subsurface and where oil-bearing formations may be present. To obtain this information, well operators measure the properties of the rocks using a combination of tools lowered into the borehole. This process is known as oil and gas well-logging.

1.1.2 Well-Logging

From its conception in 1927 [4], oil and gas well-logging has a long history as a technique for downhole geophysical evaluation. A well-log presents the characteristics of the surrounding rocks in a borehole as a function of depth. Characteristics measured depend upon the type of logging tool used. This can range from measurement of the conductivity of the rocks to the induced gamma response of the formation from intense neutron bombardment. The field of well-logging encompasses the use of all of these tools, and the resulting well-log is used to inform upon the likely

presence of hydrocarbon deposits for extraction.

The first oil well log was performed in 1927 by Henri Doll, the son-in-law of the eponymous Conrad Schlumberger [4], founder of Schlumberger Limited with his brother, Marcel. For years before this, the Schlumberger brothers had been investigating the electrical conductivity of ore-containing rocks for mineral prospecting. The earliest of these tests reportedly took place in Conrad's bathtub [5]. The ore-containing rocks had a lower resistivity, and the brothers considered that this technology could also be applied to fluids in the subsurface. Building upon the work of the Schlumberger brothers, Henri Doll lowered an electrical sonde (a logging tool) into an oil well in Pechelbronn, France [6]. The theory was that the electrical resistivity of the rock formation would vary according to the pore-occupying fluids present. For example, a saltwater-containing formation will record a low resistivity, due to the presence of conductive ions in the fluid. Conversely, a hydrocarbon containing formation will have a high resistivity [7]. Doll measured the resistivity at different depths in the well, plotting the results by hand. The result was the first well log (shown in Figure 1.2).

This spurred a revolution in the industry, which previously relied on core samples brought up to the surface, which were notoriously inconsistent in their predictions [4]. This led to the development of an entirely new field: oil and gas well-logging. Today, a whole suite of techniques are available to operators. The scope of this thesis will cover nuclear logging methods, specifically those employing neutron sources to elicit a response from the surrounding formation.

Nuclear methods were first employed in 1939, with the introduction of the gamma-ray log [8]. This was a novel and exciting technique, with unique advantages. Due to the penetrating nature of gamma radiation, this type of logging could occur in a cased hole. Casing is used to support the structure of the borehole, but prevents direct contact with the formation wall, which was necessary for electrical logging. Shales tend to be of higher natural radioactivity due to elevated levels of uranium, thorium, and potassium [9], which is not present in other typical rocks encountered in wells such as limestone and sandstone. These first sources logs measured the natural radioactivity of the surrounding rocks using Geiger-Muller tubes, identifying shale beds. As mentioned above, shales tend to form traps for oil and gas, and so their location is of great interest to geophysicists.

In 1941, nuclear logging went one step further when Bruno Pontecorvo proposed neutron-gamma logging. This work, borne from Italian nuclear research during the Second World War, measured the induced gamma radiation (from neutron captures)

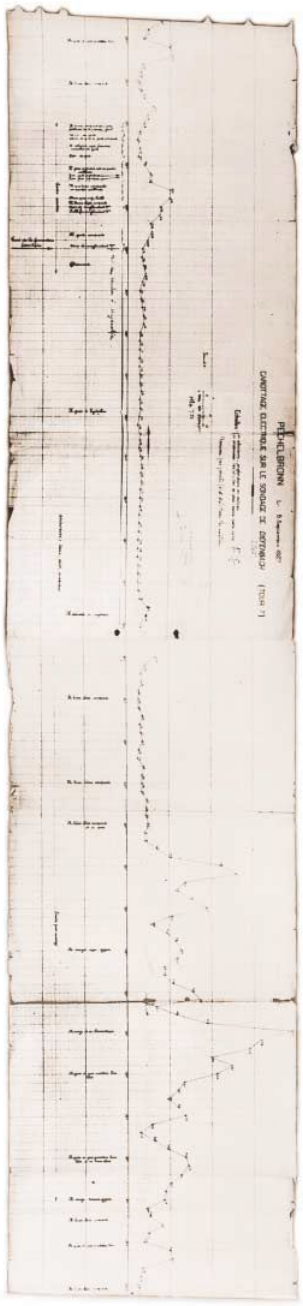

Figure 1.2: The first well log was a hand-plotted resistivity curve, taken by Henri Doll. Image from [5]

in the presence of an intense neutron source downhole (see Figure 2.5 for a cross-section of a source-detector setup downhole). The first reported tool used a Radium-Beryllium (RaBe) source. In his report to the Oil and Gas Journal in 1941 [10], Pontecorvo reported how neutron measurements could provide new information

based on the capture of neutrons on hydrogen, different from traditional gamma-ray logging. Again, due to the penetrating power of neutrons, cased holes were no issue. Further to this, the use of high activity radioisotope sources was considered an advantage for speeding up logging times. This was a key moment, as the first technique employing radioisotope sources downhole as part of logging tools. Neutron logs exploit interactions of emitted neutrons with hydrogen in the pore fluids. Neutrons interact with their surroundings via nuclear interactions [11]. This involves inelastic or elastic scattering, followed eventually by the capture of the neutron, and subsequent emission of other radiation. In well-logging, the detected radiation in the vicinity of the surrounding rock can inform upon the strata properties based upon these interactions (discussed in more detail in chapter 2). One of the main petrophysical quantities of interest for neutron logging is formation porosity, ϕ, defining the proportion of pore space to solid rock. Hydrogen is mainly present within the fluids occupying pore space within the surrounding geology. Neutrons predominantly lose energy from elastic collisions with hydrogen present within the formation. Therefore, a formation containing lots of hydrogen will thermalise and absorb neutrons more quickly, over a shorter distance, leading to lower count rates in detectors. Conversely, neutrons incident upon a formation with low porosity will encounter less hydrogen atoms, and will therefore lose less energy to elastic scattering on their path through the medium, travelling greater distances. This leads to higher count rates in detectors in the borehole further from the source. This can present as a change in the near-far detector count ratio, which is the commonly used metric in porosity logging tools. As a result, neutron logs are in general a good tracker of porosity [12][13]. Though further techniques are available with more complex methods employed, this is the basis for most neutron logging.

Epithermal neutrons have energies just above 0.025 eV. Though Figure 1.3 shows the epithermal neutron rate tracking porosity in the formation, it is also common to use thermal neutron detectors, or gamma detectors sensitive to induced capture gamma rays to track porosity. Other techniques employing neutron sources include sigma logging, which measures the macroscopic cross-section of the formation, and spectroscopic carbon-oxygen ratio logging. These spectroscopic measurements of inelastic neutron scatter gamma rays can inform on the relative proportion of carbon and oxygen in a well, providing details on the likely ratio of water to hydrocarbons. Overall, the field of neutron logging encompasses several techniques:

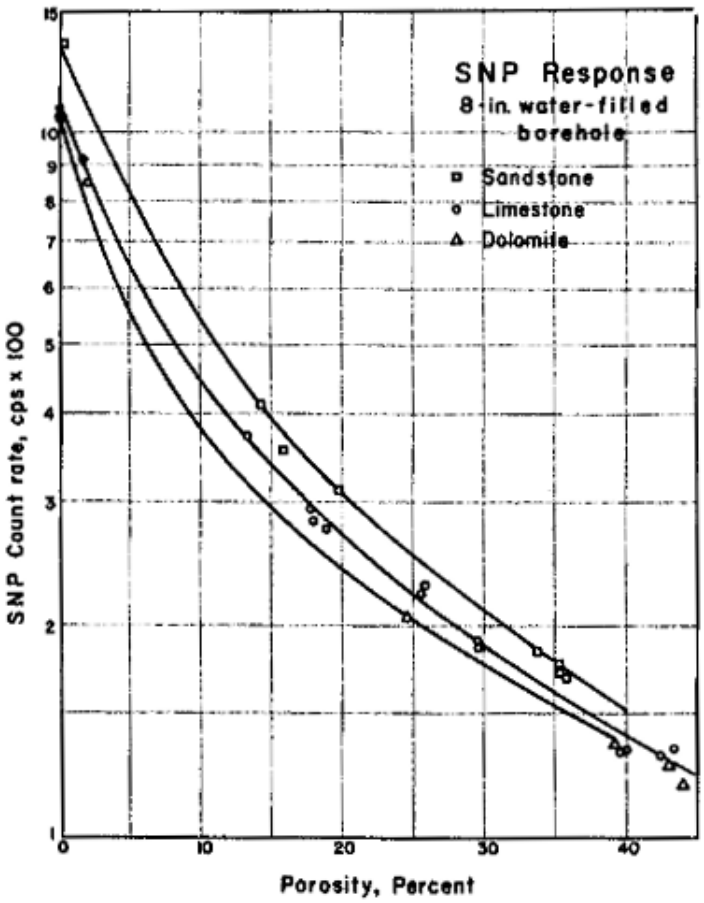

Figure 1.3: A curve from a sidewall neutron porosity tool shows epithermal neutron counts vs. porosity in different rock types. Image from [14]

- Porosity logging - Near-far detector count ratios are used as a measure of the amount of hydrogen in the formation, which is related to the fluid occupied pore space in the surrounding rocks.

- Gamma ray neutron tools for porosity logging may be employed which measure the capture gammas from hydrogen.

- Neutron-Gamma logging - employs spectroscopic techniques, in which scintillators are used to measure specific energy of emitted gammas after neutron bombardment. This technique may be used to measure inelastic or capture gammas from neutron interactions. This kind of measurement is useful for carbon-oxygen ratio measurements for example, which can be used to assist in the determination of relative quantities of hydrocarbons and water.

	WL	**LWD**
Detector Operation Temperature	75° – 175 °C	150° – 175 °C
Vibration level / acceleration	None	∼30 g RMS
Downhole pressure	∼690-2070 bar	<1380 bar
Operational time	∼10 hours (typ.)	Several hundred hours
Tool lifetime	10-15 years	∼1 year

Table 1.1: Reproduced from [16]. The different requirements of WL and LWD tools. In vibration, $g = 9.81 m/s^2$

- Sigma logging - Using a pulsed neutron source, macroscopic cross-section, or the sigma value of the formation, is measured and used as another property of interest for the surrounding rock formation.

Nuclear logging techniques are discussed in more detail in chapter 2.

1.1.3 Detectors: Current State of the Art and Issues

Due to ever-increasing demand for hydrocarbons, and the need to locate new oil-bearing reservoirs, deeper wells are becoming more common. In fact, in 2017, 52% of US oil production was from wells greater than 1.5 km depth [15]. With deeper wells, the conditions downhole become more hostile. The requirements for operation will differ depending upon the logging method. This is dictated by whether logging occurs in a pre-drilled well (known as Wireline Logging (WL)) or during drilling (known as Logging While Drilling (LWD)). LWD tools have to contend with particularly hostile environments, as they are mounted as part of a fully operational drilling tool.

Table 1.1 shows the extreme environments present in WL and LWD scenarios. These requirements limit the detector types available for use in nuclear well-logging detectors. Helium-3 based neutron detectors have long been the choice for well-logging applications. Helium-3 detectors present many desirable properties:

- High neutron efficiency
- Low gamma sensitivity and thus excellent gamma rejection
- Resistance to high temperatures
- Reliable over long operational period

Despite their excellent performance and suitability, Helium-3 detectors present an issue. Helium-3 is historically susceptible to massive disruptions in supply [17], leading to huge price premiums. Some logging tools have in recent years deployed Lithium glass detectors as an alternative (see chapter 2), however their reliability has been called into question. Lithium glass has been found to show highly variable response across batches [16], a significant drop in light output at high temperatures [18], and is also sensitive to gammas. For these reasons, further alternatives are sought by the industry. There is a clear demand for alternative methods of neutron detection suitable for downhole deployment.

1.1.4 Incidents involving Radioisotope Sources

Radioisotope sources in the oil industry present a unique set of risks. With many radioisotope sources across hundreds of well sites, these sources are liable to loss or theft. Furthermore, with sources used commonly in the Giga or Terabequerel range, high radiation doses to operators are possible as a result of improper handling procedures, accidents, or even theft.

Source Abandonment Downhole

Well-logging requires the deployment of long toolheads in deep, narrow boreholes. In such a situation, it is possible for the toolhead to become stuck downhole, and in many cases, this has occurred with sources mounted. Procedure dictates that if attempts fail to retrieve the tool from downhole, the well must be plugged, and a plaque placed at the site of abandonment to warn others of potential dangers. An example of one of these warning plaque is shown in Figure 1.4. The US Nuclear Regulatory Commission (NRC) keeps records of incidents involving radioisotope sources. The following source abandonments are a small selection of those recorded in [19] unless otherwise referenced:

- 2017, Halliburton Energy Services abandoned a stuck logging tool containing a 555 GBq AmBe source and a 74 GBq Cs-137 source in North Slope Borough, Alaska, at a depth of around 12400 feet. Well was plugged with cement at 11300 feet.
- 2017, Halliburton Energy Services abandoned a tool containing four sources including three Cs-137 sources of 65.86 GBq, 18.5 kBq, and 59.2 kBq, along

with a 555 GBq AmBe source, in Kern County, California. A plaque with details of the sources present was erected atop the well.

- 2017, Schlumberger Technology Corporation abandoned a 65.86 GBq Cs-137 source, along with a 677.1 MBq Cf-252 source, in Escambia County. Attempts to retrieve the source, known as "fishing operations", failed, with the sources then cemented in place. Plaque placed at well site.

- 2014, Baker Hughes abandonment of two sources, a 185 GBq AmBe and a 92.5 GBq Cs-137 in an offshore well near Louisiana. Plugs and additional protections for mechanical deflection [1] placed in well.

- 2003, Schlumberger report the abandonment of three sources, at a depth of 12600 feet. The sources included two 592 GBq AmBe sources and a 62.9 GBq Cs-137 source. A cement plug and plaque were placed at the well site.

These cases show just a few of the many sources lost downhole over the years. Though the loss of sources downhole is concerning, if sufficient protections are in place, further contamination from a logging source is unlikely. There may be some concern if a well is re-entered in the future that a drilling tool could strike the source, penetrating its casing. If the resulting radioactive material released was then able to reach the surface, this could result in exposure to workers. During drilling, a heavy drilling mud is pumped into the well for two key reasons:

1. Cycling mud from the drill bit and up to the surface allows drilled material to be carried away from the drill head, preventing blockages.

2. The high pressure of the drilling mud equalises the pressure between the borehole and the subsurface rocks containing oil, gas, or water.

The potential for an uncontrolled flow of material from the subsurface could in the worst case scenario lead to a so-called blowout, such as the infamous Deepwater Horizon disaster of 2010 [20].

One way that radioactive exposure could potentially occur is through the movement of contaminated drilling mud (from a breached source) up to the surface. A risk analysis of this case was performed in [21], arriving at a worst case scenario of 1.3 person-rem [2]

[1] Mechanical deflection apparatus typically means any barriers placed around the source to deflect drill bits from hitting the source

[2] A person-rem is an older unit defined by the average dose per person, multiplied by the number of people exposed [22]. 1 Sievert is equivalent to 100 rem.

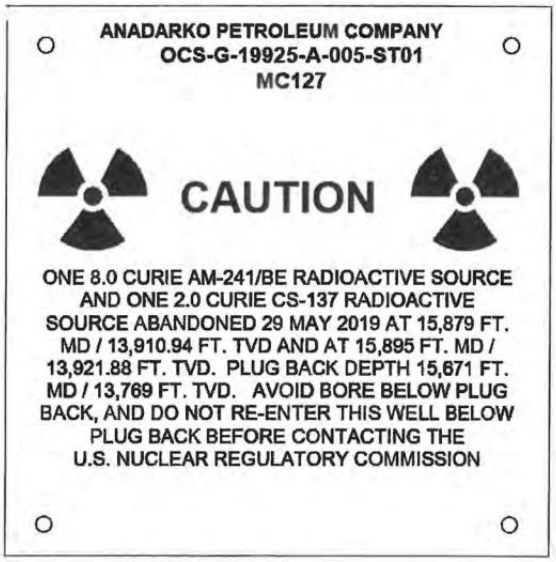

Figure 1.4: An example of a source abandonment plaque erected at a well site in the case of a source lost downhole [23]

Theft or Loss of Radioisotope Sources

Theft of radioisotope sources is another concern of national security agencies. A source could be stolen by parties with intent to cause harm through deployment of a dirty bomb, though in what appears to be most recorded cases, these sources have often been stolen by accident in attempts to steal other equipment.

- 2017, Roke Technologies report the theft, and the subsequent recovery, of two 111 GBq AmBe sources from their storage area in Kern County, California, along with a 1100 kg water calibration tank. Locks had been cut, and the sources were removed and discarded close to the site. It was determined that the person responsible did not know they were radioisotope sources.

- 2012, Halliburton Energy Services reported the loss of a 555 GBq AmBe source. After using the source for logging activities in Pecos, Texas, the team left the site and travelled 130 miles to Odessa, Texas. Upon their arrival, they found the source missing. After searching the original well site to no avail, Halliburton arranged search teams along the route between sites. Daily searches were sent out, including military and Environmental Protection Agency (EPA) support. The source was found almost one month later by a member of the public, 8 miles from the well site in a different direction to that travelled by the logging team.

No explanation was found for how this had occurred. The member of the public received a 0.518 mSv full body dose and 9.72 mSv extremity dose.

- Referred to in [24]. In India, 1993, two AmBe sources (685 MBq and 18.5 GBq) and one Cs-137 source (55 GBq) were stolen following a dispute between staff and management. Searches failed for the stolen sources, until police located those responsible. It was discovered that the sources had been thrown into a local river. The sources were located, but it was deemed impossible to safely retrieve them from the riverbed. An embankment was created to cover the sources. Concluded with a total cost of $100,000 to the company responsible.

- More recently in January 2023, in a case that caught a lot of media attention, a Cs-137 source was lost in transit over a 1400 km journey in Western Australia. The 6×8 mm, 19 GBq source was used in mining operations by the Rio Tinto Group, and was transported from the mine on the 12th January to Perth, arriving on the 16th January. 9 days passed before the source was found to be missing. Public health warnings were then issued [25]. The source was found on 1st February, 2 metres from the side of the road, by a search team using radiation detectors on a vehicle travelling at 70 km/h. Australian Prime Minister Anthony Albanese expressed that the maximum penalties for companies who had lost dangerous radioactive material ($1000) was "ridiculously low" [26].

The above case studies present a concerning trend in the loss of radioisotope sources, however in most cases, these sources are found due to their high activities. For Deuterium-Tritium (DT) Pulsed Neutron Generator (PNG)s, which do not emit when powered down, this presents an interesting issue. When they are lost, it can be very difficult to locate them. In one particular case in 2008, a Baker Hughes truck containing four neutron generators and one 3.7 GBq Cs-137 source was stolen from outside a hotel in Texas. The empty truck was recovered 10 days later. The Cs-137 source was later recovered, but the neutron generators were never found [19]. Whilst this is a concern, in order for the neutron generators to be of danger to the public, they must be turned on by a skilled operator; they are not constantly producing neutron radiation. The primary danger of a lost source is that it may be found by a member of the public who does not know of the inherent dangers. The person may then go on to expose themselves and others to the radioactive source. In the case of a lost neutron generator, there would be no immediate radiation exposure.

Radiation Exposure

With the presence of radioisotope sources onsite, there is inevitably exposure to workers. With the correct procedures and monitoring, such exposure can easily be kept to an acceptable level. However in cases where operators may be less prudent with safety measures, exposure can reach dangerous levels:

- In 2014 it was discovered that a member of staff at Pioneer Wireline Services had been handling logging sources by hand, culminating in an annual whole body dose of 51.22 mSv in 2013. For comparison the annual effective dose limit for an adult in the UK is 20 mSv [27]. Following interviews with other staff, handling sources without the necessary tools was found to be common practice.

- In [28], the loss of control of a Cs-137 logging source is outlined, leading to the exposure of several workers to radiation. Following logging activities, a source had been left in the logging tool, and not returned to its shielded container. The source was only discovered to be missing two days after this, by which point workers on the rig floor (many of which were not radiation workers) had been exposed.

These examples of exposure to radioisotope sources were the result of negligence and improper respect for necessary protocols. Improved education of staff around the potential dangers of ionising radiation could reduce such incidents. Despite this, the presence of constantly emitting radioisotope sources at well sites will always carry an inherent risk. As an alternative, the industry could look to different sources such as electrical neutron generators. In order for this switch to occur, these sources must provide a tangible benefit to industry. Important issues to industry include cost, reliability, and capability to provide the same or improved data. One challenge in providing the same data is the different energy spectrum of the sources used. For example, porosity response from a DT PNG (emitting 14.1 MeV monoenergetic neutrons), will produce a much different (and worse) near-far detector response to an AmBe source, with a neutron spectrum of average energy $\approx$ 4.2 MeV. However, the DT source has other advantages in that it provides neutrons of high enough energy to make carbon-oxygen ratio measurements from inelastic scatter. The proposal to move to DT PNG sources for more measurement types is therefore a careful balance of cost and safety factors, along with the capability to make measurements of many different properties.

1.2 Neutron Source Replacement in Formation Evaluation

Well-logging is demonstrably an invaluable tool for oilfield operators. To reliably perform neutron well-logs, a reliable, robust neutron source is required for the hostile borehole environment. Sealed radioisotope sources have long been the standard for neutron logging due to their reliability; a radioisotope source will emit neutrons without any interruption or breakdown. This is very important in the oil and gas industry to prevent costly delays in formation evaluation. However the use of high activity neutron sources is not without its disadvantages, namely safety and security risks. An alternative technology that shows potential for neutron well-logging is pulsed electrical neutron sources. This technology could answer some of the issues which are present with the use of sealed radioisotope sources, but further development is required in order to encourage wider adoption of these sources.

The presence of a large number of highly active radioisotope sources at well sites is a constant source of concern for nuclear security agencies. Though there is a low likelihood of their use for terrorism, the potential fallout from such an incident would be severe. The fear for logging sources is their potential for use in a Radiological Dispersal Device (RDD), more commonly known as a "dirty bomb". Dispersal of radioactive material could cause mass panic, danger to public health, and significant long-term decontamination costs [29]. AmBe sources used in neutron well-logging are of particular concern due to their Americium-241 content. Being an alpha emitter, Americium-241 would be highly hazardous if inhaled. In addition, it would be difficult to monitor contamination due to the short range of its emitted radiation in air. An example of typical well logging sources is shown in 1.2

In addition to the threat of terrorism, radioisotope sources pose other complicated issues:

- Exposure of workers onsite to neutron radiation.
- Potential for loss of sources downhole
- Cost and availability

PNGs are electrical neutron sources, producing a flux through the fusion of nuclei. Currently available as DT or Deuterium-Deuterium (DD) based tubes, these sources answer some of the key drawbacks of radioisotope sources:

Radiation Type	Neutron Source
Measurement	Porosity
Standard Activity	Up to 20 Ci (740 GBq)
Nominal Output	2.2 x 10^6 neutrons/s per Ci
Average Energy	4.2 MeV
Half-Life	432 years
Neutron Dose Rate	2.2-2.7 mrem/hr at 1 m/Ci 0.59-0.73 μSv/hr at 1 m/GBq
Gamma Dose Rate	2.5 mrem/hr/ at 1 m/Ci 0.68 μSv/hr/ at 1 m/GBq
Recommended Working Life	15 years

Table 1.2: Data from QSA Global [30] on their available range of AmBe neutron sources for oil and gas well logging

- Operator safety: These sources can be switched off, preventing unwanted exposure of operators to neutron radiation
- National security: If lost, these sources cannot be repurposed into a dirty bomb, and would require specialist expertise to use for nefarious means

However, there are still concerns:

- Cost: Electrical neutron sources are a relatively new technology, and their lifetime and purchase price may prevent adoption by industry.
- Reliability: A radioisotope source is simple by comparison, and always emitting. These sources are naturally robust in the harsh borehole environment, and these sources will not fail on the drilling line. There are more points of failure with electrical neutron generators.
- Data: Due to different neutron source energy, the data from these logs presents differently to historical AmBe logs, on account of the different neutron source spectrum .

Table 1.3 summarises these key issues.

Alternative neutron sources have been considered for porosity measurements in other studies, such as by Frankle and Dale in [31]. D-T was found to show the worst sensitivity to porosity, in a setup tallying the near and far detector counts. No timing information was used for porosity estimation. A shielded D-T source was also used in attempts

to modify the source spectrum with little success. D-D source neutrons showed the best sensitivity, higher even than AmBe. The relative sensitivity of these alternative sources is shown in Figure 1.5. However D-D sources do not provide the threshold energy for inelastic gamma emission used in C/O ratio calculation. C/O ratio is the ratio of carbon and oxygen in the surrounding rock. This is useful to determine the relative proportion of hydrocarbon and water downhole. D-T neutrons were found to produce the fastest C/O ratio measurement time, but as mentioned, their performance for porosity measurement is severely lacking. Interestingly, T-T fusion neutrons perform reasonably well in both categories, but it is mentioned that commercial production of such generators is not currently at the level of D-T or D-D. Badruzzaman also mentions the low neutron output of current T-T systems [32]. In [33], another simulation study was performed in MCNP to investigate porosity responses of different sources. Again, D-D showed the highest sensitivity to porosity, with the main drawback being the relatively low flux of D-D sources compared with D-T or AmBe. Chen also discusses the need for alternative neutron detection technology, with the rising costs of Helium-3. In [32], Badruzzaman discusses how D-T generators can provide multiple types of measurement in the same tool (C/O ratio and porosity), which is not possible with other electrical sources.

In January 2018, industry representatives met with NuSec and AWE at a workshop held to discuss alternative technologies for radiation sources in the energy industry [34]. Those present included BP, NNSA, GE-Baker, Halliburton, and Schlumberger. The 2018 workshop was held to develop roadmaps for alternative technologies, paving the way for the replacement of worrisome radioisotope sources. Despite some of the discussed disadvantages with neutron generators, the safety and security benefits (along with potential informational benefits) were considered significant enough that further adoption of PNGs is a worthy technical challenge.

This work will aim to explore the timing distribution of neutron and gamma detector hits as an additional parameter sensitive to formation porosity using a pulsed DT source. Measurements of this type are only possible when using pulsed neutron sources. Timing information from pulsed neutron sources is already widely used in sigma logging. This work aims to explore the more specific case of hydrogen content prediction with low-cost detectors. Low-cost mixed-field detector designs will be investigated using PSD methods. Simulations will be used to explore potential geometries before construction of a prototype. In addition to this, along with the simulation of potential testbenches, this work will attempt testing in a purpose built test bench at the University of Sheffield's

Pulsed Neutron Facility. The work will focus particularly on low-cost detectors for this purpose to offset the high cost of D-T generators. Replacement of existing Helium-3 detectors in logging systems every year leads to very high costs. A potential alternative, low-cost system for neutron detection may be available using an optical readout based detector using solid scintillators as an alternative to high-cost gas detectors. Ruggedized Photomultiplier Tube (PMT) based detectors are already well established in the well-logging industry [35].

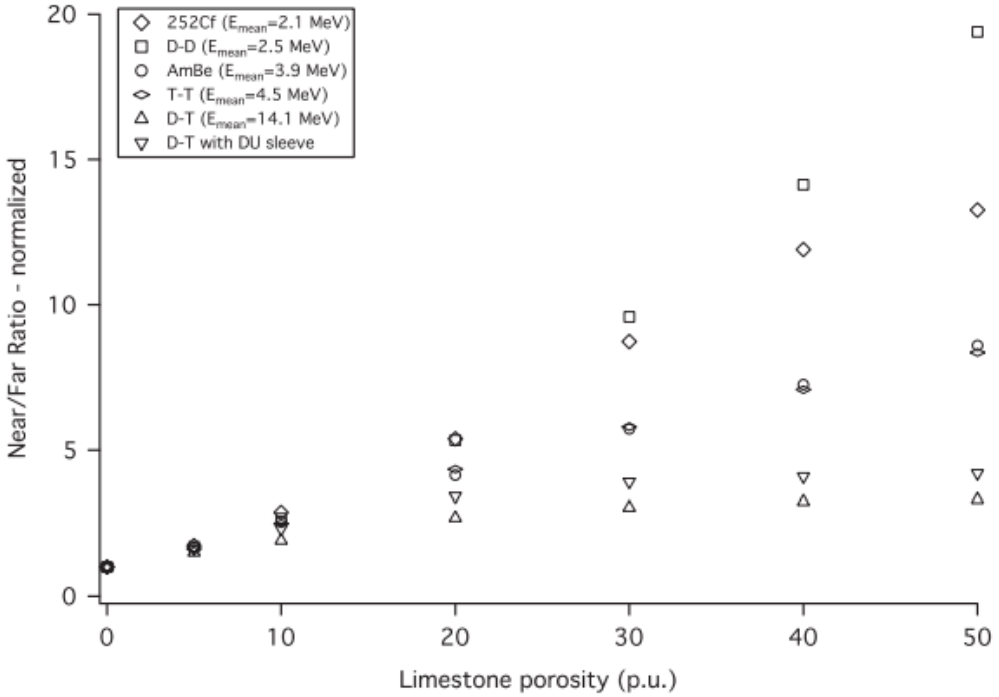

Figure 1.5: Simulated near-far detector count ratio for different logging sources in limestone of varying porosity. Image taken from [31]

	Radioisotope Source	**Electrical Pulsed Sources**
Operator Safety	Always emitting, constant controls required	Can be turned off when not in use, reducing unnecessary exposure
Nuclear Security	Dirty bomb threat	Difficult to repurpose for nefarious means
Emission mode	Constant	Tuneable pulse rate
Cost	Variable - AmBe (100k$ for 590GBq, 740 GBq is over $150k [36])	$100 - 400$k$ ($10^8 - 10^{10} n/s$) [36]
Lifetime	AmBe recommended 15 year lifetime [37]	Typically 1000 hours [38]
Operation	Simple, load into tool, constantly emitting	Requires skilled operator
Reliability	Unmatched	Redundancy required in case of equipment failure

Table 1.3: Key differences in the use of radioisotope and pulsed electrical sources for well-logging.

1.3 Aims of the Thesis

As has been discussed, high activity radioisotope sources are a cause for concern in the nuclear security sector. In addition, they provide a health and safety risk for operators working in close vicinity to logging tools, and an environmental concern for sources lost downhole. Continuous monitoring of risk, and the threat of fines, exposes the industry to high financial liabilities. Therefore, this work will explore the adoption of alternative sources, namely Deuterium-Tritium Pulsed Neutron Generators (D-T PNGs). It will examine the feasiblity of DT based tools for neutron-logging, and the design of lower-cost detectors to offset the expense of DT PNGs.

As discussed, He-3 detectors are currently the industry standard (discussed in 2) but issues with supply and cost necessitate the development of suitable alternatives. This work investigates a low-cost alternative, which could also potentially be used in applications beyond borehole logging where mixed-field sensing is desired (nuclear security, dosimetry etc). A lower-cost detector may also offset some of the costs of a more expensive neutron generator source. The following thesis will investigate mixed-field (neutron and gamma) detectors based on plastic scintillator coupled Boron Nitride : Zinc Sulfide (BN:ZnS), investigating the detector response for different geometries. In chapter 4 the effects on Pulse Shape Discrimination (PSD) will be explored within the context of design for borehole geometries. Simulation tools will be developed to assist in the prediction of PSD performance for proposed detector geometries, which will inform the construction of the prototype detector designs in later chapters.

Part of this project required prototyping unconventional geometries and as a result, this work also investigated the in-house manufacture of custom scintillator using low cost epoxy base materials (discussed in 4). This work aimed to develop a procedure for low-cost, fast prototyping of plastic scintillators for detector development projects, in this case for the testing of borehole detector geometries. Temperature constraints are an obvious issue with the deployment of plastics downhole, but the recent development of new polymers and elastomers [39][40][41] alleviates some of these concerns. Therefore research into mixed-field detection systems incorporating organic scintillators is particularly relevant with upcoming developments in the area of polymer and materials physics. The work in this thesis explores detector designs with currently available commercial scintillators suitable up to around 80 °C. Though this work will consider the coupling of organic scintillators to neutron converter foils, it was considered that inorganic scintillators may offer

additional information on account of their energy resolution. Sodium iodide detectors would be unsuitable for this application, as they require encapsulation, however crystals such as Bismuth Germanate (BGO) may be ideal. On account of their relatively high cost when compared with plastic scintillators, this was considered at cross purposes to the low-cost detector development in this work. For example, a 40 mm by 50 mm BGO crystal costs in the region of $2000 [42]. Considering a multi-module detector, this price multiplies accordingly. Nevertheless, for a mixed-field detector requiring good energy resolution and neutron sensitivity, exploration of this combination may be of interest in future work. In this work, however, the focus is on low-cost detector development with plastic scintillators coupled to neutron converter foils. This is a novel approach, with most converter foil based detectors usually coupled to wavelength shifters rather than scintillator.

One of the key goals of this work is to build a low-cost prototype neutron tool, sensitive to the hydrogen content of a test formation, using low-cost detectors. Possibilities will be explored to exploit any additional timing information from DT PNGs to improve the sensitivity of the detector. This part of the work involves the design and simulation of a small-scale mock rock testbench, which is simulated in chapter 3 and tested with a prototype in chapter 6. The project explores the sensitivities of the tool within this testbench, constructed at the University of Sheffield's Pulsed Neutron Facility.

Chapter 2

Theory

This chapter outlines general theory on the detection of neutron and gamma radiation, along with applications in neutron and gamma well-logging techniques.

2.1 Neutron Interactions

Neutrons, having zero charge, interact via the strong force with nuclei. Depending upon the neutron's energy, it will interact via three key mechanisms:

- Elastic Scattering
- Inelastic Scattering
- Capture

The interactions that will occur are highly dependent upon the energy of the neutron incident upon the nucleus. Thermal neutron energies have a Maxwell-Boltzmann distribution with an average kinetic energy of kT, which at room temperature equates to 0.025 eV [43]. Epithermal neutrons exist at energies between a few to 100s of eV. A neutron above 100 keV is generally considered as a "fast" neutron. It is worth noting that these boundaries are general and there are many interpretations of their concrete limits. The method of interaction is dictated by the cross-section for a particular interaction, which is a function of energy and is dependent upon the target nucleus.

In elastic or inelastic scattering, a neutron scatters on a nucleus, which recoils in response. In the elastic case, the recoiling nucleus gains all of the energy lost by the

neutron in the collision. In the inelastic case, some energy may be emitted by an excited recoil nucleus as a gamma ray. In capture reactions, a neutron is absorbed by a nucleus instead, forming a new compound nucleus which may go on to decay into charged products. These capture reactions are particularly useful in neutron detection, as the charged products often deposit their energy over a short distance in detectors. This section will explore some theory behind cross-sections, along with examples of the above interaction types.

2.1.1 Neutron Cross-Sections

The microscopic cross-section, σ, for neutron interactions is an energy dependent quantity which differs across nuclei and interaction types. Usually given in terms of barns (10^{-28}m^2), it determines the probability of an interaction. This description of neutron interactions is based upon the effective interaction area of target nuclei.

To understand cross-sections, consider a thin target material of area A and thickness δx, with an incident neutron beam of density n and velocity v. The nuclei density in the target is given as N.

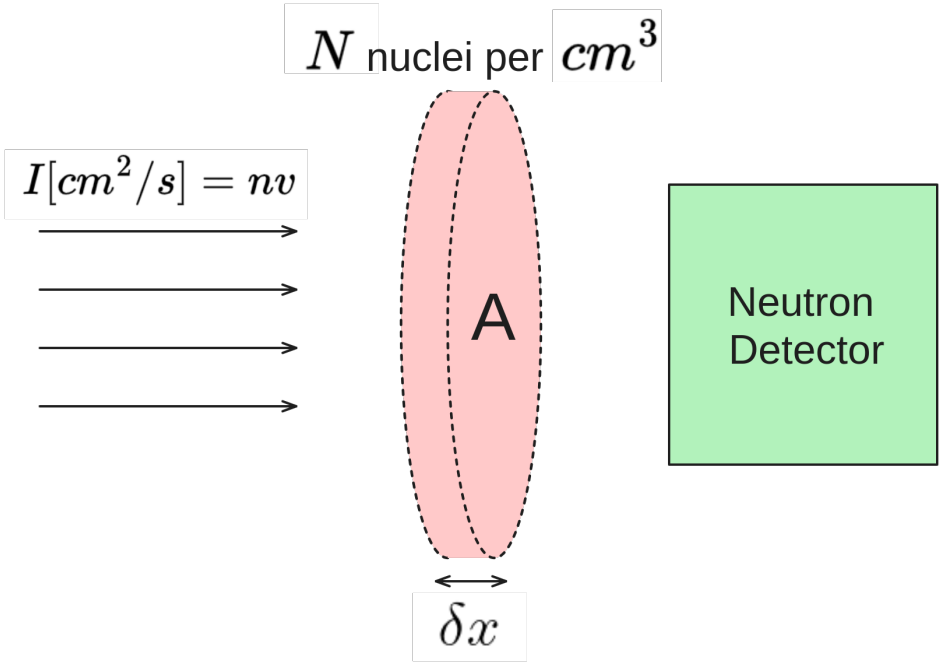

Figure 2.1: The interaction of a beam of neutrons with a thin slice of nuclei.

The reaction rate R can be considered proportional to the quantities as follows in Equation 2.1.

$$R \propto A \cdot \delta x \cdot n \cdot v \cdot N \tag{2.1}$$

Adding a constant of proportionality σ:

$$R = \sigma \cdot A \cdot \delta x \cdot n \cdot v \cdot N \tag{2.2}$$

It is then possible to simplify further, and express a reaction rate density in terms of these quantities. The volume of the target is $A\delta x$, and the reaction rate density can be expressed in units of reactions per cm^3 per s.

$$R' = \frac{R}{V} = N \cdot v \cdot n \cdot \sigma \tag{2.3}$$

Then it is possible to rearrange for σ and determine the units of cross-section, cm^2.

$$\sigma = \frac{R'}{n \cdot v \cdot N} \tag{2.4}$$

The intensity of the incident neutron beam can be written as $I = n \cdot v$, and so simplifying further:

$$\sigma = \frac{R'}{I \cdot N} \tag{2.5}$$

Therefore the microscopic cross-section σ can be defined as "the reaction rate density per unit beam intensity per nucleus in the target per unit volume" [44]. Different types of neutron reaction are given different cross-sections, denoted by a subscript on the cross-section, such as σ_{el} or σ_{in} for elastic and inelastic scatter respectively. The total cross-section can be calculated simply as the sum of all relevant reactions available. An example cross-section plot is shown for Helium-3 in Figure 2.2, showing the contributions from different interactions to the overall cross-section [45].

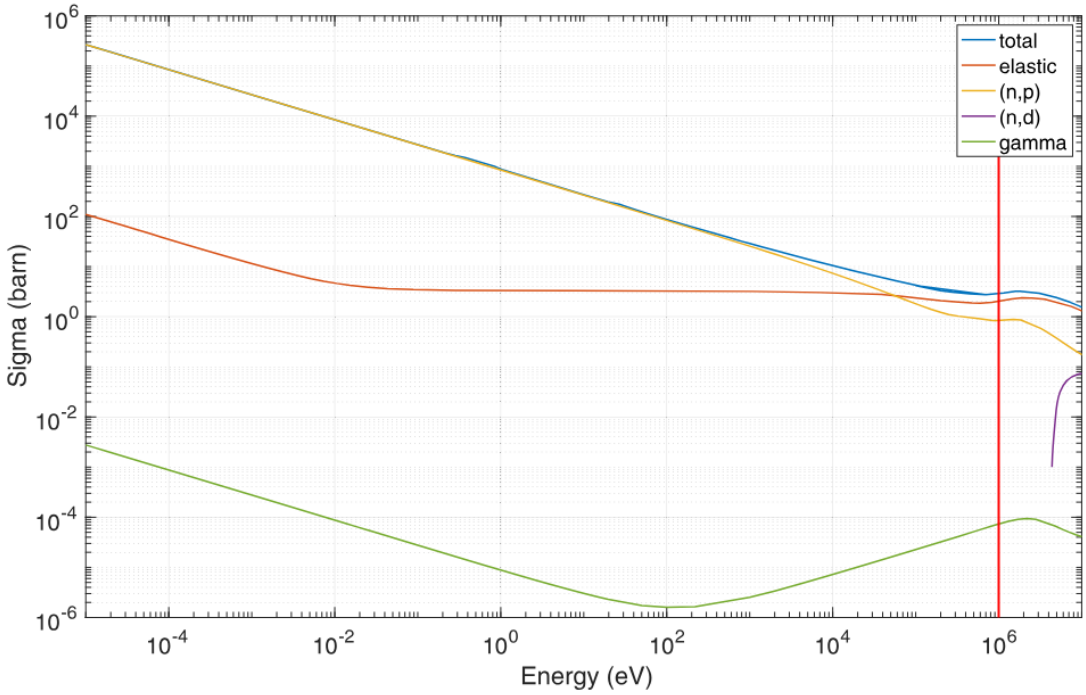

Figure 2.2: The contributions to total cross-section from different neutron interactions with Helium-3. The (n,d) reaction has little contribution due to its 4 MeV threshold. Image from [45].

2.1.2 Elastic Scattering

Neutrons can undergo elastic scattering on nuclides, in which the total energy lost by the neutron is transferred to the recoil nucleus. This is perhaps the most important interaction for neutron well-logging. The most efficient energy loss occurs when a neutron collides with a target of similar mass. The energy loss for a particle scattered at an angle θ is described as in Equation 2.6.

$$\frac{Q_{max}}{E_n} = \frac{4Mm}{(M+m)^2}\cos^2(\theta) \tag{2.6}$$

Q_{max} is defined as the energy transferred to the recoil nucleus, with m and M the neutron and target masses respectively. E_n is the energy of the incident neutron.

Equation 2.7 shows the maximum fractional energy loss for head-on collisions of a neutron (mass M) colliding elastically with a nucleus of mass m [46].

$$\frac{Q_{max}}{E_n} = \frac{4Mm}{(M+m)^2} \tag{2.7}$$

Clearly, for the case in which $M = m$, this energy loss is at a maximum, and so collisions on hydrogen nuclei are most efficient for slowing neutrons via elastic scatter. Table 2.1 shows the typical energy loss fractions for head-on elastic scattering from common isotopes.

Nucleus	Q_{max}/E_n
$^{1}_{1}\mathrm{H}$	1.000
$^{12}_{6}\mathrm{C}$	0.284
$^{16}_{8}\mathrm{O}$	0.221

Table 2.1: Energy loss fractions for elastic neutron scatter on common isotopes.

For this reason, hydrogenous material is often used as neutron moderator, for slowing fast neutrons down to thermal energies. In the context of well-logging, the elastic scattering of neutrons on hydrogen creates a diffuse cloud of thermal neutrons around the detector and in the surrounding rock. These interactions and the resulting thermal neutron distribution are used to infer the quantity of hydrogen present in a well through the deployment of downhole detectors.

2.1.3 Inelastic Scattering

In the case of fast neutrons of high enough energy, inelastic scattering can occur in which a neutron excites a recoiling nucleus in a collision. This results in a promptly emitted gamma ray during de-excitation, with the incident neutron losing energy both as emitted radiation, and to the recoiling nucleus.

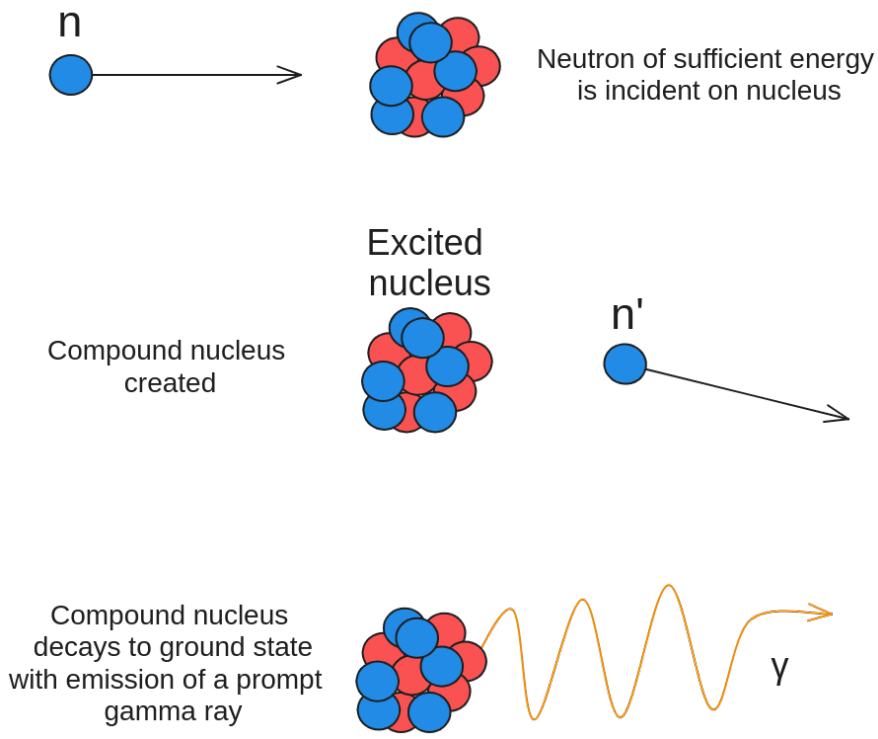

Figure 2.3: The inelastic scattering process. An incident fast neutron of sufficient energy can excite a recoil nucleus such that it emits a gamma ray of characteristic energy. This means that the final state recoiling particles contain less kinetic energy than the incident neutron.

Below the threshold for inelastic scattering, only elastic scattering may occur. Additionally, and important to note for the applications in this thesis, inelastic scattering cannot occur on hydrogen. Having only a single proton in its nucleus, no excited states exist and so only elastic scattering is possible [47]. However in larger nuclei, inelastic scattering can produce characteristic gammas useful for non-destructive analysis. For example, inelastic neutron scattering from carbon produces gamma rays of 4.43 MeV. The same process yields 6.13 MeV gammas from oxygen [48]. Spectroscopic gamma measurement can therefore yield a ratio of the presence of these two elements within a sample. In addition, another type of inelastic neutron scattering may occur in which a proton is removed from the nucleus, possible due to the incident neutron energy being greater than the binding energy of the nucleons.

2.1.4 Neutron Capture

The dominant process for slower/thermal neutrons involves a nucleus capturing a neutron to form an unstable compound nucleus, which subsequently decays, releasing further radiation. These radiative decays may involve emission of gamma-rays of characteristic energy, useful in elemental analysis [49]. In other instances, decays may involve charged products, such as the $B^{10}(n,\alpha)Li^7$ capture reaction, in which boron captures a neutron and after the formation of a compound nucleus releases an alpha particle and a lithium-7 nucleus. These heavy, charged products deposit their energy in a very short distance, and such decays are convenient for applications in slow neutron detectors, as well as in boron neutron capture therapy (BNCT), where damage to surrounding tissue can be minimised [50]. Figure 2.4 shows a selection of cross-sections for capture reactions across a variety of nuclei used in neutron detectors. Gadolinium has a notably high capture cross-section, but rather than short-range capture products, it instead produces a gamma shower, which may be unsuitable for some small form factor neutron detectors. The collection of these factors must be considered in the selection of neutron-sensitive components of neutron detectors.

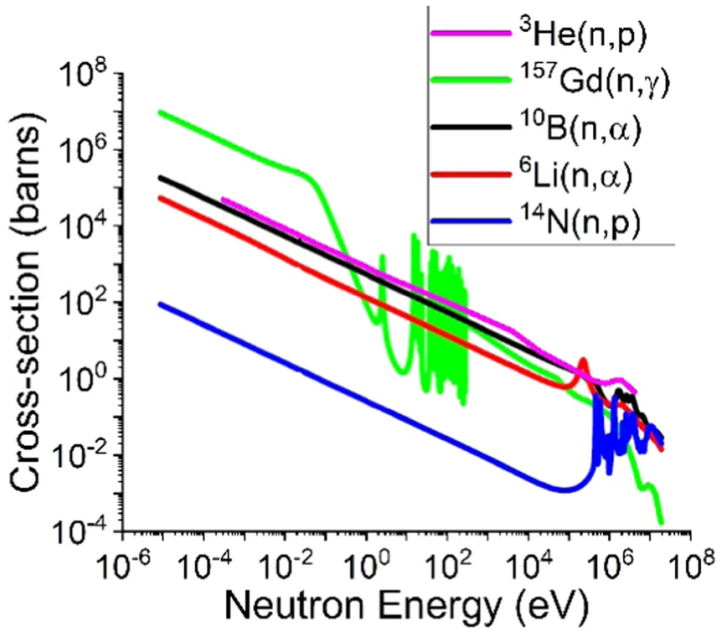

Figure 2.4: Relative cross-sections for a selection of different capture reactions. Image from [51]

2.2 Neutron Logging Methods

The discussed neutron interactions are used in well-logging to interrogate the rock strata in oil wells to yield information on their composition. There are a number of methods used that employ neutrons, and the following section outlines the main techniques used.

2.2.1 Porosity Well-Logging

As discussed, petroleum is present within the pore space in rocks. Therefore, measuring the porosity of the formation rock is important to understand the quantity of fluids present. Porosity is the volumetric ratio of pore space to solid rock within a formation. In porosity measurements, the pores are generally assumed to be completely filled with formation fluids. The slowing down of source neutrons occurs mainly on hydrogen, and so the distribution of neutrons in a downhole detector near a source can be used to inform upon the quantity of hydrogen present. The hydrogen content measured can then (through the use of lithology-dependent calibrations) be used to determine the porosity. A detector in a formation of high porosity will likely contain more hydrogen, and slow down neutrons quickly, before they are then captured. This results in low count rates in detectors. Conversely, for a formation of relatively low porosity, there is less hydrogen present, and so neutrons are able to travel further before they are captured. It is these effects that are exploited in porosity logging tools. Detector calibration is required to get a measurement in porosity units. Calibration assumes completely water-filled pores. Porosity logging tools are usually composed of multiple detectors measuring the neutron population at different positions in the borehole. This multiple detector technique is referred to as compensated neutron logging, and stems from the use of neutron diffusion theory. Neutron diffusion theory states that as a reasonable approximation, the ratio of detector hits at distances r_1 and r_2 is described by 2.8, where L_s is the neutron slowing down length, and K_1 is a calibration constant [52],

$$\frac{\phi_{r_1}}{\phi_{r_2}} = K_1 . \exp\left(\frac{r_1 - r_2}{L_s}\right) \tag{2.8}$$

Figure 2.5 shows the typical setup of a compensated neutron logging tool.

This technique is used to reduce the dependence on inconsistencies in borehole size, along with attenuation from borehole fluids, which would have to be accounted for in single detectors, as used in the very first neutron logging tools. Another method of

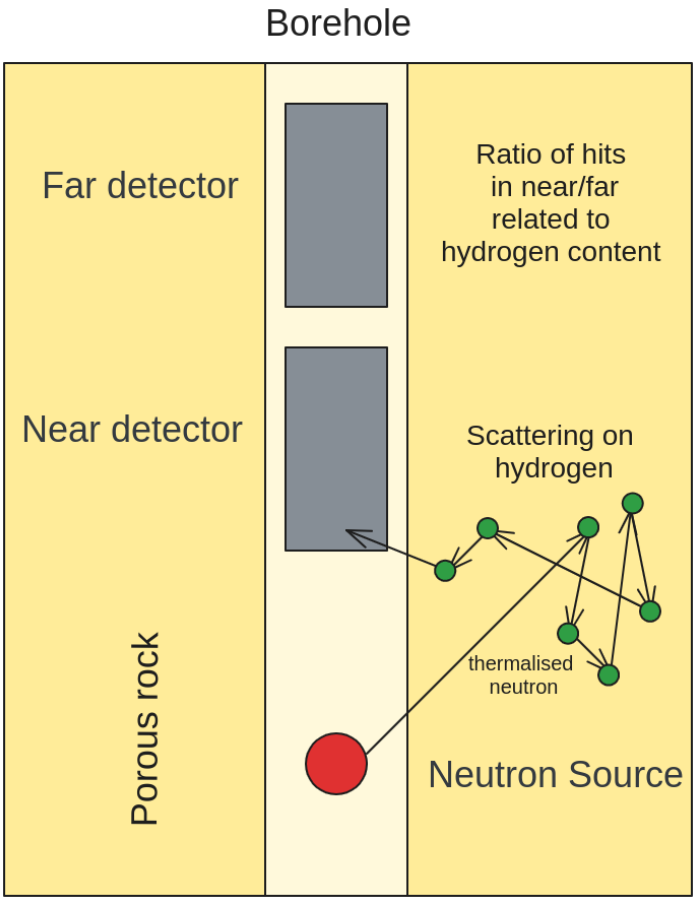

Figure 2.5: A borehole cross-section with a neutron porosity tool containing a near and a far detector. Neutrons interact with the formation fluids and are thermalised, and then detected or captured by the formation.

countering these effects is the use of sidewall neutron porosity measurements. These tools require an uncased, open hole, and press the detector against the borehole wall using a caliper arm. Roughly drilled boreholes can cause problems for these kinds of tools [53]

2.2.2 Sigma Logging

Sigma logs are named for the macroscopic cross-section of the formation, Σ, which is measured by observing the die-off time of the neutron pulse, as neutrons are captured by the surrounding material. Sigma logging measurements are a technique used as part of a pulsed neutron generator system, and are used in wells of high salinity to distinguish saltwater from hydrocarbons [54]. This is possible due to the high chlorine

content, a strong neutron absorber, in high salinity wells. These tools are less useful in wells of low salinity, as hydrocarbons and fresh water have very similar values for Σ, but tools will still respond to the hydrogen content in the well. These tools may operate by detecting neutrons, in Pulsed Neutron-Neutron (PNN) tools, or gammas, in Pulsed Neutron Lifetime (PNL) tools, between neutron pulses. PNN systems tend to have a more accurate response in low salinity and porosity wells, due to higher neutron count rates (less absorption) [55]. However, in situations with more neutron capture (higher salinity/porosity), it may improve counting statistics to measure the emitted gamma rays instead.

2.2.3 Carbon-Oxygen Ratio Logging

Another use of pulsed neutron generators in well-logging is as part of a Carbon-Oxygen logging [56]. The Carbon-Oxygen ratio is of interest to well operators, as it serves as a useful indicator of the relative proportion of hydrocarbons (containing carbon) to water (containing oxygen) in a well. In Carbon-Oxygen logging, inelastic gamma rays are induced by neutron bombardment. These inelastic gamma rays are detected using scintillators with good energy resolution, and the pulses collected used to build an energy spectrum. Pulsed neutron sources can be used in order to leverage the timing information to improve the resolution of the collected spectrum [57]. Different neutron interactions occur on different time frames, and so the gamma rays emitted are detected at different times. Detector systems can therefore using timing gates or event timestamps to separate an inelastic neutron scatter gamma spectrum from a capture gamma ray spectrum.

2.3 Neutron Detection Techniques

2.3.1 He-3 Proportional Counters

The historical gold standard of thermal neutron detectors is the Helium-3 proportional counter. Proportional counters use gas multiplication. By this method, the products from He-3 neutron capture are able to elicit an amplified charge response by application of an electric field. It is then possible to discern individual neutron capture events as measurable charge pulses.

Helium-3 tubes exploit the thermal neutron capture reaction:

$$^{3}_{2}\mathrm{He} + ^{1}_{0}\mathrm{n}\,(\mathrm{thermal}) \rightarrow ^{1}_{1}\mathrm{H} + ^{3}_{1}\mathrm{H} + 764\,\mathrm{keV}$$

The cross-section for thermal neutron capture on Helium-3 is 5330 barns. Reaction products are emitted back-to-back, with a combined energy of 764 keV. The stopping distance of the proton and triton released by this reaction can in some cases reach the walls of the tube, giving rise to the aptly named "wall effect". In these cases, full energy deposition of the capture products is not possible, leading to sharp walls in the spectrum. This effect is visible in both the diagram and spectrum in Figure 2.6.

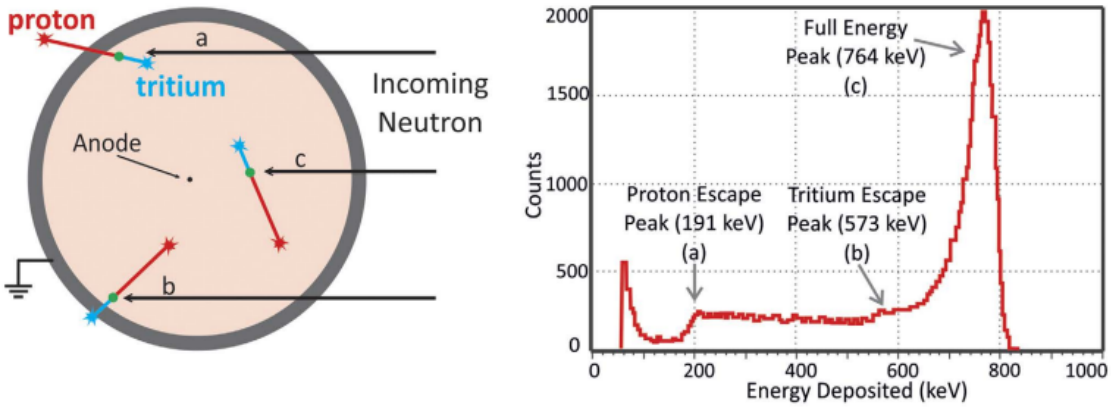

Figure 2.6: A cross-section of a He-3 tube showing three cases of neutron capture (left), along with an associated spectrum. Image taken from [58]

Helium-3 detectors are also suitable for operation at high temperature, making them an ideal candidate for oil and gas well-logging tools. Despite this, there are issues with Helium-3, and alternative detection technologies would be welcomed by both the logging industry and other industries requiring Helium-3 which have no other alternatives. Overall, the main issue is cost, which is closely related to the historical supply volatility.

Supply Volatility and Cost

Helium-3 is produced in industrial quantities as a byproduct of tritium production. Tritium decays into Helium-3 with a half-life of 12.3 years [59]. It is a byproduct of nuclear weapons manufacturing, and as such, its production and auction is highly regulated. In the US, Helium-3 is auctioned by the DOE from stockpiles generated by the National Nuclear Security Administration (NNSA). Before the September 11 attacks, the He-3 supply was sufficient to meet demands. In the post-9/11 world,

concerns against the smuggling of radiological materials led to the deployment of He-3 based neutron detectors at the US border, spiking demand [17]. This spike in demand also coincided with the winding down in nuclear weapons production, and with it, the production of Helium-3.

At an AAAS workshop in 2013 [60], the oil and gas industry, along with national security applications, were highlighted as two key areas where alternative neutron detectors could feasibly replace Helium-3 and ease demand. For medical imaging applications, another big consumer of Helium-3, there are no known replacements. Therefore neutron detection is a sector under significant pressure to move towards more sustainable alternatives.

2.3.2 BF_3 Tubes

Boron Trifluoride Proportional counters have the same method of operation as Helium-3 tubes but with an alternative gas fill.

$$^{10}\mathrm{B} + {}^{1}_{0}\mathrm{n}\,(\mathrm{thermal}) \rightarrow {}^{7}\mathrm{Li} + {}^{4}_{2}\mathrm{He} + 2.31\,\mathrm{MeV}\,(93\,\%)$$
$$^{10}\mathrm{B} + {}^{1}_{0}\mathrm{n}\,(\mathrm{thermal}) \rightarrow {}^{7}\mathrm{Li} + {}^{4}_{2}\mathrm{He} + 2.79\,\mathrm{MeV}\,(7\,\%)$$

Boron-10 has a thermal neutron cross section of 3840 barns, around 72% that of Helium-3. Natural unenriched boron is also just 20% Boron-10, and so natural boron has a cross-section of just 14.4% that of Helium-3. Boron-based detectors are therefore inherently less sensitive unless this difference in cross-section is accounted for through the addition of further capture material. These tubes can also be provided with enriched boron-10 content to improve efficiency [61].

One advantage of boron-based detectors is the large Q-value from capture reactions, improving discrimination between neutron capture events and gamma backgrounds.

2.3.3 Lithium Glass Detectors

The first neutron detectors made from glass scintillators were reported in 1957, and were made from borate and phosphate glasses [62]. Since then, further developments in glass detectors have led to the development of lithium-based glass detectors coupled to photodetectors such as PMTs for thermal neutron detection. These detectors utilise the lithium thermal neutron capture reaction:

	GS10	**GS20**	**GS30**
Overall Lithium Content	6.6%	6.6%	6.6%
Li-6 enrichment	Natural ∼5%	95%	0.01% (Depleted)

Table 2.2: Different lithium isotope loadings for Scintacor glass product range.

$$^{6}\mathrm{Li} + {}^{1}_{0}\mathrm{n}\,(\mathrm{thermal}) \rightarrow {}^{3}\mathrm{H} + {}^{4}_{2}\mathrm{He} + 4.78\,\mathrm{MeV}$$

Glass detectors are suitable for high temperature applications, making them an ideal candidate for the oil and gas industry to rival He-3 tubes.

Scintacor [63], one of the primary suppliers of lithium glass detectors, produce GS20® glass, which has gained in popularity over recent years, particularly for use in the oil and gas industry. The geometry of lithium glasses is particularly interesting, as they are designed in hollow cylinders. GS20® contains 6.6% lithium doping, isotopically enriched to 95% ^{6}Li. This ensures high thermal neutron efficiency in just a few mm of glass. In order to improve gamma rejection, the centre of the cylinder is removed to reduce gamma interactions in the bulk scintillator.

Scintacor also provides a variety of glasses with different specifications and levels of lithium-6 enrichment, visible in Table 2.2. Notably, they provide glasses almost entirely depleted of Li-6 for reference measurements.

2.3.4 Pulse Shape Discrimination for Neutron Detection

Pulse Shape Discrimination exploits the contrasting time profiles of light emission from the interactions of different particles. Different interactions can deposit differing amounts of energy, and produce varying pulse shapes. Digital signal processing of these pulses can then be used to discriminate between interacting particles.

Long-Short Gate Integration

One option available for the discrimination of pulses with large differences in area is using a charge integration approach. This method integrates from the start of the pulse to a predetermined short gate limit. A second integral is then calculated from the start of the pulse to a longer gate limit. The ratio of these two values can be used to quantify the emission profile of the event. An event with a long decay tail will show a characteristically higher long/short ratio. This ratio is used as a metric for particle discrimination.

$$PSD = \frac{\int_0^L V(t)dt}{\int_0^S V(t)dt} = \frac{Q_L}{Q_S} \tag{2.9}$$

The PSD parameter in Equation 2.9 is the specific metric used to distinguish between a neutron and gamma event. In this instance, it is defined as the ratio of the integrals of pre-defined long and short time intervals in a pulse.

$V(t)$ denotes the voltage pulse from the PMT, and L, S, the time limits of the long and short gates respectively.

$$FoM = \frac{PSD(\text{Neutron}) - PSD(\text{Gamma})}{FWHM(\text{Neutron}) + FWHM(\text{Gamma})} \tag{2.10}$$

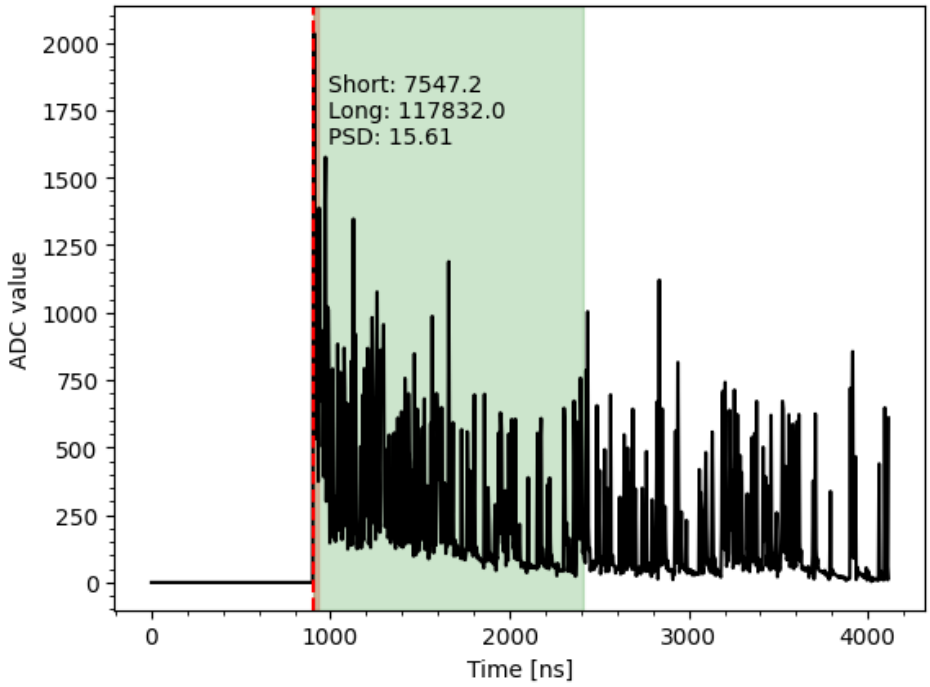

Figure 2.7: An example neutron pulse from a PMT with a BN:ZnS(Ag) foil placed directly on the glass face. Red dashed line indicates start trigger - defined either as the maximum sample value or the first point above a threshold. Red/Green shaded regions are short/long gates respectively. The short gate is 30ns, and the long gate 1500ns.

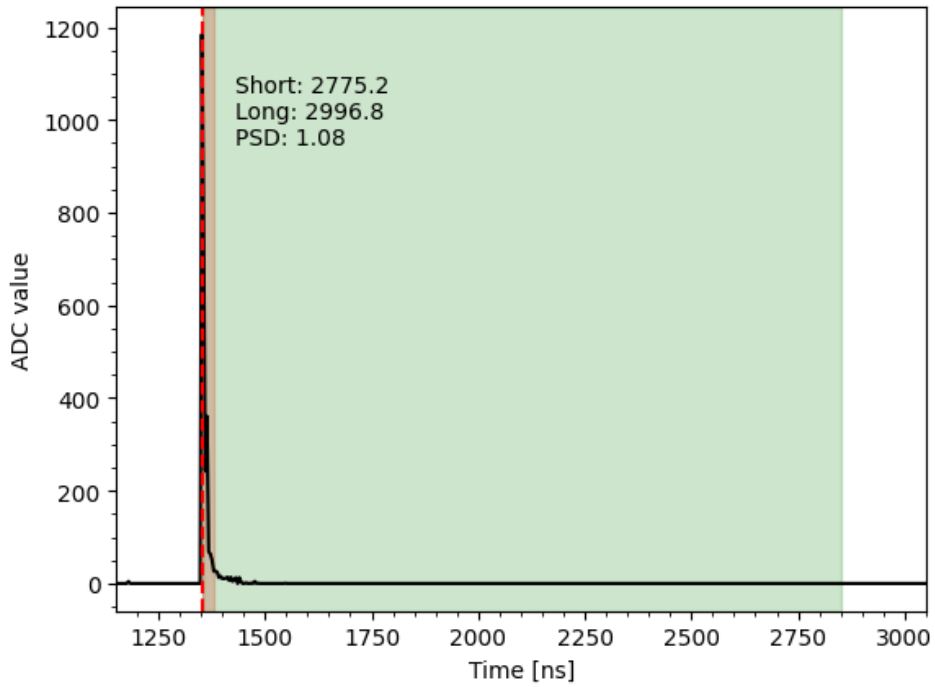

Figure 2.8: An example gamma pulse, with a PSD ratio much closer to unity. Note that the time range of this pulse is different than in Figure 2.7 and so the short gate region is more clearly visible.

Figure 2.7 shows how selecting appropriate time gates can yield significantly different areas, providing a good metric to distinguish a neutron pulse from a gamma pulse, such as in Figure 2.8.

A histogram of PSD parameters can then be used to observe distinct populations of neutrons and gammas, allowing for discrimination based upon pulse characteristics. The shape of this distribution will vary significantly dependent upon the detector used. To quantify the quality of discrimination between two gaussian neutron and gamma populations, a figure of merit is used such as that in Equation 2.10.

Time Over Threshold Approach

It is also possible to use the time-over-threshold as a metric for PSD. Trivially, it measures the total time spent in the pulse over a pre-defined threshold, and is simple to implement.

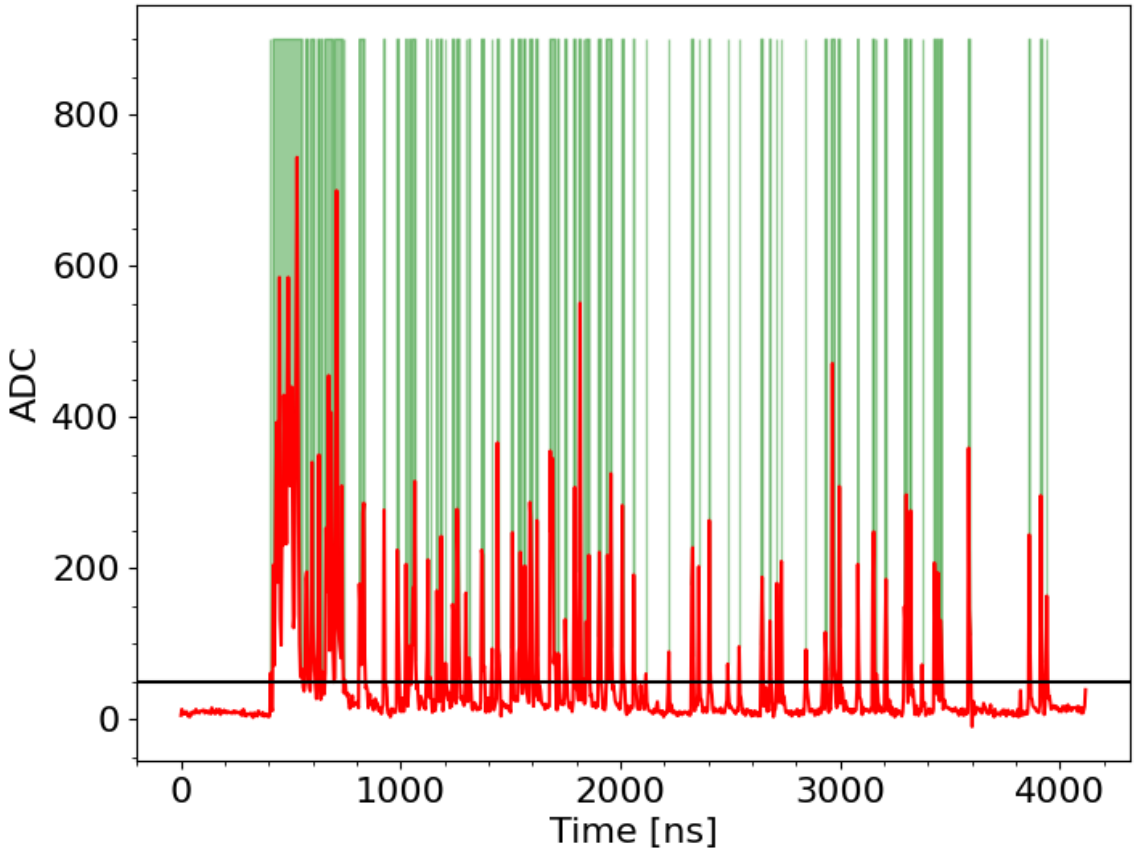

Figure 2.9: Green zones show where pulse was above threshold. Total width of green zone is time-over-threshold.

Peak Counting Approach

In some circumstances it may be more appropriate to deploy a peak counting approach. Though unsuitable for some types of detector with simple exponential decay tails, peak counting can work very well for long pulse trains such as those observed in ZnS emission profiles, as in Figure 2.7. This approach involves counting the peaks according to a set of conditions on threshold and prominence. A long, pulse train event from a BN:ZnS(Ag) foil will have many peaks, compared to a single peak for a gamma.

2.3.5 PSD in Scintillators

Neutron detection is also possible using plastic scintillators designed specifically to allow for PSD. One example is EJ-276 by Eljen [64]. These scintillators are neutron

and gamma sensitive and require pulse processing to separate particle populations based on different decay times for different interactions. These decay times are a product of the concentration of different excitation states resulting from interactions with higher or lower mass charged particles. For fast neutrons, detection is via proton recoil interactions, or in the case of thermal neutrons, the scintillator will usually be doped with a high capture cross-section nucleus. In addition to organic scintillators, some inorganic scintillators have been developed with mixed-field detection in mind. These inorganic scintillators retain excellent energy resolution for gamma spectroscopy while also exhibiting sensitivity to neutrons through addition of capture material. One such example is $Cs_2LiLa(Br, Cl)_6$, or CLLBC [65]. Due to the excellent energy resolution in these scintillators, the capture neutrons appear as a discrete patch in the PSD spectrum, as opposed to a drawn out band as seen in other PSD-based neutron detectors. Other examples include CLYC [66] and NaIL [67] scintillators.

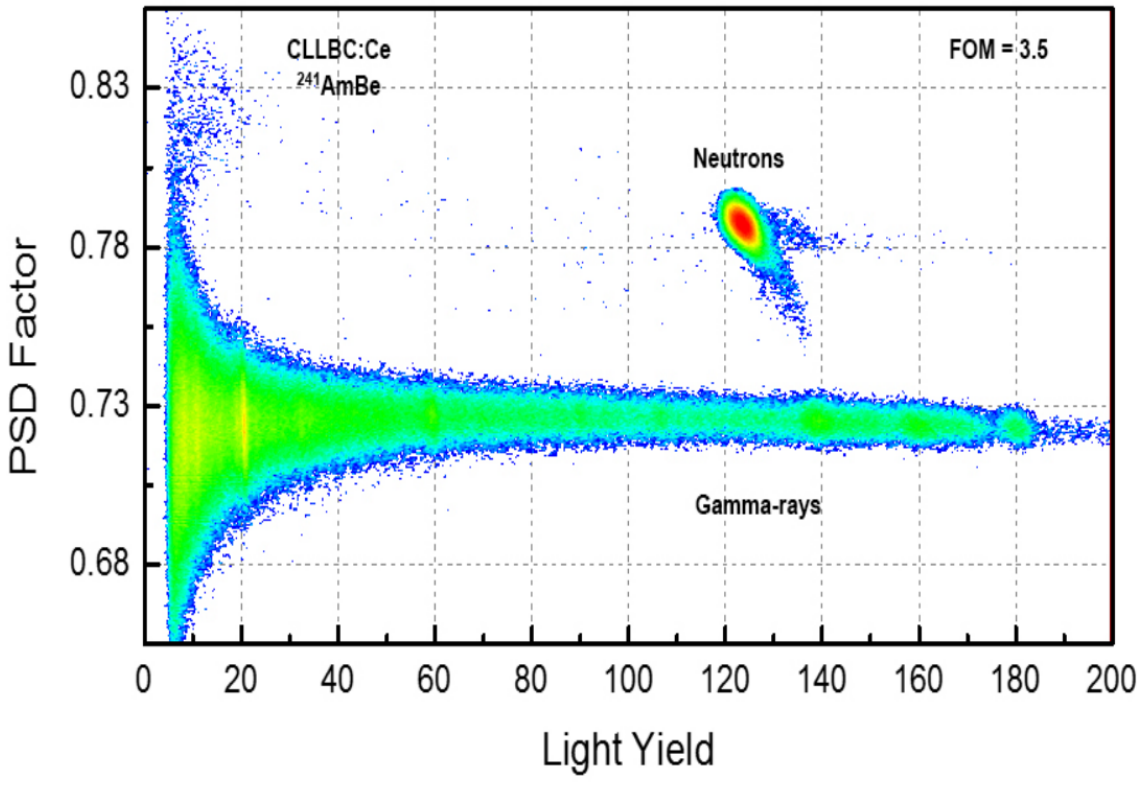

Figure 2.10: PSD distribution for CLLBC crystal. Image from RMD datasheets [65].

2.3.6 Thermal Neutron Converter Foils

Converter foils are the chosen detection method in this thesis, on account of their low-cost, ease-of-manufacture, and high light output for PSD. Converter foils are scintillation detectors which combine a neutron capture agent and a scintillating powder. This mixture is then combined with a binder material, usually some form of transparent epoxy or silicone, and coated onto a substrate. The converter foil can then be coupled directly or indirectly (via a wavelength shifter) to a photosensor.

Zinc Sulfide (ZnS) is an ideal scintillating powder of choice for this application. ZnS has excellent light output (300% relative to anthracene [68]), but cannot be used as bulk scintillator due to its opacity to its own scintillation light. However, in a thin layer, it is suitable to capture the full energy of charged products from neutron capture reactions, such as lithium-6 and boron-10. This provides a long characteristic pulse with high light output. Being so thin, converter foils intrinsically have very low gamma sensitivity, since gammas cannot deposit a significant amount of energy in the scintillator. This further assists in pulse shape discrimination.

The optimal ratio of capture agent to scintillator should ensure that each nucleus responsible for a capture is well surrounded by scintillator grains. Studies to determine this ideal ratio in [69] found the mass ratio to be 1:3 to 1:4 for lithium-based foils. In work by Marsden [70], it was found that on account of the shorter path length of capture products from boron-10, a small grain size of boron-10 is particularly important, with a mixing ratio of 1:3 most ideal. This is to ensure that capture products can escape the boron grains, and deposit energy in the surrounding scintillator, as in Figure 2.11.

If foils were coupled directly to photosensors, the detector area would be limited to the aperture of the photosensor used. In order to extend the effective area of foil-based detectors, they are often coupled to wavelength-shifting guides. In doing this, light from a large area of foil can enter a wavelength-shifter, and be guided towards a photosensor.

The choice of capture compound is highly dependent upon application. For low-cost detectors, boron based capture compounds (commonly BN) are usually the choice. However in cases where superior light output is desired, lithium based compounds (usually LiF) are preferred due to the higher Q-value of the lithium capture reaction. Table 2.3 compares these two candidates for converter foil capture compounds. Note the significant price difference for the two compounds. Lithium Fluoride for neutron detectors usually requires lithium-6 enrichment. This is also subject to additional export restrictions, which is not the case with boron nitride.

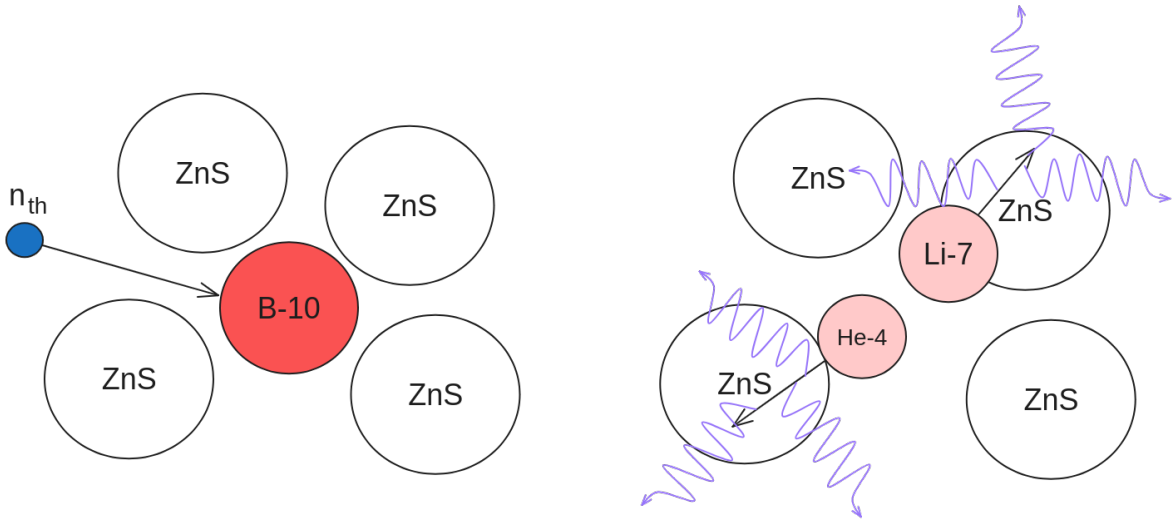

Figure 2.11: Method of detection for thermal neutron converter foils. Boron captures a neutron, before emission of capture products which deposit their energy over a short distance in surrounding ZnS scintillator.

	Boron-10 (BN)	**Lithium-6 (LiF)**
Thermal cross-section (barns)	3838	940
Natural Isotopic Abundance	19.9%	7.4%
Reaction Q-value (MeV)	2.31 (93%) or 2.78 (7%)	4.78
Price per gram	£0.56 (unenriched BN) [71]	£14.50 (95% enriched LiF) [72]

Table 2.3: Comparison of boron-10 and lithium-6 for neutron detector applications.

2.4 Gamma Ray Interactions

Gamma rays can interact with matter by several mechanisms. The mechanism of interaction is dependent upon the energy of the photon, as well as the atomic number of the medium. Understanding of these mechanisms and their dependence is crucial to detector design.

2.4.1 Compton Scattering

Compton scattering occurs when an incoming photon is scattered by an electron in the interaction medium.

The energy loss can be described by Equation 2.11 [11]. E' denotes the energy of the gamma ray after scattering. θ is the scattering angle, m_0 is the rest mass of the electron, and c the speed of light in a vacuum.

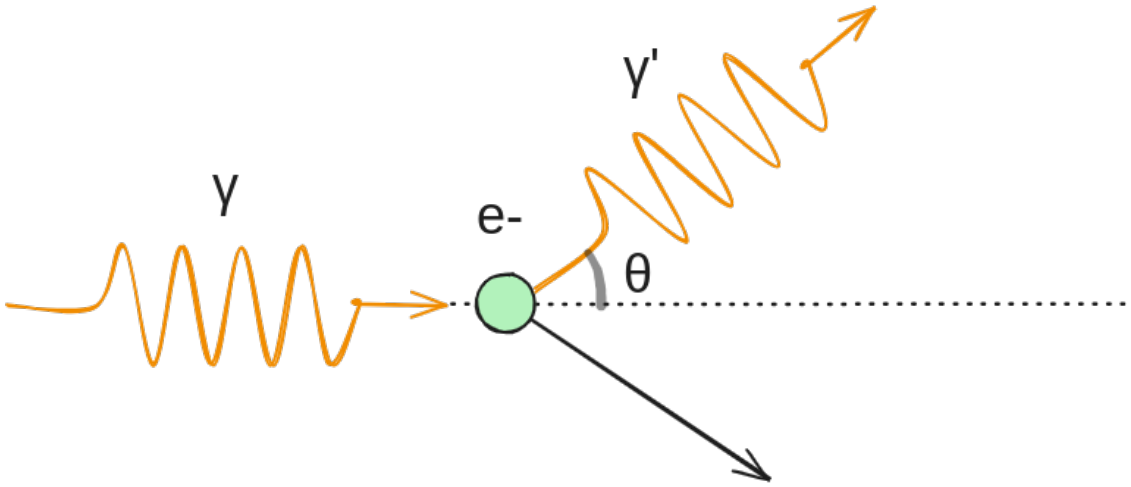

Figure 2.12: Compton Scattering: An incident photon scatters off an electron, resulting in an energy loss from the photon and an energy gain for the electron

$$E' = \frac{E}{1 + (E/m_0c^2)(1 - cos\theta)} \tag{2.11}$$

Compton scattering is the dominant mechanism of interaction for gammas in organic scintillators. Recoil electrons are able to deposit their energy in the scintillator, and due to the relationship in Equation 2.11, Compton scattering gives rise to a characteristic Compton continuum and edge. The continuum runs from the extreme cases of Equation 2.11, with $\theta = 0, \pi$. An example of such a continuum is shown in Figure 2.13.

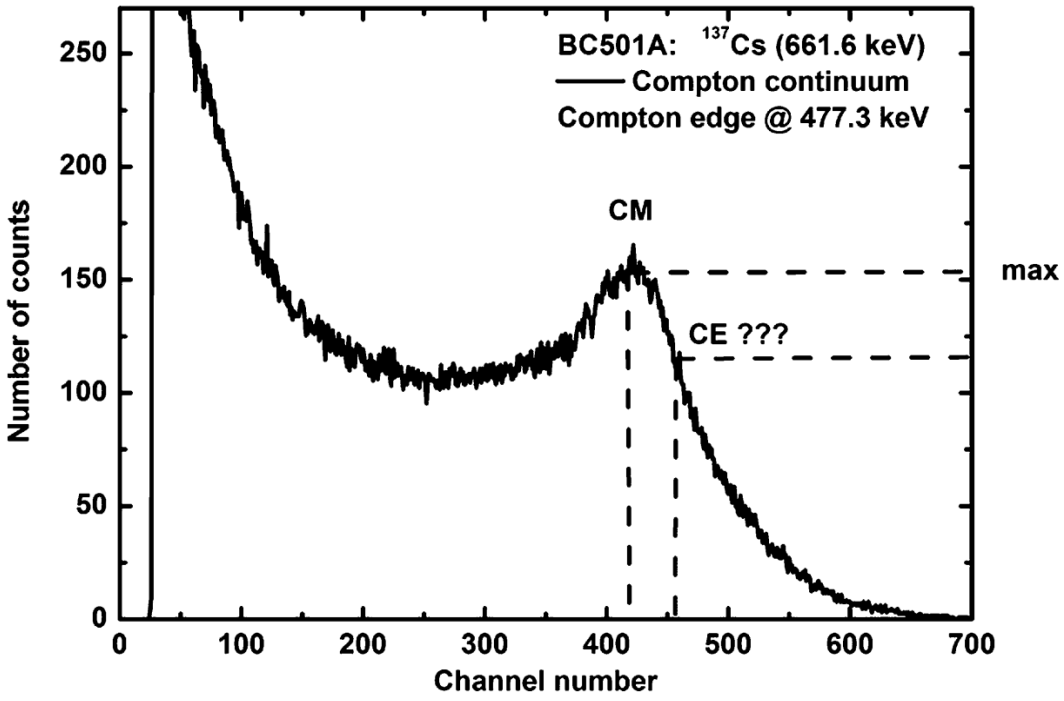

Figure 2.13: Compton continuum and edge in BC501A liquid scintillator, taken from [73].

2.4.2 Photoelectric Absorption

Photoelectric absorption is a highly desirable interaction for gamma spectroscopy applications. It results in a full-energy peak for incident radiation. This interaction occurs when an incident photon is able to liberate a photoelectron from an atom which absorbs the full energy of the gamma ray minus some binding energy [11].

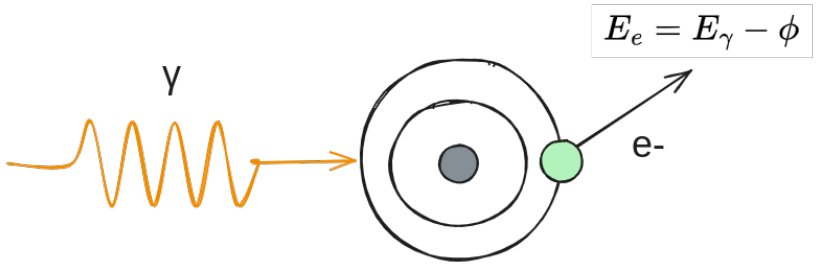

Figure 2.14: Photoelectric absorption process. Absorbing atom emits a photoelectron after absorbing the full energy of the incident gamma. The electron leaves with the energy of the photon minus the binding energy ϕ of the electron.

The full energy or photopeak appears after the Compton edge, as in Figure 2.15.

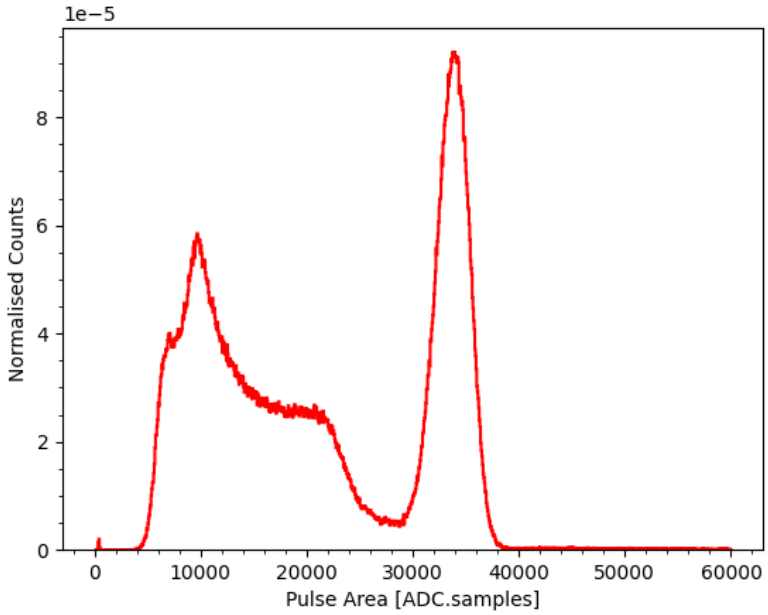

Figure 2.15: Photopeak appears to the right of the Compton continuum. Data taken using a Cs-137 source and a NaI scintillation detector.

These peaks are used in radioisotope identification, and their appearance is dependent upon the detector type used. The probability of a photoelectric absorption event scale strongly with Z, the atomic number of the detector medium. This relationship is variable over energy ranges, but is approximately determined as in Equation 2.12, with n varying between 4 and 5 depending upon the gamma ray energy [11].

$$P \approx k \times \frac{Z^n}{E_\gamma^{3.5}} \tag{2.12}$$

2.4.3 Pair Production

In the case of a sufficiently energetic gamma ray, an incident gamma ray photon may convert into an electron-positron pair as in Figure 2.16. Pair production becomes energetically possible above the threshold of 1.02 MeV [11], with any excess energy shared between the particle pair produced. In order to properly conserve momentum, the process of pair production must occur within the presence of a nucleus [74].

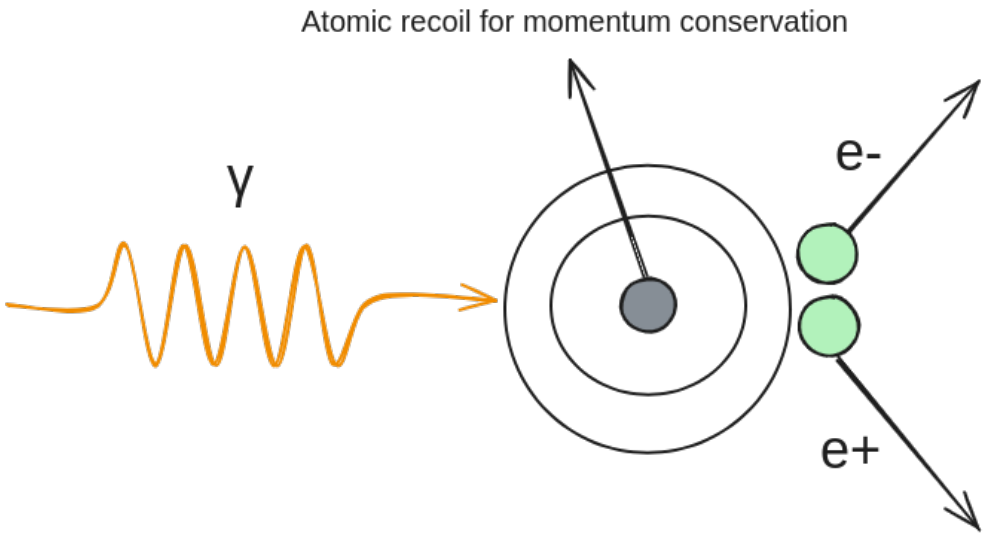

Figure 2.16: Pair production occurs when a photon of sufficient energy close to a nucleus is able to convert into an electron-positron pair

2.5 Scintillation Detectors

The function of a scintillation detector is to convert incoming ionizing radiation into photons of a detectable wavelength, which can be converted into an electrical signal by a photosensor. The first of such scintillation detectors was used in 1895 by Wilhelm Roentgen to detect X-rays. His detector employed a phosphor screen of barium platinocyanide (an inorganic scintillator) [75]. Scintillators are now deployed in a variety of different applications, as both thin-layered screens and bulk materials. According to their chemical composition, they can be split into two main families: inorganic and organic. High density, high-Z inorganic scintillators are preferred for applications requiring good energy resolution, such as gamma spectroscopy. As discussed, gamma interactions in these high-Z materials are more likely to result in photoelectric absorption and the formation of a characteristic photopeak. Organic scintillators, with typically lower Z-values, are often preferred for lower-cost applications or where fast counting is required.

2.5.1 Inorganic Scintillators

Inorganic scintillators have a long history dating back to the phosphor screens of $CaWO_4$ and ZnS. The most recent of developments, the lanthanum halide

scintillators, are of particular note to this work, as they are the current standard for scintillator based spectroscopy measurements in oil and gas well logging. Lanthanum Chloride and Bromide scintillators show excellent light output (61,000 photons/MeV) and therefore very good energy resolution (2.6% at 662keV [76]). In addition, these scintillators have very short decay times, and so are suitable for high count rate applications [77]. The main benefit of these crystals for well-logging however is their ability to maintain this performance up to and an in excess of $175°C$ [78]. Sodium Iodide has been the scintillator of choice in the well-logging industry for many years prior to this, due to its good temperature stability and energy resolution, along with its low cost. In a lot of cases, it is still used on account of its low cost.

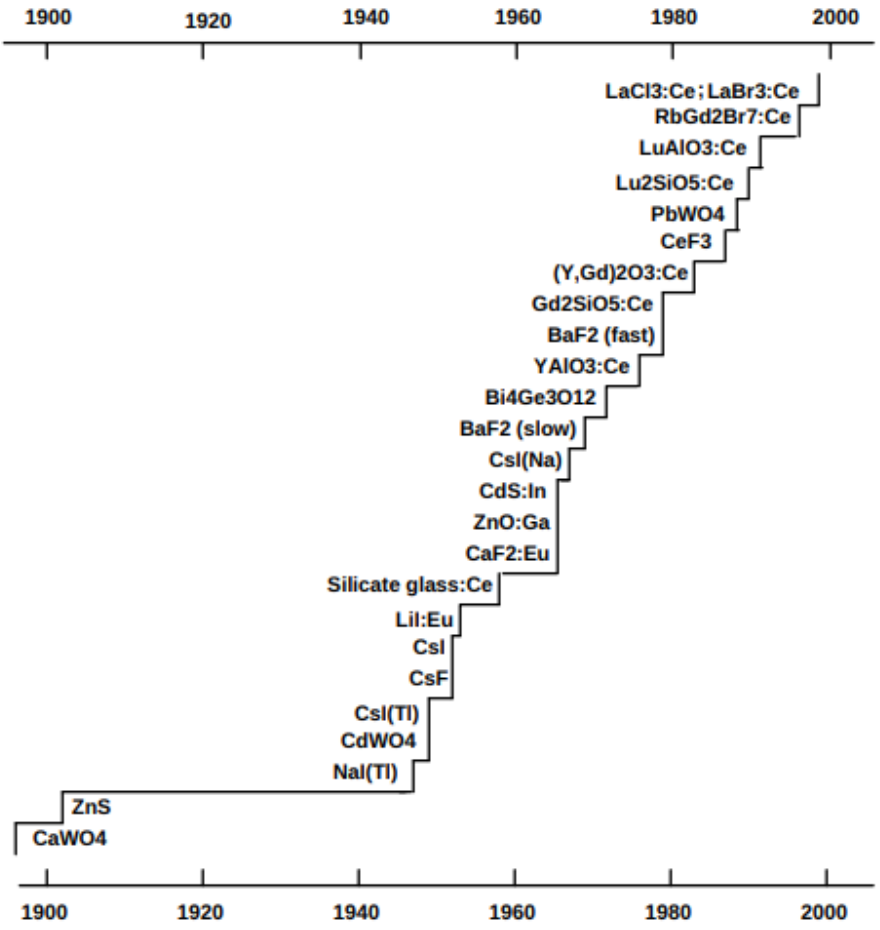

Figure 2.17: Timeline of inorganic scintillator developments. Image from [79]

The mechanism for scintillation in inorganic crystals is complex, but in short, results from the formation and subsequent recombination of electron-hole pairs across the

valence and conduction bands. Understanding of the band structures in scintillators has driven development and improvements for inorganic scintillation detectors [80].

2.5.2 Organic Scintillators

The main body of this work employs the use of plastic scintillators for gamma detection, which belong to the family of organic scintillators. Plastic scintillators are composed of an aromatic matrix (containing benzene rings), with the addition of one or more dissolved organic fluorophore molecules, commonly known as fluors. These molecules are commonly added as a primary or secondary fluorophore, with consideration of the optimal fluorescence and absorption profiles for the base material. Secondary fluorophores are generally added to improve the scintillator emission profile. Improvement in this context means that the light the scintillator emits can travel further with lower attenuation, or is of a wavelength more closely matched to the optimal quantum efficiency of common photosensors. The design of an optimal scintillator is a careful balance of these considerations.

In order to deposit energy within a scintillator, incident radiation must interact via one of the previously mentioned mechanisms. In organic scintillators, it is usually via Compton scattering. The scintillation mechanism itself within organics relies on the energy levels within delocalised π-electron orbitals present within benzene rings in the scintillating molecules present. Energy is first deposited within the organic solvent, which constitutes the majority of the detection medium.

Following interaction of radiation quanta with the scintillation medium, π-electrons are excited into elevated singlet states. Non-radiative energy transfer then occurs into electrons within the primary fluorophore molecules. Radiative energy transfer is then possible, but the light emitted in the UV range is likely to be reabsorbed in the medium. Therefore a wavelength shifter, or secondary fluorophore, is used in lower quantities to improve the transmission length of scintillation light. Light is collected from scintillators on a photosensor such as a photomultiplier tube or a silicon photomultiplier.

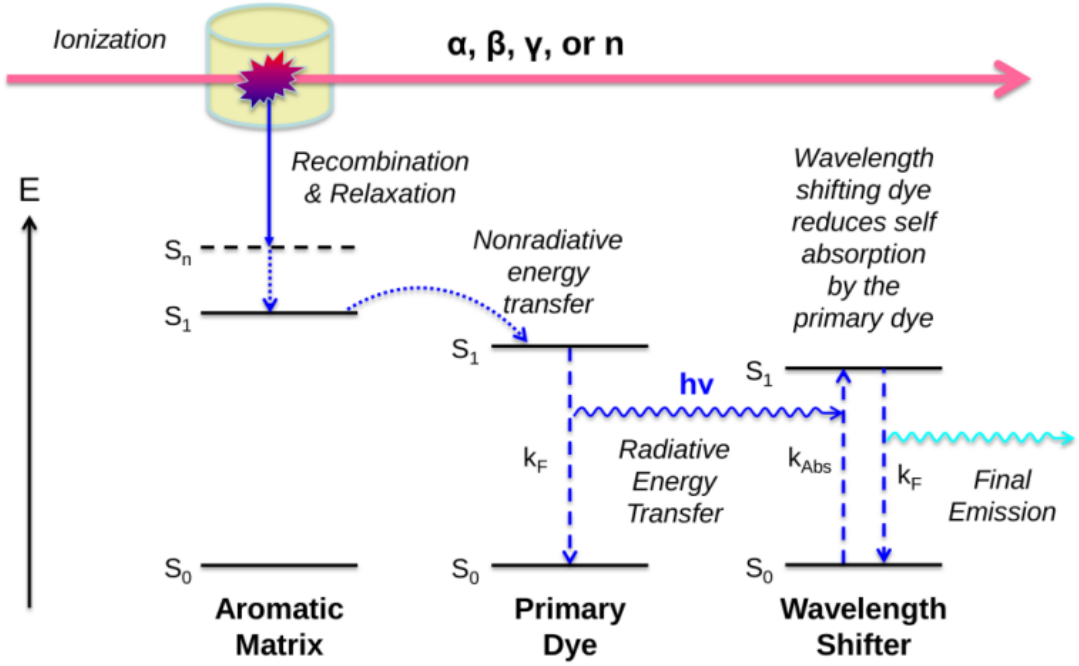

Figure 2.18: Organic scintillation process. Image taken from [81]

Chapter 3

Detector Response Simulations

Nuclear well-logging tools image the distribution of neutron or gamma radiation from a rock formation, as discussed in chapter 2. The objective of this work was to build a mixed-field radiation detector that could predict hydrogen content using a neutron generator source and alternative low-cost detection methods. The specific goal in this chapter is to work towards this goal by understanding the potential detector responses in a test bench setup at Sheffield, and inform optimal designs.

To test potential designs, a suitable rock formation test bench was required. For testing of prototypes, the tool design and testing procedure must be compatible with the available DT PNG setup at the University of Sheffield Neutron Facility, shown in Figure 3.1, manufactured by NSD-Gradel. Encased within a "castle" of magnetite concrete shielding [82], the DT PNG tube is oriented parallel to the ground. Removing all shielding around the generator and constructing an exact borehole analogue around the generator was unfortunately not an option, however following consultation with radiation protection, it was possible to remove a section at the far end of the shielding which could be replaced with variable test material to provide varying detector responses. To better understand the response of a generic prototype detector in this configuration, a series of simulations were performed using GEANT4 [83] and CRESTA [84]. GEANT4 is a Monte Carlo simulation toolkit for the simulation of the passage of particles in matter. It has uses in nuclear, high-energy, and medical physics. CRESTA is an application built using the GEANT4 toolkit to allow for simple setup of complex simulations.

The simulations presented here investigate different test bench geometries to understand which would provide an appropriate signal for a test borehole system

given the configuration of the Sheffield DT source. Ultimately, a combination of factors led to the work presented here, with maintaining shielding for radiation safety a key requirement. Though the generator is operated behind an interlocked, shielded door, it is necessary for risk assessments to reduce fluxes around the shielding to within acceptable dose rate limits. This involves moderating the fast neutrons from the DT source with magnetite concrete. Dose rates for the existing configuration have been confirmed with bonner sphere measurements, and so maintaining as much of the existing setup as possible is ideal. As will be discussed, decisions were made to remove a section of shielding near to the far wall, replacing it with wet sand in a large container. In this way, any potential increases in flux would be directed at the far wall. As the building is constructed on a slope, this far wall is underground, further mitigating risk.

The work presented here maintains sufficient shielding, minimises the required shielding reconfiguration, and provides a suitable detector response from simulations, whilst keeping the DT PNG in its original position. With the associated power and electrical requirements, moving the PNG would be no simple task.

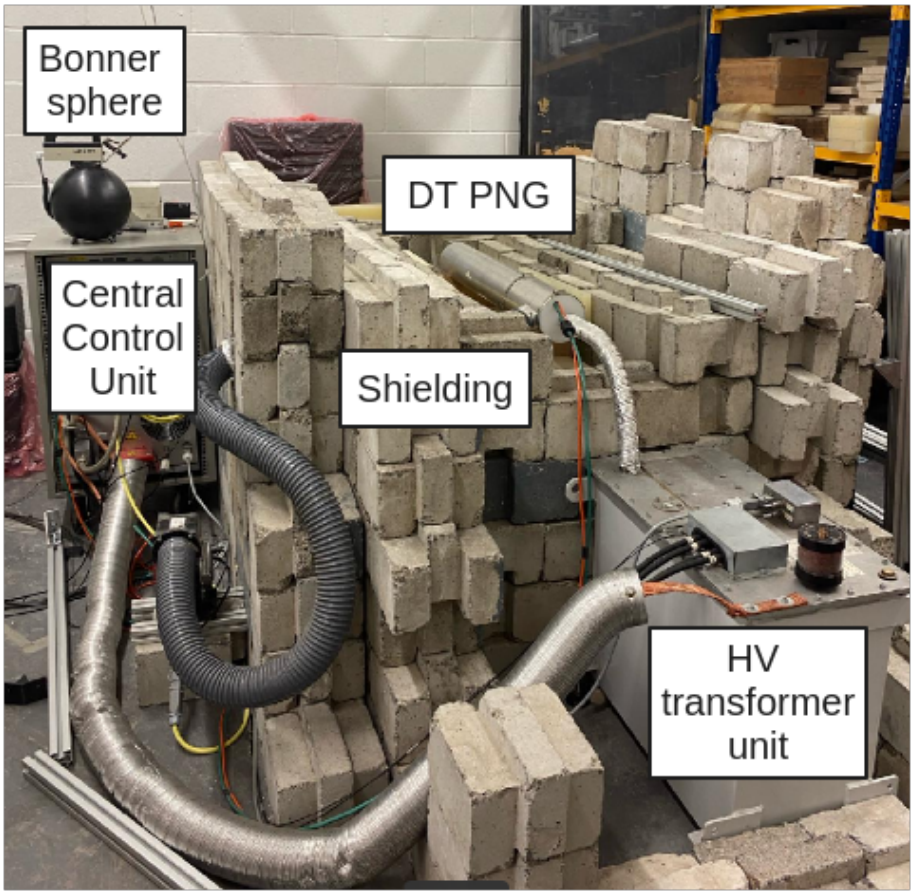

Figure 3.1: D-T Pulsed Neutron Generator Setup in the University of Sheffield Neutron Facility.

3.1 Goals of Simulation Study

With higher water content, there are more hydrogen nuclei present to thermalise and capture incident neutrons, analogous to the presence of oil or gas in an oil well. As a result, it is expected that rates in the detector will drop with increasing water content (as neutrons capture on hydrogen), and the neutron population will die off more quickly. The proportion of hits in different regions of the detector, usually in the form of a near-far ratio, is generally considered a good indicator of the hydrogen content, on account of neutrons travelling shorter average distances before capture in higher hydrogen content formations. This response will be explored in simulations within the context of potential setups within the University of Sheffield Neutron Facility. In these simulations, to study the likely detector response, a simple detector monolith will be used (see Figure 3.2),

consisting of plastic scintillator wrapped in thermal neutron converter foils. Detector hit information from GEANT4 can then be used to extract the positions of detected thermal neutrons and gammas, in order to image their distribution.

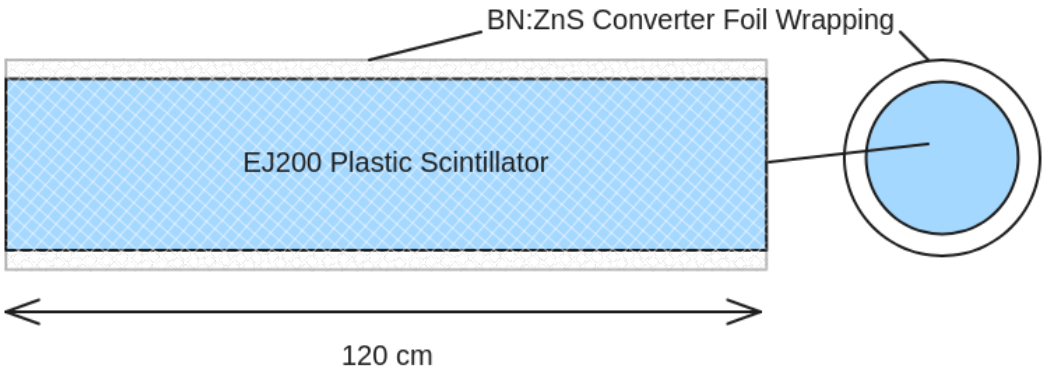

Figure 3.2: Detector monolith for simulation. Simplified design with single cylinder of wrapped plastic scintillator with diameter 10 cm. Foil wrap has thickness 200 micron.

In addition to positional information, timing information is also available from simulations. With a traditional AmBe source, it is only possible to measure the position of neutrons detected, and no time information is available. With a pulsed neutron generator, it is also experimentally possible to timestamp detected events relative to the emission of an initial neutron pulse. However, this information is only useful if it can be successfully correlated with the hydrogen content of a formation. Therefore, a range of sands were examined of differing moisture contents, with a range of different sizes of test container. The footprint of the test container was limited, and so to modify the total volume of moderator material, the container height was varied. The container will be referred to here as a "mock formation". The simulations focused on answering the following key questions:

- For different candidate test volumes (container heights), which show a measurable detector response? Container height will be varied because the container base area is limited within the space available. Increasing the volume of material is expected to impact the detector response, and there is sufficient vertical space to work with.

- Quantify the level of correlation between the distribution of the detector timestamps and the hydrogen content of the mock formations used. Is there a strong relationship between the two?

The first question will inform designs for construction of a detector test bench within the Neutron Facility. This design can then be used to test detector prototypes from the following chapter with the D-T PNG. The second question will be used to inform on the expected level of improvement for timing information in hydrogen content prediction using a mixed-field detector of this design.

3.2 Test Bench Design Constraints

The mock rock setup must:

- Keep the generator contained within its existing shielding
- Be large enough to provide a sufficient detector response
- Allow for modification of mock rock material to test over a range of hydrogen contents

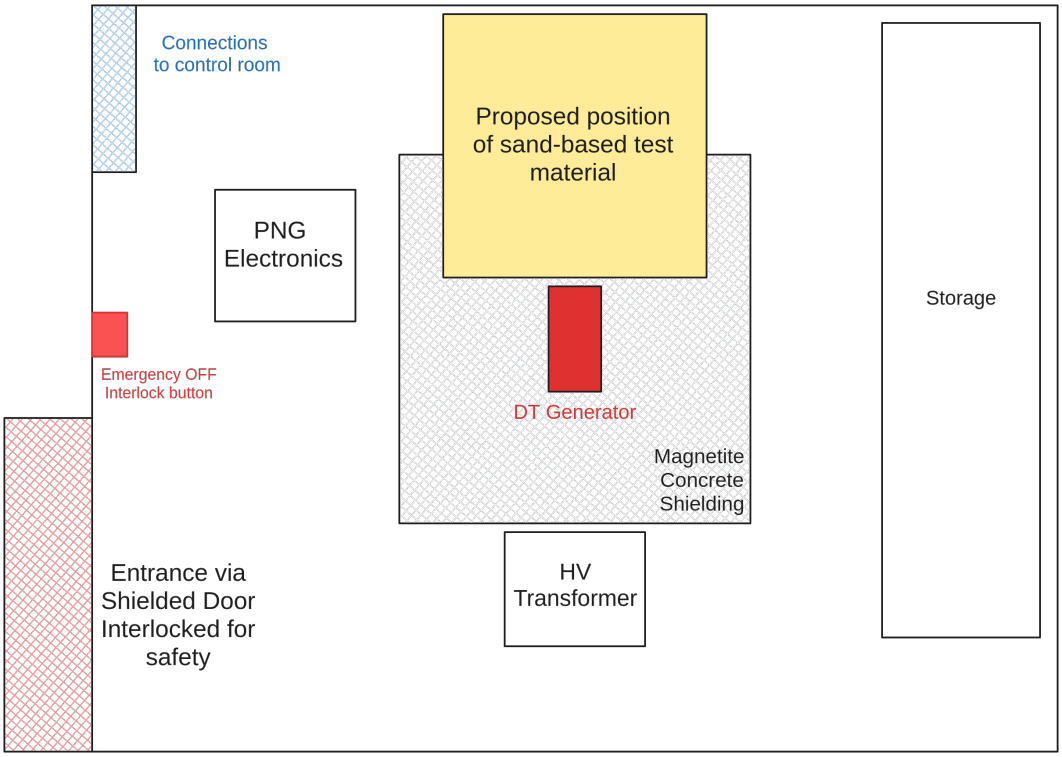

Figure 3.3: Top-down schematic of the generator room.

Simulations were performed to test the ideal size of a sand-based test container placed between the PNG and the far wall, as shown in Figure 3.3. This setup minimises reconfiguration of existing shielding, and allows the DT PNG to remain in its existing position. The mock rock material had an available base size of 80 by 120 cm. The height of this monolith was tested at 30, 60, 90, and 120 cm to examine the height required to elicit a reasonable response in a monolithic detector. The detector in each case was placed directly atop the moderator monolith. In the case of 90 cm height, the detector is directly in line with the DT PNG, similar to a more conventional borehole detector setup.

With eventual plans to test this within the D-T neutron facility, considerations were made of suitable materials that would provide flexibility for the variation of hydrogen content. Though typical rock formations are composed of solid rock (such as limestone or sandstone) with filled pore-space, a more suitable alternative was commercially avaialble builders sand. It provides easy access to a large amount of sediment of known composition, to which water can be easily added, and the content monitored. Therefore, custom materials were created in GEANT4 composed of sand with varying amounts of water, which were subject to 14.1 MeV neutron bombardment in sand containers of different heights.

3.3 Test Bench Simulation Studies

Simulations were performed in GEANT4 [83] to examine differences in detector responses over a range of sands with differing water content. Detected events were timestamped to explore the possibilty of correlating the time profile of neutrons detected with the hydrogen content of the formation. Side and top-down profiles of the GEANT4 geometry are shown in Figure 3.4 and Figure 3.5 respectively.

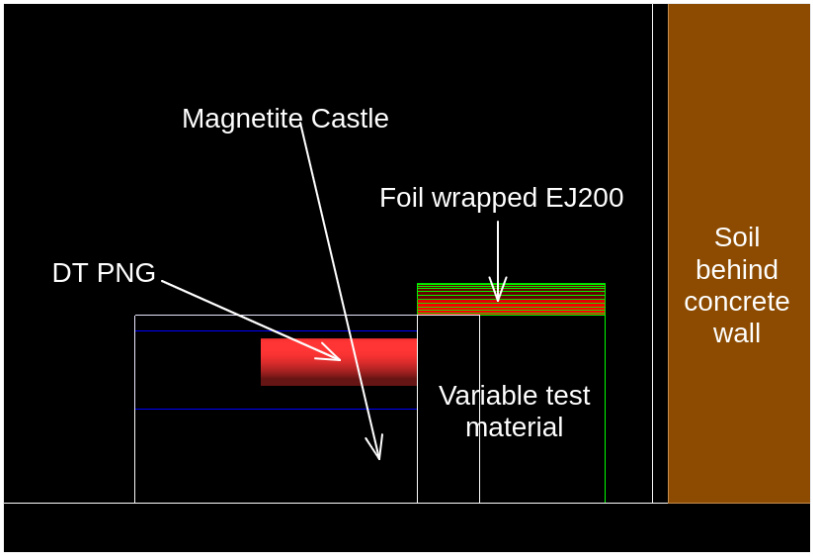

Figure 3.4: Side profile of test bench simulations

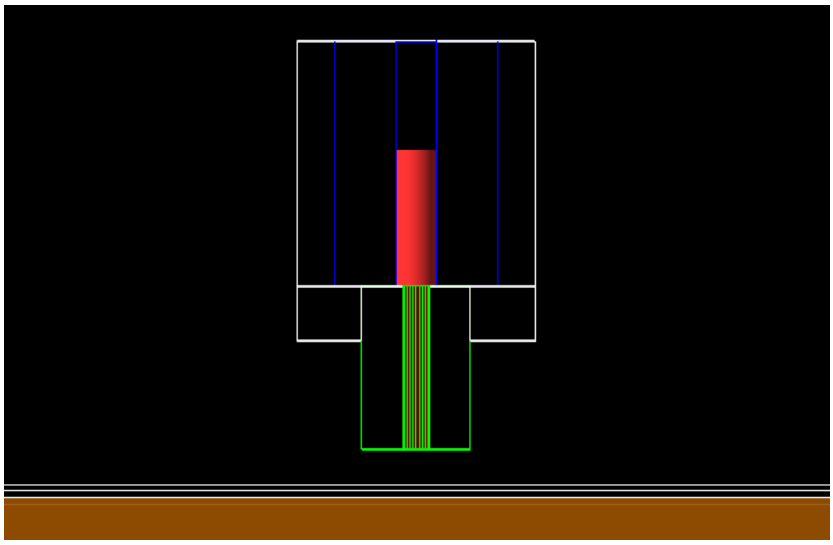

Figure 3.5: Top-down profile of test bench simulations

3.3.1 Modelling the DT PNG Flux

The D-T PNG was modelled as a monoenergetic (14.1 MeV), isotropic emission from a 5 cm line source as described in the NSD-Gradel documentation. The 5 cm diffusion region from which neutrons are emitted is encapsulated by an aluminium housing. There is in fact a small 0.3% D-D fusion contribution to the neutron flux, which has

not been modelled as part of the source spectrum for these simulations.

In simulation, all neutrons are emitted at an effective "zero-time", with the time of detection recorded using GEANT4 hit information. This results in collection of simulation data that empirically would actually be built up over many pulses of the neutron generator, since all time measurements in real data will be taken relative to the generator pulse.

3.3.2 Detector Configuration and Physics

The detector in this simulation consists of a 10 cm diameter, 120 cm length cylindrical monolith. This monolith is a combination of EJ200 plastic scintillator (for gamma sensitivity), wrapped in BN:ZnS scintillating foil (for thermal neutron sensitivity). The simulations did not consider optical transport at this stage, nor the presence of photodetectors in the detector volume. More detailed discussion of optical transport in detectors of this type and segmented detector design is explored in chapter 4.

For each sand composition, 15 million neutrons of 14.1 MeV were generated isotropically in the simulation at the neutron generator. Detector hits in the foil were determined by energy deposition over 2 MeV yielded from charged nuclei emitted by a neutron capture event on boron-10 (as in the reactions discussed in chapter 2). Gammas were recorded based on energy deposition within the bulk EJ200 plastic scintillator. For all particle trajectories in the detectors, the simulation recorded: energy deposition, the average position of this energy deposition, and the time at which this occurred relative to time-zero (when the initial neutron was emitted by the source). This information was used to generate an overall detector response for different hydrogen contents. The GEANT4 physics list used for this study was "QGSP_BERT_HP", where "HP" denotes the High-Precision neutron libraries for the transport of neutrons below 20 MeV. This is crucial to properly model neutrons in this energy range.

3.3.3 Test Materials

Materials were set up in GEANT4 to model sands of different water contents. A common unit used in well-logging to differentiate between materials containing different amounts of hydrogen is hydrogen index. The sand was assumed to be made wholly of silicon dioxide, with added pure water. The sand was simulated over a range of different

hydrogen indices, corresponding to the amount of hydrogen in the test material.

Hydrogen Index

Hydrogen index is defined as the density of hydrogen relative to that of water [85]. It is defined by the following formula:

$$HI = \frac{9 n_H A_H}{\sum n_i A_i + n_H A_H} \tag{3.1}$$

n_i and A_i are the number of atoms per molecule and atomic masses of elements within the material. The same quantities with sub-H represent hydrogen. The factor 9 appears due to the ratio of relative molecular masses of hydrogen and water, 2 and 18. For further detailed discussion on hydrogen index see [7]. It denotes the number of hydrogen atoms per unit volume relative to pure water. It can also be said to be the density of hydrogen relative to pure water [85]. Hydrogen index and formation porosity (ϕ) are inter-related such that in specific circumstances they can be considered one and the same. Limestone is used to calibrate detector tools, and so when inevitably used to measure porosity in formations that are not limestone, calibration curves are required for conversions.

For a detector tool within a "formation" of pure water, the hydrogen index is unity - relative to water, there is the same amount of hydrogen. This can be considered a limestone rock of 100% porosity. In this instance, HI= ϕ. One may also consider a mass of solid limestone with zero pore space, and thus $\phi = 0\%$. HI= ϕ in this case, since there is no hydrogen present and there is zero porosity in solid rock. Intermediate porosities will have HI= ϕ if the rock is limestone with completely water filled pore space. Therefore, hydrogen index tracks porosity given these specific conditions are met. For well log interpretation, calibration tables are available to perform corrections and properly convert hydrogen indices into porosities. Some formation rocks may contain hydrogen or bound water, which can impact upon detector responses, leading to inaccuracies in porosity predictions. This work will focus on correlating detector response to hydrogen index only.

3.4 Results and Analysis

In the first case, the ability of the test formation to generate a measurable detector response was investigated. This work would demonstrate the necessary size of a volume

of sand material for prototype detector testing. Each simulation performed in this work consisted of a sand-based test bench of a particular height, with sands over a range of different hydrogen contents. The results show the variation in detector response across these parameters.

3.4.1 Detector Response with D-T PNG Source

Hydrogen indices were varied between 0 and 0.16, with a hydrogen index of 0.16 corresponding to around 150 kg of added water in the sand setup. The detector response was investigated over this range of hydrogen indices. Neutron counts were recorded as events depositing over 2 MeV of energy in the converter foil, and occurring over 100 µs after the initial neutron pulse to avoid pileup (see chapter 6 for a more detailed discussion on pileup).

The neutron counts per incident neutron shows a clear relationship with the hydrogen index, and is shown in Figure 3.6. 30 cm was found very early on to show no response and is omitted here. 60 cm again shows no clear response to hydrogen index but is included for reference. For larger container heights, both at 90 and 120 cm, the neutrons detected per incident neutron is negatively correlated with the hydrogen content. This is to be expected, with more hydrogen present, neutrons are more readily absorbed in the sand, resulting in lower counts in detectors. This effect is less noticeable at higher hydrogen indices. There is also a noticeably higher count rate in the 90 cm height formation compared with 120 cm. This is likely due to neutrons entering the 120 cm formation and being captured before they can exit the top face and be detected. Higher count rates are desirable for detector testing.

The response of the plastic scintillator was also explored to investigate whether the gamma response of the detector showed any correlation to the hydrogen index. The gammas detected per incident neutron is shown in Figure 3.7. This plot shows the case in which any energy deposition in the plastic scintillator is recorded as a hit. In the case of gammas, though there is an initial rise between hydrogen indices of 0 and 0.02, beyond this the gamma counts begin to fall. As water is added, the sand material becomes more dense. With increasing density, more gammas are attenuated before they can reach detectors. It is believed that this shielding effect begins to overwhelm the increase in gamma rays from added hydrogen in this setup.

The goal of these simulations was to ensure that a detector response was obtainable using a test bench of the simulated dimensions. Near-far count ratios are commonly

used in neutron-logging to highlight the reduction in thermal neutrons reaching a far detector relative to one nearer the source. Therefore, a near-far count ratio was used to demonstrate a response to a large mass of material in the simulated monolithic detector. In this preliminary case, to produce a near-far detector neutron count ratio, the counts below and above a position cut along the length of the detector were used.

Figure 3.10 shows the near-far neutron count ratio for a basic near-far cut which divides the 120 cm detector into two slices, near and far. The near-far ratio generally increases with hydrogen index in the cases of the larger containers of 90 and 120 cm height. The cut for this response is 10 cm along the length of the 120 cm detector. This same near-far ratio is calculated in the following section for an AmBe source, a more conventional setup for a hydrogen index/porosity measurement.

Both 90 cm and 120 cm height sand containers demonstrate a response to increasing hydrogen content. 120 cm has notably better dynamic range, but will require more material. 90 cm still demonstrates a measurable response to the hydrogen content, and also has the advantage of allowing the detector to be placed in line with the DT source. This geometry is more analogous to conventional borehole setups. 90 cm also showed higher count rates when compared with 120 cm. This is also noticeable in the increasing size of the error bars for the near-far ratio in the case of a 120 cm height test formation.

This work also considered that increasing positional segmentation in detectors may be of benefit for the prediction of hydrogen content. With this monolithic detector in simulation, it is possible to fit a decay curve to the counts as a function of position along the detector. Figure 3.8 shows the distribution of neutron hit positions in the detector monolith for one of the sand compositions tested. The red line shows an exponential decay fit to this distribution. Applying this procedure to all of the simulated sands, the decay parameter can be plotted against the hydrogen content. This plot is shown in Figure 3.9 for the case of a 90 cm height test container.

It should therefore be possible based on this simulated setup to test prototype detectors using a formation of base dimensions 80 by 120 cm with 90 cm height over this range of hydrogen contents using a DT neutron source. The effect should be particularly pronounced moving from very low hydrogen indices around 0 up to the 0.08 region. This is based on the detected positions of thermal neutrons in a monolithic detector. It should be noted here that more typical borehole setups generally show much higher near-far ratios with better dynamic range. Additionally, the demonstrated relationship between exponential fit parameters and hydrogen index suggests that a detector with

good position resolution, perhaps through the use of a segmented detector, may be desirable for this application. Therefore in the following chapter, one of the potential designs explored is a modular segmented detector using fibre readout to maximise active detector volume.

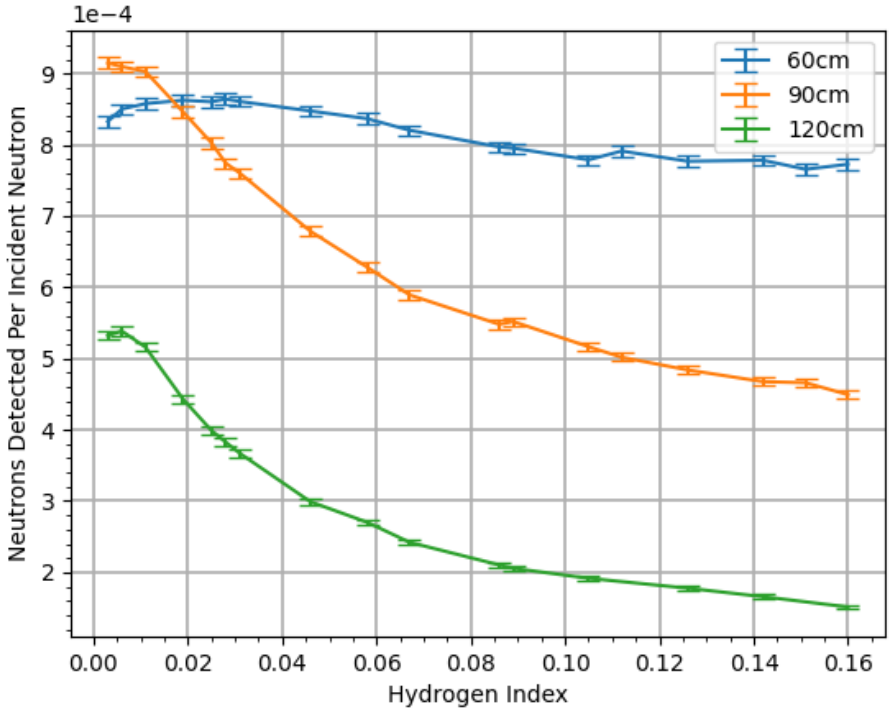

Figure 3.6: Detected neutrons per incident neutron fired in simulations for three potential heights of test container with the detector laid on top.

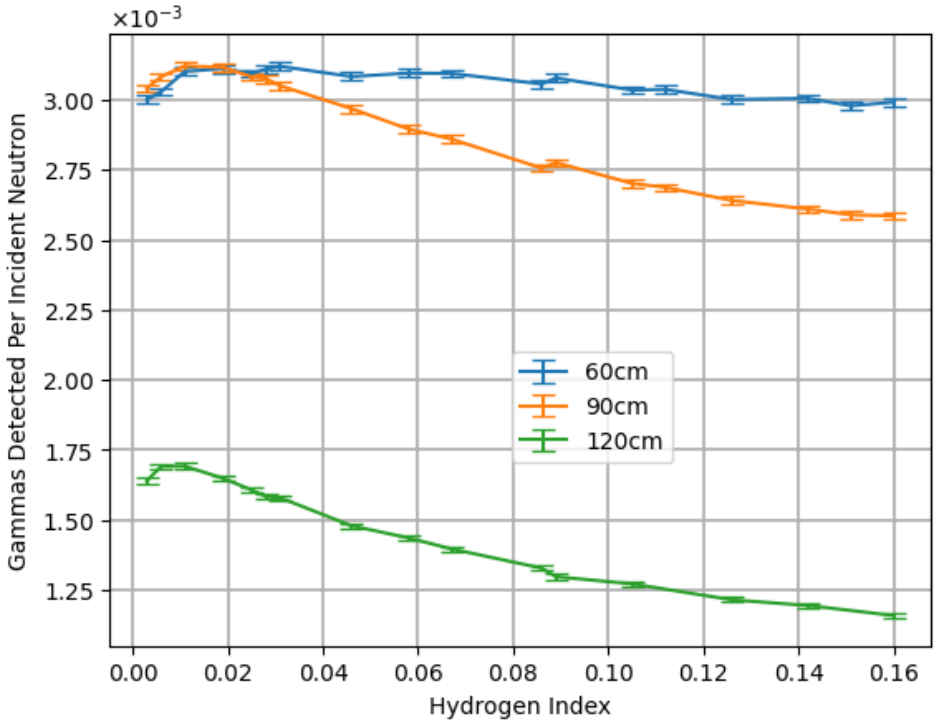

Figure 3.7: Detected gammas per incident neutron fired in simulations for three potential heights of test container with the detector laid on top.

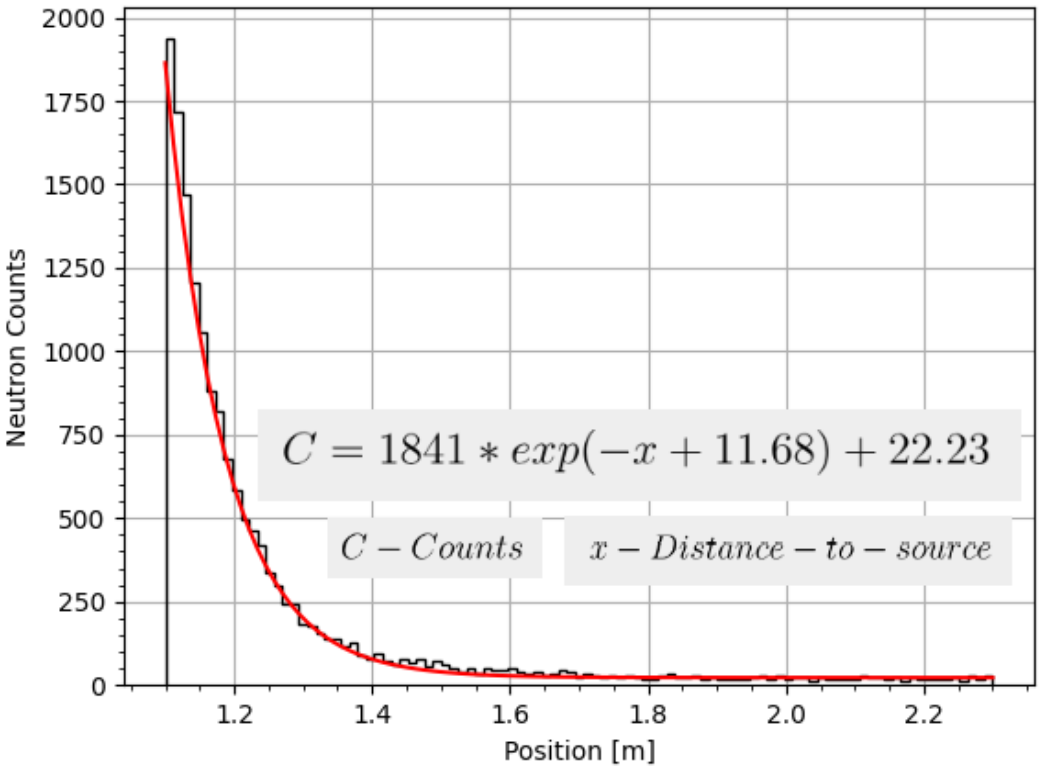

Figure 3.8: An exponential fit to the position distribution of detected neutrons in the simulated detector monolith for a sand of hydrogen index 0.105.

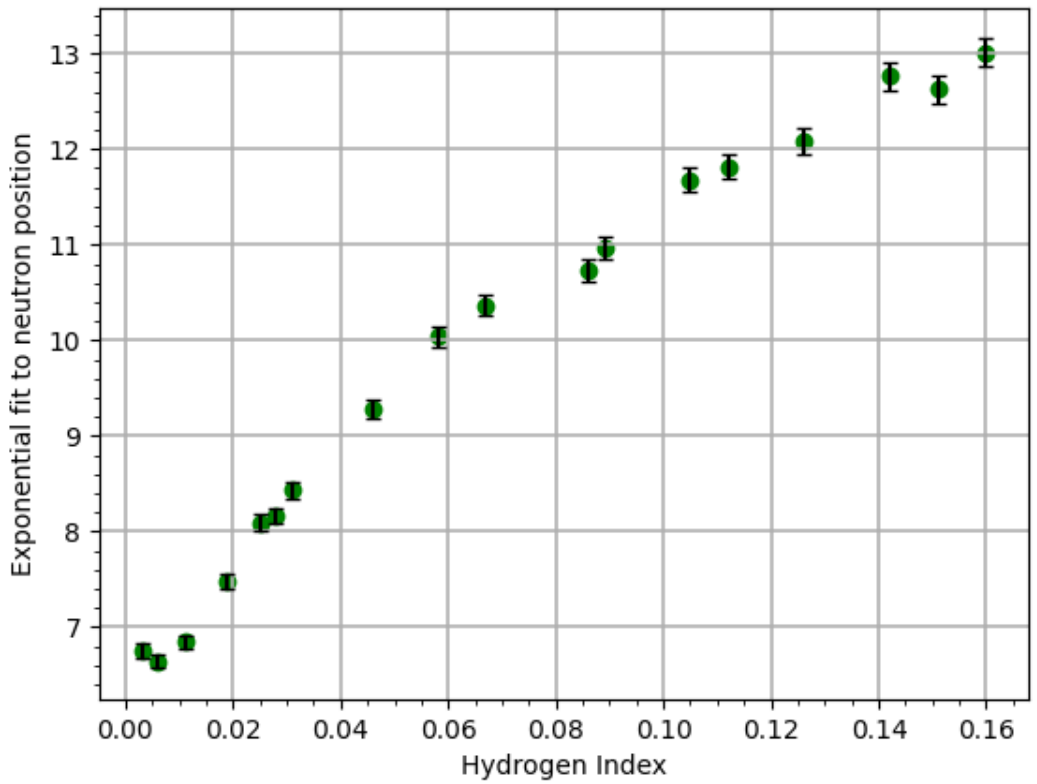

Figure 3.9: Exponential fit parameters for the position distribution of detected neutrons across a range of hydrogen indices in a 90 cm height test formation.

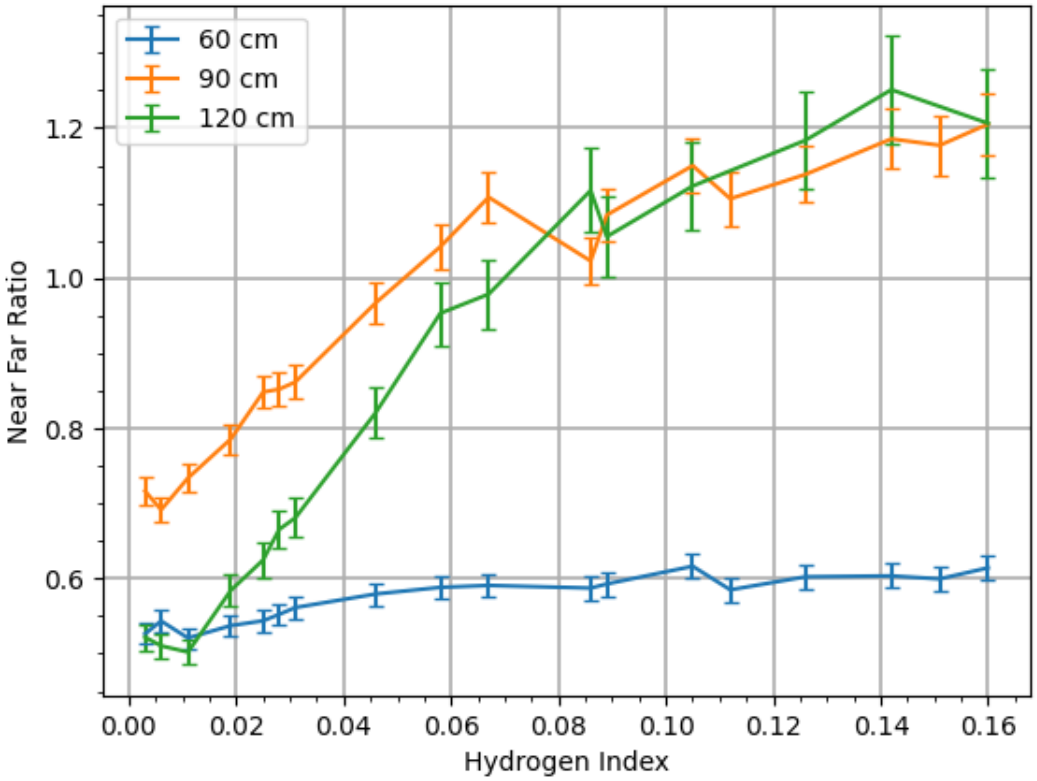

Figure 3.10: Simulated near-far ratios over the range of tested hydrogen indices for different heights of test formation for a DT source spectrum in GEANT4.

3.4.2 True Borehole Comparison with Mock Container Setup

The true replication of an exact borehole setup in a laboratory environment is extremely challenging. At any typical neutron research facility with access to a pulsed neutron generator, the setup will likely be similar to that at Sheffield. A pulsed neutron generator will generally be surrounded by a large volume of shielding, along with required electronics and controls. This of course limits the movement of existing PNGs at established research facilities, complicating research efforts for borehole systems. In addition, disregarding logistical concerns, if a real borehole was to be drilled on-site and a source placed downhole, it has been explored already in chapter 1 the potential liabilities involved. Even commercial detector systems and sources can become lodged downhole, with large fines handed down to offenders. For this reason, it is not feasible to simply drill a borehole for testing a prototype detector rig.

Therefore in this work, mock rock test benches are used, with a geometry that fits into existing setups. The previous simulation geometry, which examined the setup with test containers of different heights, was modified to replace all surrounding material with the test sand, in a borehole of diameter 11 cm. Though boreholes vary in size, this is within the typical range of boreholes for well-logging. Therefore in the following plots, reference to a "true borehole" scenario means a setup in which a cylindrical borehole is used surrounding the full detector, closely replicating a real world siuation. This is compared with the scenario which was realistically possible to build within the Sheffield Neutron Facility, with a large container of material, with a detector placed on top.

The key difference in the results of these simulations was the large difference in neutron count rates in detectors. With a full borehole surrounded by material, there is far more hydrogen present to capture neutrons. Figure 3.11 shows the neutrons detected per neutron generated in simulation, and demonstrates the large disparity for the case of a 90 cm height test formation versus a typical borehole. There is still a comparable declining trend for both a realistic borehole and a 90 cm test container, however the dynamic range for a true borehole setup is orders of magnitude larger. However count rates per neutron fired are higher with the test container. Therefore, though the test container setup may not offer the best response over a range of hydrogen indices, it can offer higher count rates, which is desirable for detector testing (even more so for testing with lower activity sources).

On account of low count rates in the true borehole simulation case, drawing conclusions on near-far ratios and detector responses leads to large errors, particularly

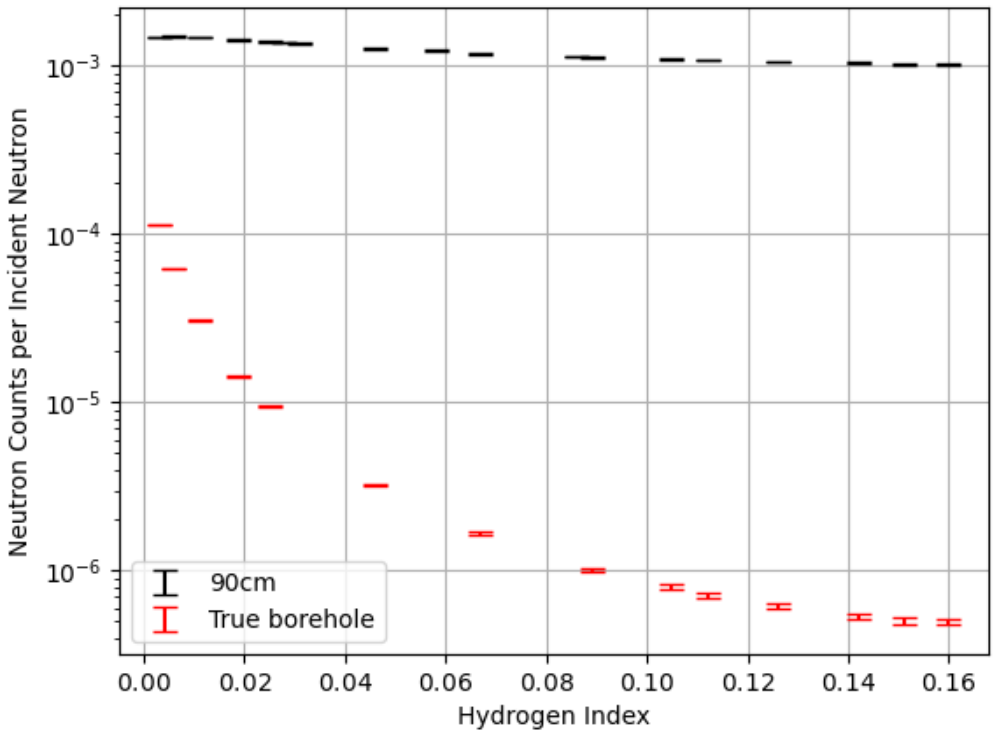

Figure 3.11: Detected neutrons per incident neutron for the case of a mock test container versus a more typical true borehole setup.

at higher hydrogen indices. This could be improved by increasing simulated events for the case of a true borehole, leading to higher numbers of events in detectors, however the simulation runtime for the true borehole case is already prohibitive. Further optimisation of the true borehole simulations could improve these issues. See an example of the impact of poor statistics in the true borehole scenario in the near-far ratio plot in Figure 3.12. The effect is particularly pronounced with higher hydrogen index, when more neutrons are captured before they can reach the detector.

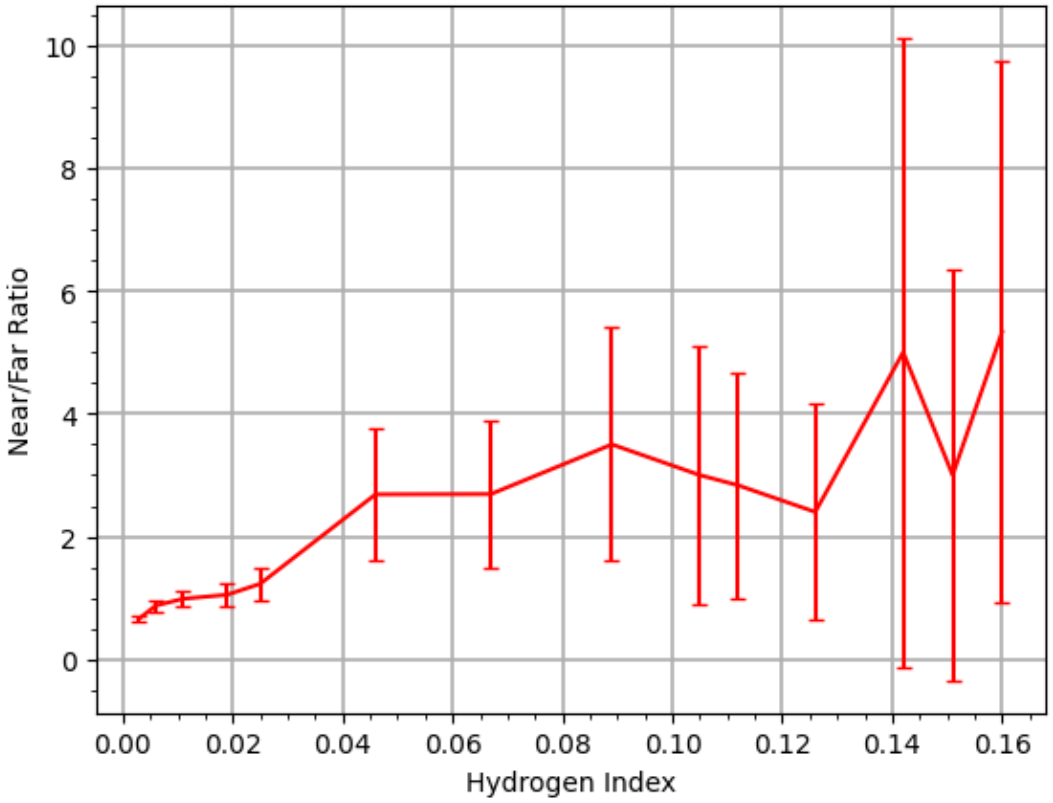

Figure 3.12: Poor statistics in the case of a true borehole simulation make comparison difficult. More rock material contains more hydrogen, capturing neutrons and significantly reducing count rates.

3.4.3 Detector Response with Conventional AmBe Sources

As discussed, conventional radioisotope sources show a better response in typical near-far ratio detector setups on account of their energy spectrum. To demonstrate this, an AmBe neutron source was simulated to compare to the near-far ratio response of the DT source. AmBe sources have a mean energy (4.2 MeV) much lower than that of DT sources (14.1 MeV). For this reason, DT neutrons are able to travel longer distances on average before reaching thermal energies. The resulting effect is that DT sources display a poorer dynamic range in the near-far ratio response, due to a less pronounced slowing-down effect (i.e neutrons are more likely to reach the far-detector). Figure 3.13 shows the same near-far ratio plot from simulations, this time using an AmBe source spectrum to produce incident neutrons.

Again, a clear response in the near-far ratio is visible, but this time with improved dynamic range, even in this atypical borehole setup. This disparity in dynamic range is

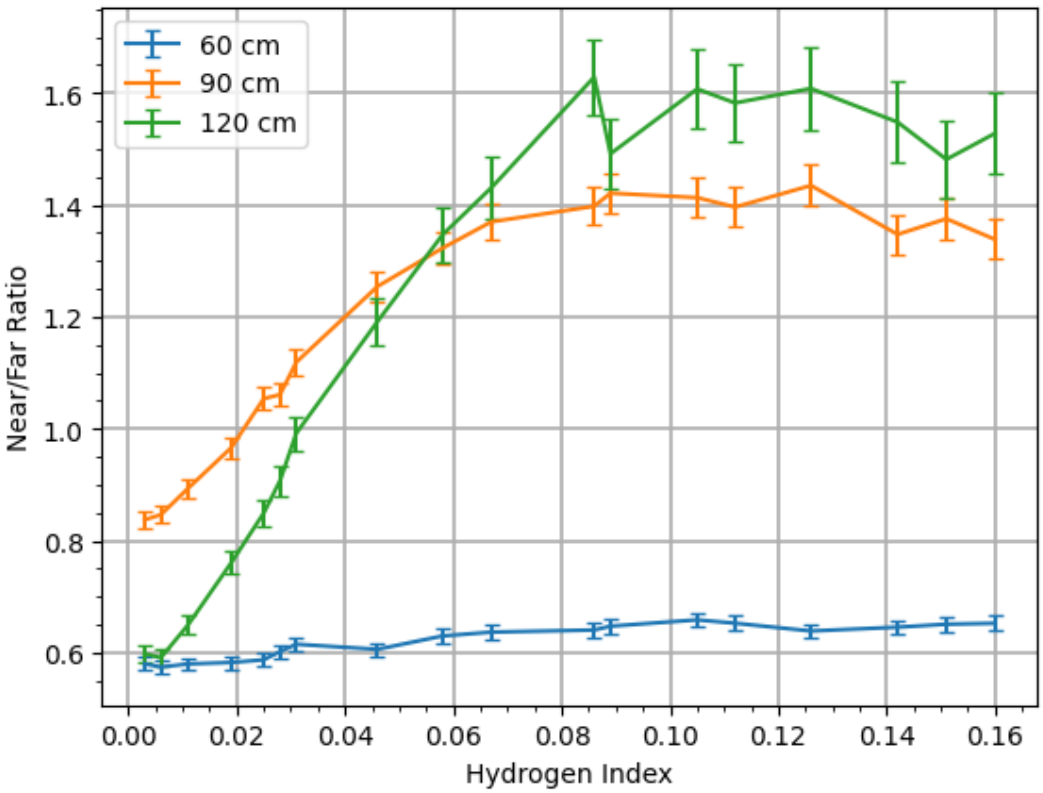

Figure 3.13: Simulated near-far ratios over the range of tested hydrogen indices for different heights of test formation for an AmBe source spectrum in GEANT4.

larger for more conventional borehole setups, such as those explored in [31]. In the case of this work, the geometry limits the ability to optimise detector spacings much further, however, this highlights how even in sub-optimal configurations, AmBe sources display superior sensitivity to hydrogen content. This is one reason why DT sources have not been more widely adopted for the measurement of hydrogen content. The near-far count ratio response for DT neutrons is not competitive with AmBe. However the potential informational benefit of using DT neutrons lies in the use of pulsed sources, which allow for timestamping of events relative to neutron emission. The next consideration is whether there is a measurable response in the timing from this setup which can be related to the hydrogen content.

3.4.4 Timing Response of D-T PNG source

In the previous sections, analysis considered only the position of detector hits and the raw counts. This is a more conventional approach which has been in common use for

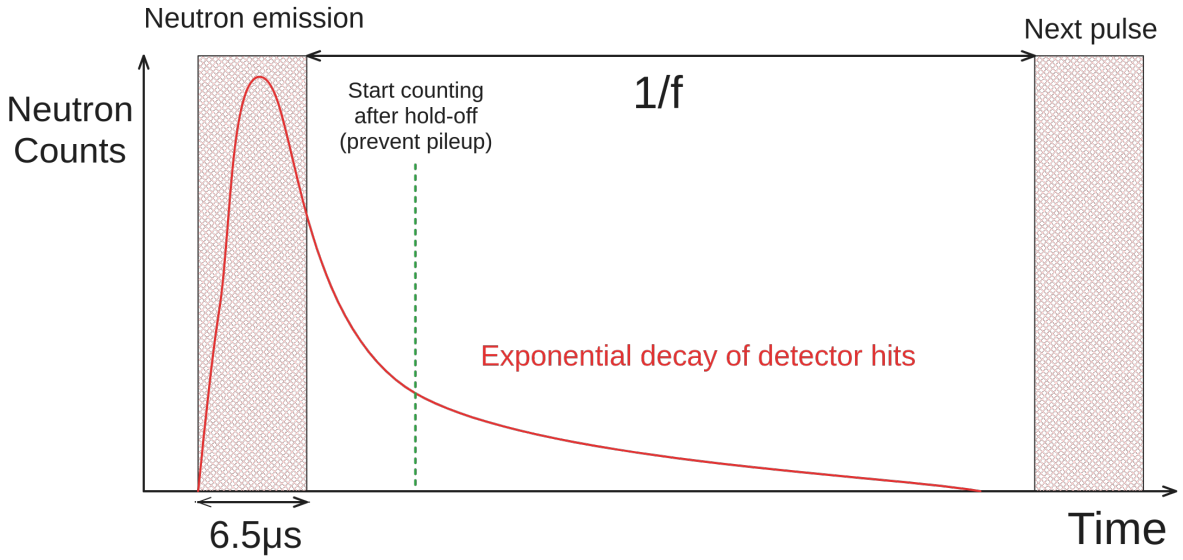

Figure 3.14: DT emission and detection. DT generator emission occurs in a 6.5 µs window, before the neutron population decays exponentially.

many years with optimised detector spacings for typical borehole setups. In this work, one of the key areas of interest is the time response of the neutron distribution following a neutron generator pulse. With a PNG, event timestamps present an additional variable of interest for hydrogen content prediction. For a pulsed DT source, it is possible to record, with a resolution of a few microseconds, the emission time of the incident neutrons. In fact, spectroscopic well-logging systems already employ this time-after-emission to improve the resolution of gamma spectroscopy, separating hits into inelastic, capture, and delayed activation time ranges. Here, timestamps will be used to explore any relationships between the hydrogen content of the formation and the decay time of the neutron population in detectors. This parameter could lead to improve dynamic range for a detector using DT sources for hydrogen content evaluation. Figure 3.14 shows the emission profile of neutrons followed by the slow decay in the neutron population as neutrons are captured. The aim of this work is to capture the decay profile of these neutrons, and use this information to assist in the prediction of hydrogen content.

Neutron detection times from simulation were binned in histograms for the case of DT neutrons, since it is only feasible to obtain this information with pulsed sources. A hold-off in time was added after the emission of neutrons of 100 µs. The reason for this is discussed in more detail in chapter 6, but in short, this removes pileup from direct

bombardment of the detectors which renders PSD impossible. The upper limit of the time binning range is dictated by the arrival of the following neutron generator pulse. As in Figure 3.14, this is determined by the pulse frequency of the neutron generator. The NSD-Gradel Fusion DT PNG used in this work is capable of pulse rates between 2 and 30 Hz, and for this work, the maximum available pulse rate of 30 Hz was used. This corresponds to a time between neutron pulses of 33 ms. In fact, the neutron population generally falls to zero before this, and so for the purposes of the fitting procedures here, times were binned between 100 µs and 3000 µs. The histogram in Figure 3.15 shows the die-off in neutron counts over the time interval between pulses.

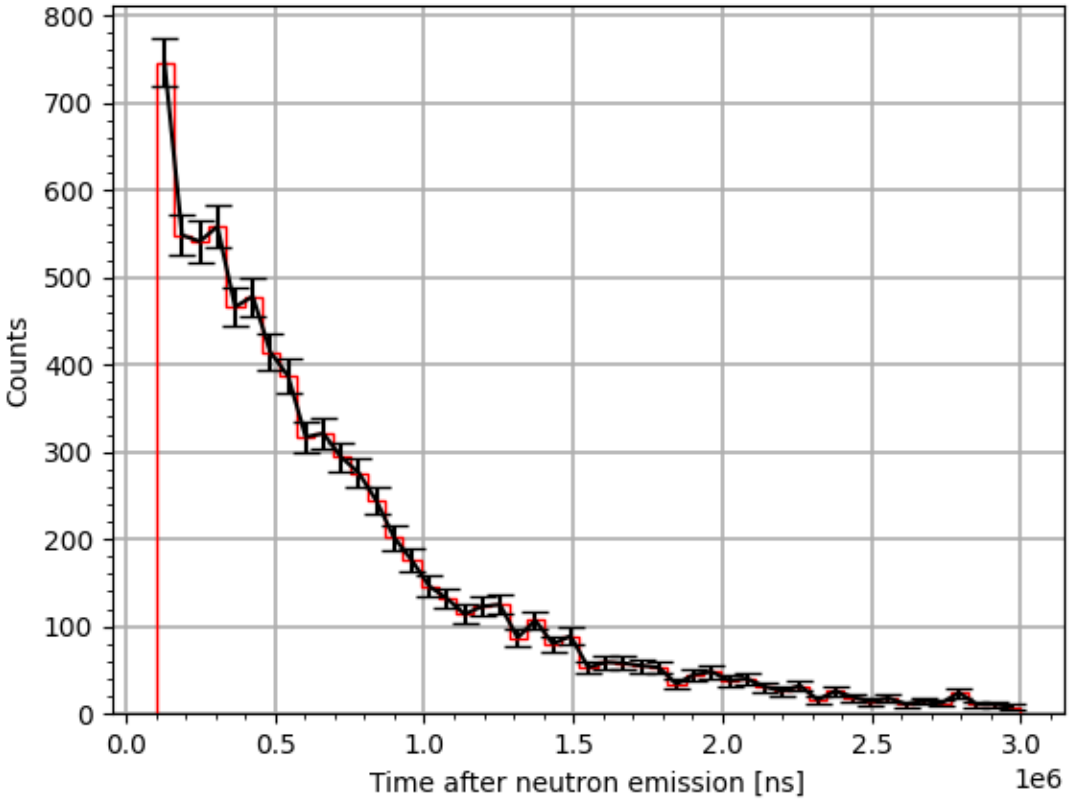

Figure 3.15: Detection time distribution for neutrons from DT source in a formation of low hydrogen index. The exponential decay is characteristic of the amount of hydrogen present in the formation.

Timing analysis was performed for the case of a 90 cm height test formation, on account of higher count rates, and the ability to level the detector with the neutron generator. Time histograms for different hydrogen contents were fit to the exponential in Equation 3.2, where N_0 and $N(t)$ are the initial detected neutron counts and the

detected counts at time t. λ is a decay constant, and c a constant.

$$N(t) = N_0 e^{-\lambda t} + c \tag{3.2}$$

The exponential fit parameter λ, is plotted against the hydrogen index for the simulation. A clear relationship is observed between the neutron decay time and the hydrogen content of the formation (see Figure 3.16). This plot shows the decay parameter, λ, perhaps better described as $1/\tau$, as a function of hydrogen index for the formations simulated. For sand of higher hydrogen content, the decay parameter increases before plateauing at hydrogen indices above 0.08, indicating that the neutron population decays more quickly as neutrons are more likely to be thermalised and captured on hydrogen. This information is not available from conventional radioisotope sources. This parameter can therefore potentially be used to assist in the prediction of the hydrogen content of the formation based upon simulation with this setup. The prototype detector built will aim to observe similar changes in the timing distribution of neutron detector hits. The sensitivity however is limited in the hydrogen index range up to 0.08 with this geometry. This appears to be the amount of hydrogen at which point the detector response in terms of the time distribution of neutron counts no longer offers any significant information on the hydrogen index. In a more conventional borehole setup, with larger spacing between source and detector, it is possible that this range could be extended further.

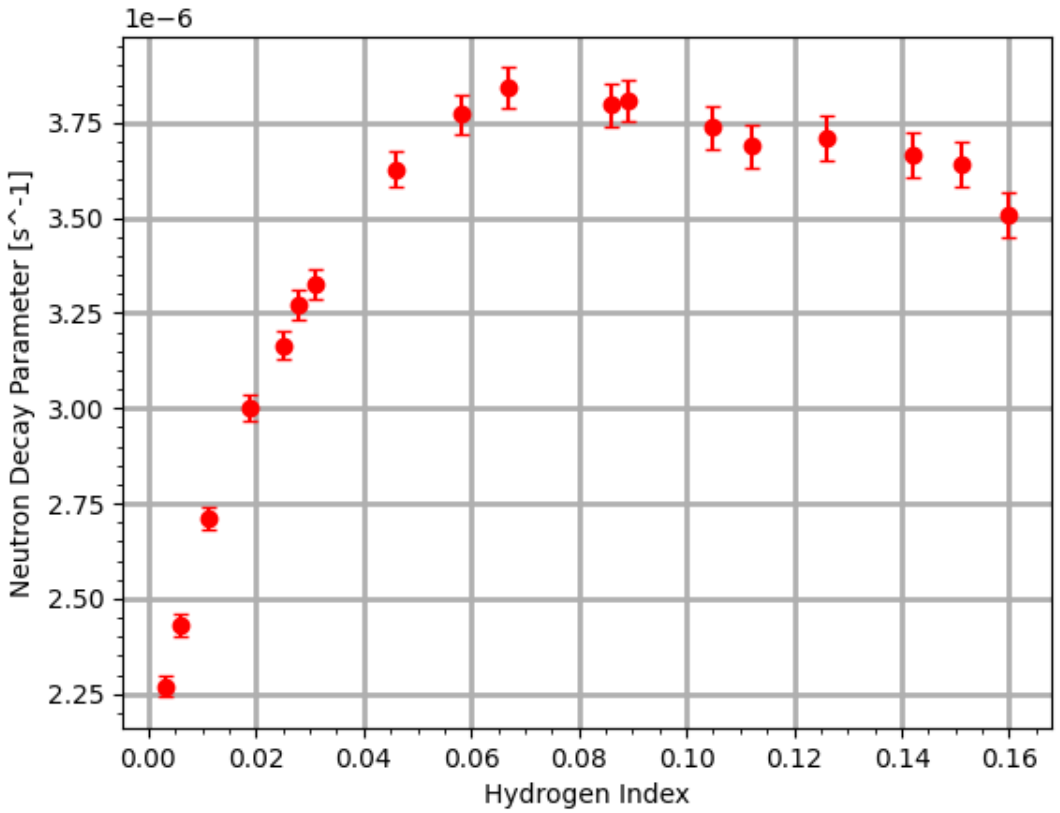

Figure 3.16: Neutron population exponential fit parameters for each hydrogen index in simulation with a 90 cm height setup. There is a clear trend toward faster neutron population decay with increased hydrogen content, suggesting predictive power in the timing distribution.

3.5 Chapter Summary

- There is a demonstrable relationship in simulation between the hydrogen content of a sand based test stand and the neutron detector response in a monolithic detector composed of plastic scintillator and thermal neutron converter foil wrapping.
- A 90 cm height test stand will be constructed and filled with sand and varying quantities of water to test prototype detectors. This setup produced a measurable response in a monolithic detector in GEANT4 simulations.
- There is a measurable response in the near-far detector count ratio for neutrons from a DT source using a 90 cm test stand.

- AmBe sources, even in this unconventional test stand displays superior near-far ratio response to increasing hydrogen content when compared with a D-T source.
- D-T sources can be pulsed, unlike radioisotope sources, allowing the use of timing information (time from emission to detection) in detector responses. One of the key goals of this work was to investigate whether this response could be useful for hydrogen content prediction.
- It has been demonstrated here from GEANT4 simulations that across a range of hydrogen indices up to around 0.08, this timing distribution is proportional to the hydrogen content.
- The timing information of DT sources could be used to challenge AmBe sources in hydrogen content evaluation. This will be tested further with a prototype detector using the aforementioned test stand.
- Positional information was also fitted showing potential benefit of additional segmentation in detectors. The feasibility of this for converter foil based detector designs will be explored in the next chapter.

Chapter 4

Understanding Optical Readout in Mixed-Field Cylindrical Detectors for PSD

To build a prototype detector capable of measuring the neutron and gamma distribution in a borehole, several possible detector designs were explored. The detector development in this work will aim to:

- Explore low-cost options for mixed-field borehole radiation detection in the context of formation evaluation for the oil and gas industry.
  - The proposed detector will consist of plastic scintillator coupled to thermal neutron converter foils.
  - The detector should have good neutron-gamma discrimination evaluated using a figure of merit and low misclassification error.
  - Due to the use of plastic scintillator, spectroscopic gamma techniques will not be used. A converter-foil-wrapped inorganic crystal may offer spectroscopic information, but the cost of a multi-detector tool with inorganic crystals would be significant. As low-cost development is a key goal here, the focus is on plastic scintillators.
  - Coupling of converter foils to plastic scintillator is a novel approach, with foils usually being coupled to wavelength shifters. This novel approach allows for mixed-field detection.

- Principally, the goal is to combine neutron and gamma detection into the same instrument, reducing the required volume of a larger tool. It is also considered that a low-cost neutron-gamma sensitive detector may have applications in other fields.
- Encourage replacement of hazardous chemical radioisotope sources.
- With regards to target parameters, the detector will be deployed within a mock borehole testbed. It aims to show that a prototype using alternative detection methods is sensitive to the water content, demonstrating potential for the use of such detectors in advanced logging tools.

The hostile borehole environment offers a unique challenge for detector development. In addition to standard considerations for radiation detectors, there are further difficulties which constrain designs.

- Tool diameter is limited in narrow boreholes (typically 18-30 cm [7]), and so any detector must accommodate this but still be large enough to capture sufficient statistics.
- Deeper boreholes present further challenges due to high temperatures (often reaching up to 200°C). In this work, plastic scintillators will be used which will likely only be suitable in shallower boreholes at lower temperatures. It is however noted that with the development of new organic scintillators (such as polysiloxanes) suitable for higher temperatures, this prototype could be considered a demonstration of their potential in the industry.

4.1 Mixed-Field Modular Detectors

In order to measure the neutron and gamma population at different positions within the borehole, a suitable detector is required. This work deploys mixed-field detection modules to detect both neutrons and gamma rays within the same detector volume. Within this mixed-field detector, plastic scintillator is coupled to BN:ZnS(Ag) foils, to provide sensitivity to both gamma and thermal neutron radiation. Figure 4.1a shows the basic layout of a simple detector module coupled directly to a photosensor.

Gamma radiation will interact within the bulk scintillator predominantly through Compton scattering (see Figure 4.1b), and thermal neutrons will interact via capture

on ^{10}B in the neutron foils (see Figure 4.1c). Within the converter foils, the resulting neutron capture products from ^{10}B will then induce scintillation in the surrounding ZnS scintillator (as discussed in chapter 2).

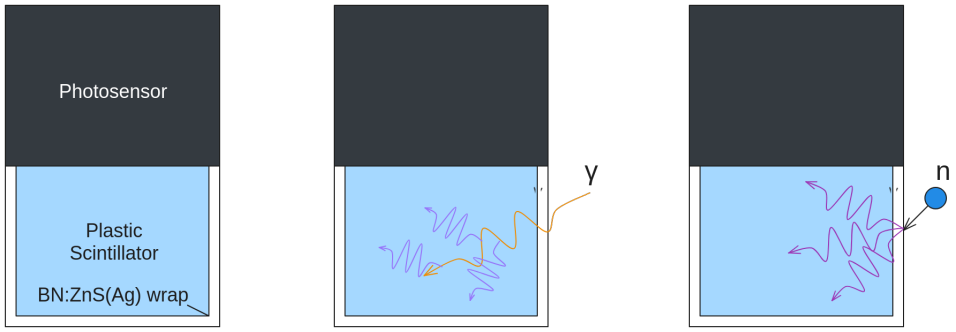

(a) Full Detector (b) Gamma detection (c) Neutron capture

Figure 4.1: Foil wrapped plastic scintillator, coupled directly to a photosensor. Different particles yield different responses in the detector. Purple lines show optical photons generated in the detector.

These different interactions yield different pulse shapes, which can be used to discriminate between particle types. For a gamma ray in the fast plastic scintillator, a short, sharp pulse is observed. Conversely, for a captured neutron in the foil, the ZnS scintillation time profile is characteristically long. The different pulse time profiles allow the use of PSD to separate the particle populations, provided there is sufficient light collection.

Typically, converter foil detectors use wavelength shifting plastic coupled to foils. This is to allow large areas of foil to be coupled to PMTs of smaller aperture, by effectively "turning" a proportion of the light from the foil by 90 degrees, towards a photosensor. However, in this work, at the expense of larger areas of foil, smaller detector modules are built from foil coupled to gamma sensitive plastic scintillator. This allows for a neutron and gamma sensitive detector within one volume, at low cost.

4.2 Proposed Detector Design

Conventionally, compensated neutron porosity logging tools are composed of two detectors (near to and far from the neutron source). In chapter 3, the distribution of detected radiation was shown to be correlated with the hydrogen content of a test rock formation. To capture this distribution, options for position sensitive detectors were explored. An option potentially offering high precision in position resolution is double ended readout, explored in [86]. This system would use a detector monolith with a large neutron foil coupled to a wavelength shifting (WLS) bar, read out by

photosensors at both ends. Based upon the relative intensity of pulses received at each end (or time differences), the position of the detected neutron can be determined. This design requires WLS bars, rather than plastic scintillator, to aid in the transmission of scintillation light from foils onto PMTs at long distances. Gamma count rates were shown in chapter 3 to respond to the variation in hydrogen content of sand formations, and so the use of plastic scintillator is important for this detector. In addition, there can be significant efficiency variation along the length of the detector. Therefore, the decision was made to instead use smaller detector modules in a stack. In this work, it is proposed to increase segmentation for more precise positional information using fibre readout. A design was suggested based upon stacked plastic scintillator modules, each coupled to thermal neutron converter foils, with embedded fibres. These fibres would transmit light from their coupled module to a multi-anode PMT.

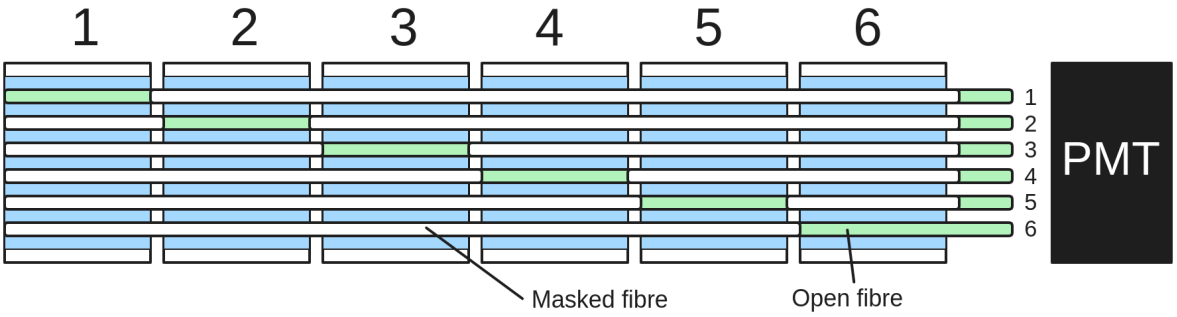

Figure 4.2: Fibre-readout based design for gapless segmented detector. Green shows an exposed fibre, white shows masked fibre. PMT situated on the right, collecting light from all fibres.

Figure 4.2 shows the method of operation, with modules read out from fibres optically isolated from all but one module. Detector segmentation was considered as a possible method to improve the ability of this detector to respond to changes in hydrogen content by providing more granular positional data on detected neutrons and gammas. This design maximises use of the available volume, and allows for better position resolution.

4.3 Detector Module Testing

For the fibre-based design, scintillation light is transported to the PMT via wavelength-shifting optical fibres (BCF-91A [87]) after light has scattered within the bulk scintillator. The transport of a photon to the PMT (particularly in the case of a neutron capture event) requires the crossing of many interfaces and some light may be absorbed in the bulk scintillator. For this reason, discrimination of neutron-gamma events could be affected. PSD relies on the preservation of different pulse shapes from different particle interactions. If a neutron event degrades, it may incorrectly appear as a shorter gamma event.

Correctly classifying pulses as neutrons or gammas is reliant on efficient collection of light and preservation of the scintillator emission time profiles. Therefore a series of GEANT4 [83] optical simulations were performed to investigate the feasibility of different designs proposed. The preferable highly segmented design is illustrated in Figure 4.2. This design would require individual modules to be optically isolated, with scintillation light transmitted by fibres coupled to the edge of each detector module. Light would then be collected by a multi-anode PMT for segmented readout. It is important that pulses read out from fibres preserve the characteristic time profile of neutron or gamma pulses. If too much light is lost, thermal neutron events could be indistinguishable from gamma hits within the bulk plastic scintillator. This would lead to incorrectly classified events from PSD.

In these simulations, directly PMT-coupled detection modules (Figure 4.1a) are also explored as a potential second-choice option to be stacked in a multi-detector system, as shown in Figure 4.3. A simple stack of these modules would be more similar to conventional logging tools. The disadvantage of this method over the segmented design is that each module requires its own photosensor, occupying additional space, with higher cost. However it would still be possible to build a stack of more than two detectors to image the neutron-gamma population with higher granularity than simpler near-far detector systems. This would also allow for simple modification of tool length and detector spacings due to this modular design.

4.3.1 Optical Simulation in GEANT4/CRESTA

GEANT4 [83] is a simulation toolkit for the simulation of the passage of particles through matter. It can also be used to model the optical properties of materials, and

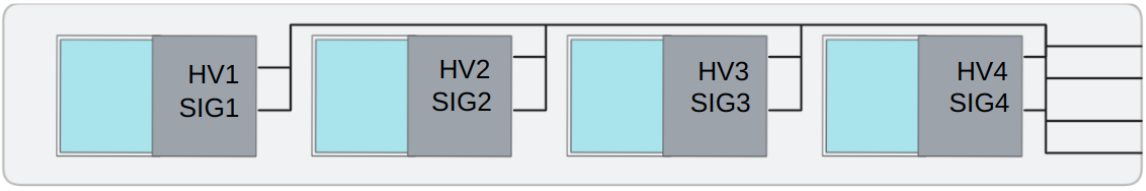

Figure 4.3: Four-detector system chosen for superior PSD capability with direct optical readout from PMTs.

the transmission of optical photons. GEANT4 allows the user to define custom materials and optical properties which can be used in simulation. Optical simulations are used here to examine the light output performance in a mixed-field scintillation detector. CRESTA [84] is a wrapper for GEANT4 which improves the simplicity in setting up complex simulations. A custom optical physics list was deployed within CRESTA/GEANT4. The QGSP_BERT_HP physics list was used, with additional extensions for scintillation, Cerenkov, absorption, and Rayleigh Scattering processes, alongside full optical boundary tracking. Optical data was taken from a combination of material data sheets and spectrophotometer measurements to support these simulations. The geometry contained Eljen EJ-200 [88] plastic scintillator coupled to BN:ZnS(Ag) foil. Plans were made to cast custom scintillator as part of this work to quickly test different geometries. As part of initial work on fast prototype scintillator manufacturing, pour depth was found to be limited to 5 cm, as the epoxy mixture used can exotherm (undergoing rapid uncontrolled heating) above this depth, causing poor sample quality. Though repeated pours may be possible to achieve higher depths, these plans assumed a 5cm depth limit, and therefore this simulation geometry used a hemicylindrical scintillator of 5 cm radius, wrapped in converter foil. Fast prototyping of scintillators is discussed in detail in chapter 5. Figure 4.4 shows a simple geometry setup in which the PMT is coupled directly to the detector.

A flux of monoenergetic thermal neutrons (0.025 eV) was fired at the combination and the resultant optical photons collected on a PMT. In addition to sensitivity to incident gammas, it was found that the plastic scintillator itself exhibits sensitivity to thermal neutrons through capture on hydrogen. Either a thermal neutron capture event occurs within the foil, or the neutron is captured within the scintillator, producing a capture gamma from hydrogen. In each case, scintillation may occur, either within the foil itself or the bulk plastic scintillator. These two cases were used to test the PSD performance from the same incident flux. Events are labelled as “true” neutrons

or gammas from simulation data, and compared later with the predicted classification based on PSD. Optical photons were simulated, and a PMT sensitive detector used to record detected photon hits. These photons are recorded in position, energy, and time. It was also necessary to account for the Quantum Efficiency (QE) of the PMT as a function of photon wavelength, as this significantly reduces the actual number of detected photons. The quantum efficiency curve for the H8711A PMT is visible in Figure 4.5 against the emission spectrum of POPOP. Figure 4.6 shows the same QE curve against the emission spectrum of ZnS. This is a multi-anode PMT which would be suitable for fibre-based detectors, and so is used as a model in this simulation.

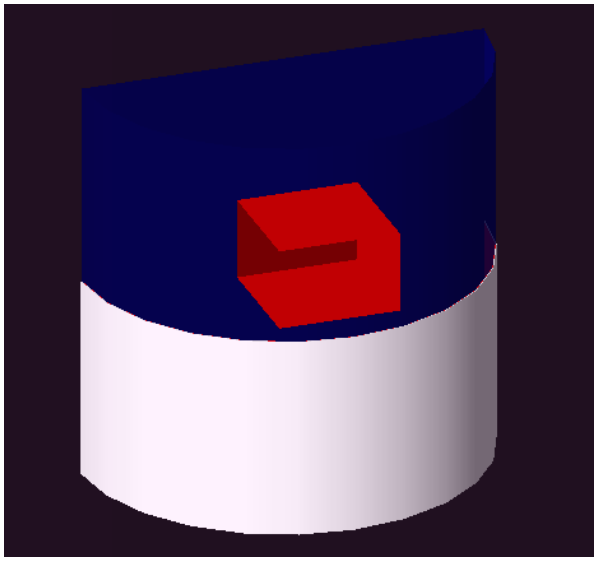

Figure 4.4: Simple setup consisting of plastic scintillator wrapped in converter foil, white. This detector is directly coupled to 3 × 3 cm PMT (red).

A rejection sampling approach was applied to incoming photons for quantum efficiency. In the case of a direct PMT-scintillator interface, losses from quantum efficiency reduced the total number of photons detected across all events by approximately 80%. This is to be expected, with 20% QE generally considered standard for PMTs.

A form of "pseudo-PSD" is possible with the raw PMT hit data, taking the ratio of hits in different time ranges. However with only integer values possible, this results in discrete values of the PSD parameter. Therefore a more complete approach was deployed and photon hits were used to generate realistic PMT pulses. Each photon was assigned a randomised transit-time in the photomultiplier based upon the spread from Hamamatsu datasheets [89] (12 ns transit time with a 0.33 ns spread). The

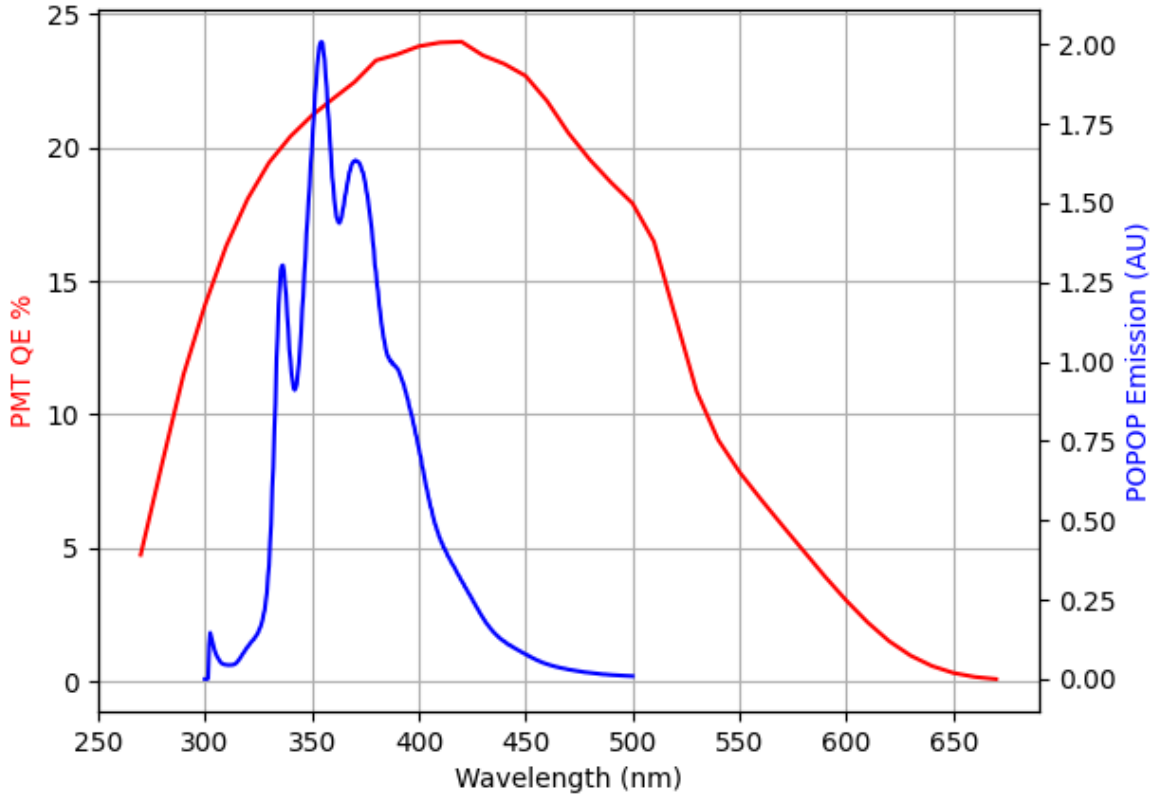

Figure 4.5: Quantum efficiency curve for Hamamatsu H8711A multianode PMT [89] compared against POPOP emission spectrum [90].

resultant collection of photon hits was then convolved with a Single Photoelectron (SPE) response, and amplified assuming a front-end normally distributed gain of 10 (to simulate use of a fast amplifier). Finally, baseline noise jitter was added based on typical experimental setups (Gaussian noise with $\mu = 0$ and $\sigma = 0.5\,\text{mV}$). Figure 4.7 shows the pulse processing procedure.

An example pulse carried through this process is shown in Figure 4.8 and Figure 4.9. Figure 4.8 shows the simple, pre-processed hit data, showing photons that would produce a response in the PMT after QE losses are accounted for. Figure 4.9 shows a more realistic pulse, in which this hit data has been converted into the characteristic PMT pulse expected from thermal neutron converter foils.

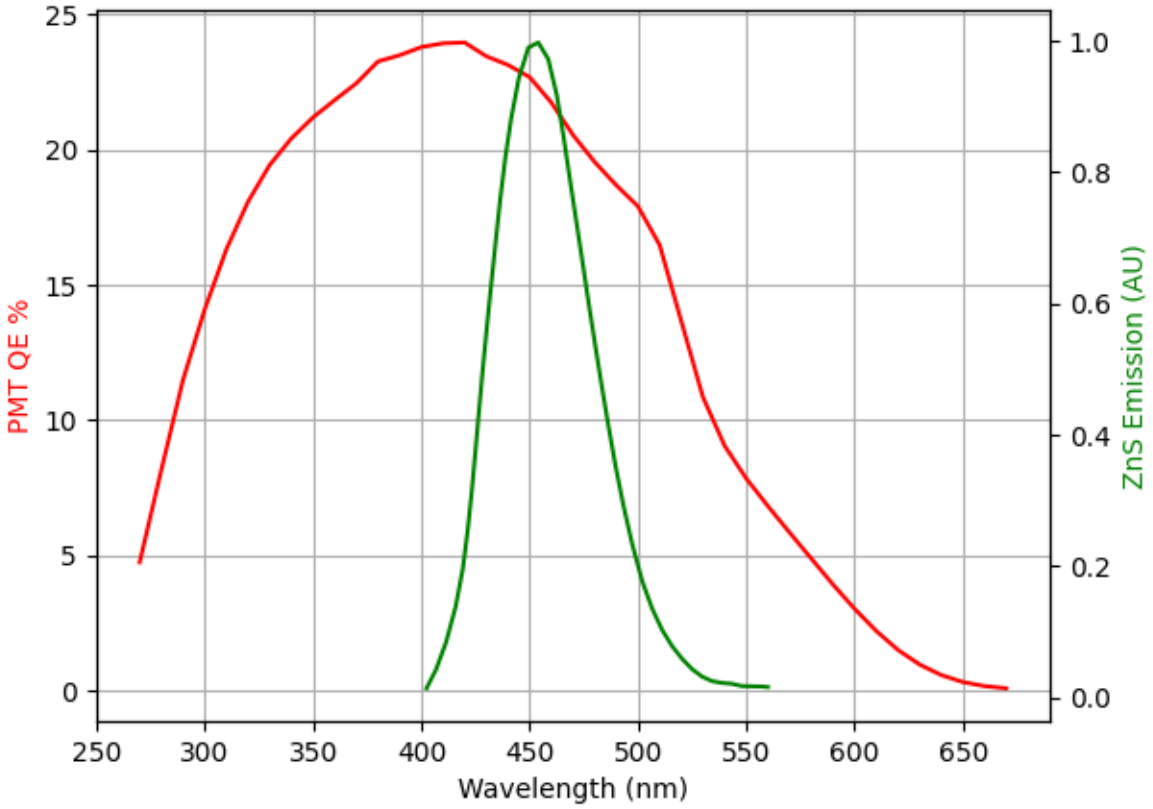

Figure 4.6: Quantum efficiency curve for Hamamatsu H8711A multianode PMT [89] compared against ZnS emission spectrum [90].

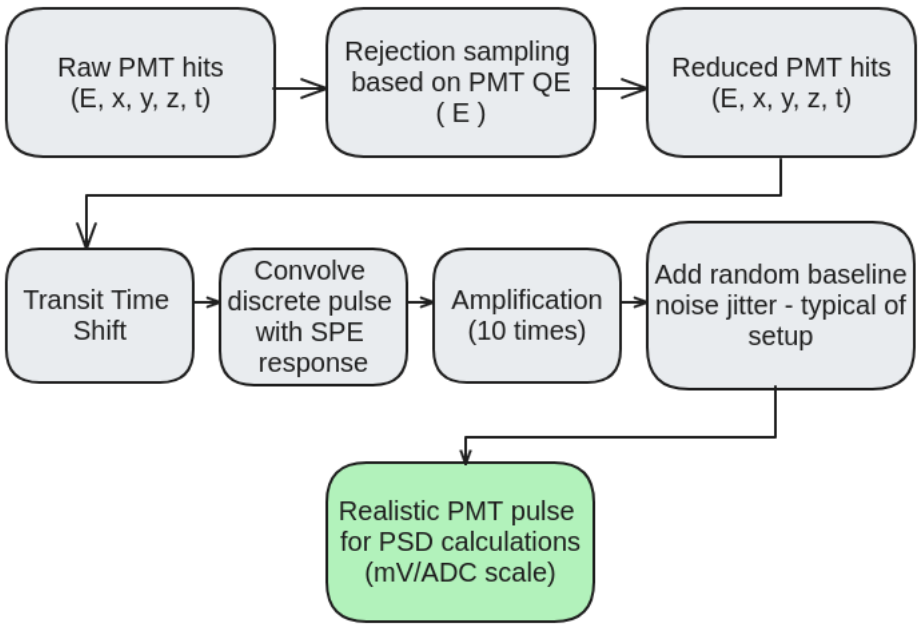

Figure 4.7: Pulse processing for raw PMT hits within optical simulation for realistic pulse construction.

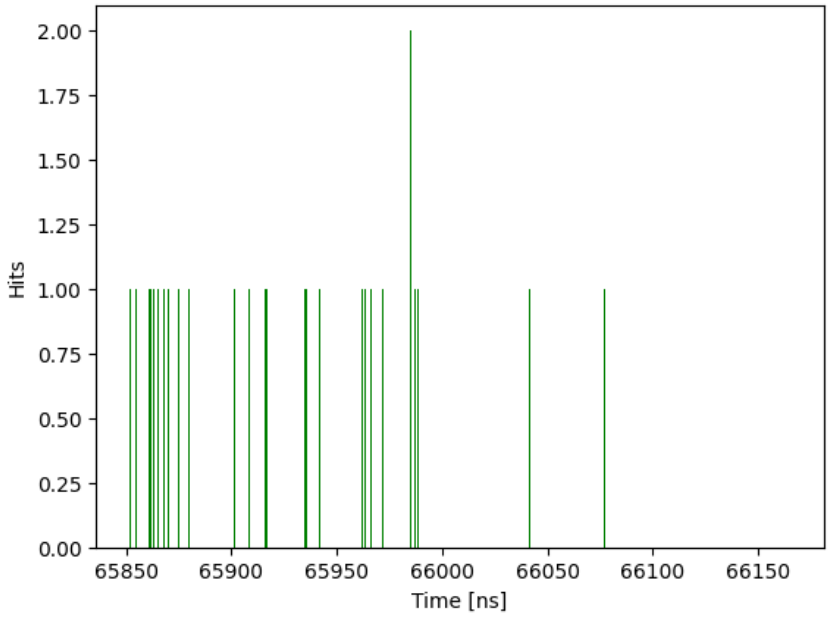

Figure 4.8: Raw PMT hits after QE filtering from a simulated event.

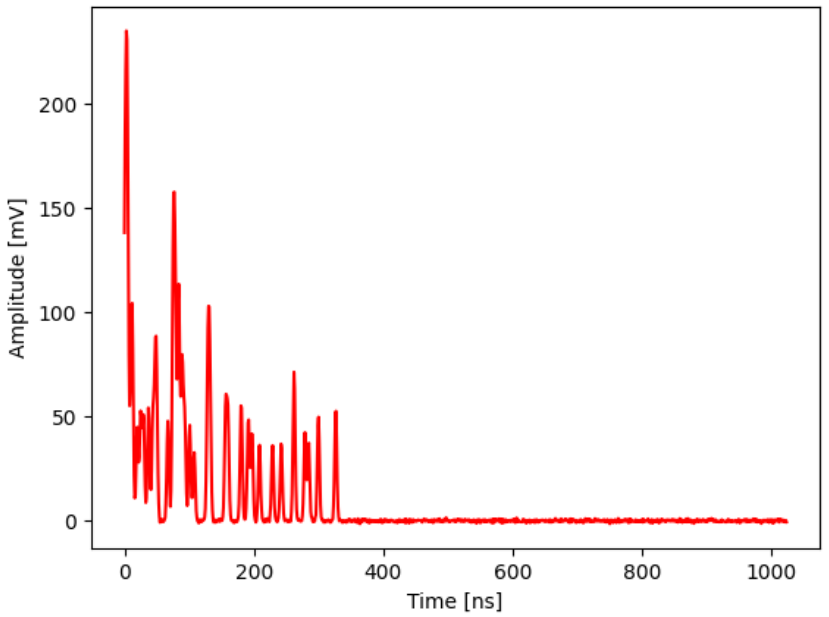

Figure 4.9: Simulated PMT pulse generated using raw hits from Figure 4.8 carried through transit time shift, SPE response, amplification, with baseline jitter included.

Following the generation of realistic pulses from the PMT hit data, PSD

calculations were applied to the collection of simulated events. PSD was performed using the standard long-short gate integration approach outlined previously to extract PSD ratios.

Following this approach, simulations were performed to examine the following setups:

1. Directly coupled PMT-Scintillator-Foil. Success with this method would demonstrate capability for PSD in low-cost coupled plastic-scintillator-BN:ZnS(Ag) combinations.

2. A geometry with embedded fibres within the scintillator. BCF91-A WLS fibres are capped with a PMT within simulations to examine the potential light output using this geometry. Up to 8 fibres were added at 10 degree intervals around the radius of the hemicylinder. The performance of this setup will dictate whether a highly segmented tool design as in Figure 4.2 is feasible.

3. Fibres were removed incrementally from the geometry configuration in (2) to observe the impact upon PSD capability.

Performance was judged based upon the quality of the figure of merit for discrimination. The misclassification error is also reported by comparing the PSD result to the true particle information from the simulation.

Direct-Coupled PMT-Scintillator-Foil Combination

Simulations were first performed with a 3×3 cm PMT face placed directly upon the top scintillator face. The curved edge of the hemicylinder was encased in BN:ZnS(Ag) foil with a 100 µm airgap. All other edges were forced to 100% reflectivity to simulate perfect containment of optical photons. Incident particles were generated from a source box situated adjacent to the detector, from the BN:ZnS foil side. Pulses were generated using the aforementioned algorithm, and PSD parameters calculated. The data in Figure 4.10 shows the detector response in terms of the logarithm of PSD ratios.

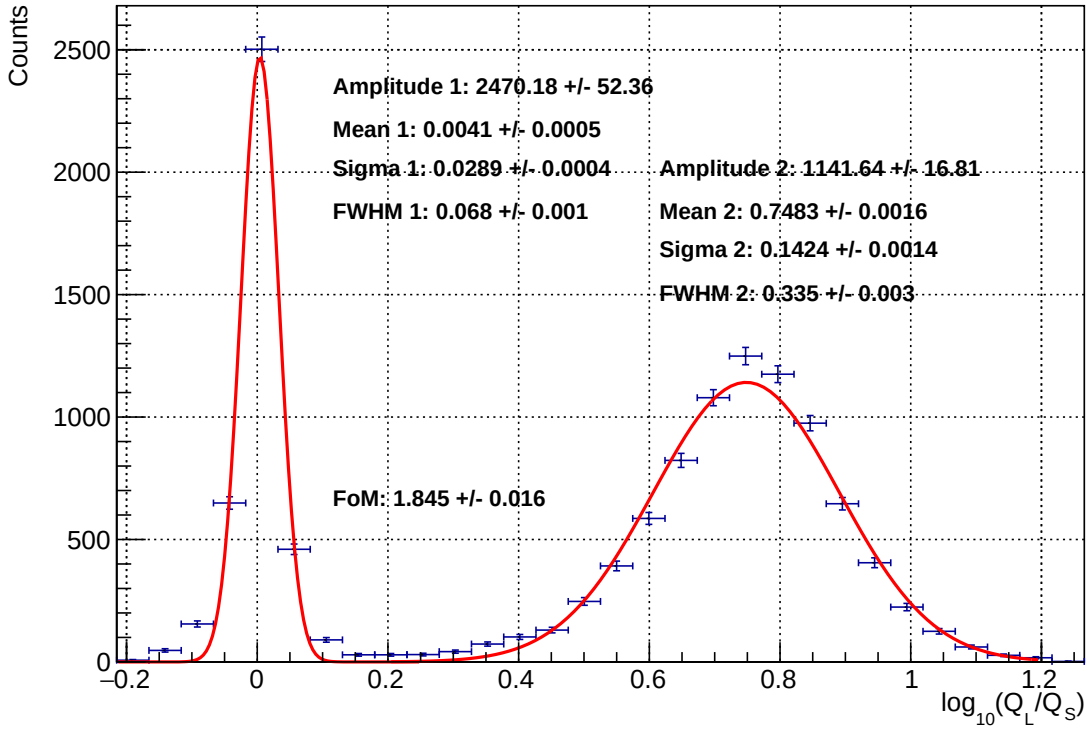

Figure 4.10: PSD long-short ratio histogram (15 ns short gate with 1000 ns long gate) for direct readout from hemicylindrical scintillator module. Gamma peak (left) and thermal neutron peak (right) with good separation.

Evidently, a clear, separated peak is visible for thermal neutron events at higher PSD ratios. This demonstrates that the time profile of pulses from the foil, and the number of photons present, are sufficient for PSD in this detector system. A FoM of 1.845 ± 0.016 was achieved for this detector configuration with direct readout, using Equation 4.3.1. This value is characteristic of a good neutron-gamma discriminator. The figure of merit, as described in Equation 4.3.1, is used to consider both how far apart two populations are (see top of fraction) and how sharp those peaks appear (see bottom). Two well separated, sharp peaks, will have a higher figure of merit than two wider peaks which have smeared into one another. However, the FoM alone is not fully representative of the detector's discrimination quality, and it is necessary to also consider the misclassification error.

$$FoM = \frac{PSD_n - PSD_\gamma}{FWHM_n + FWHM_\gamma} \tag{4.1}$$

For the data in Figure 4.10, a sensible cut value can be selected on the PSD parameter to define particle populations. In doing so, there is inevitably a misclassification error. In this instance, the misclassification errors for a selection of cut values is shown in Figure 4.11. The PSD cut value determines the value above which a detected particle is classified as a neutron (and by elimination, what remains is classed as a gamma). For a gamma, it is typically expected that the bulk of the pulse is contained in the short time window, and so the logarithm of the long integral divided by the short should be just above 0. Figure 4.11 shows that for an optimised PSD cut, the total misclassification error is low, at 1.8%. This plot is similar to a ROC curve, in that it displays the false positive rate. However, this shows the false positive rate as a function of the PSD parameter, separately for both neutrons and gammas to give a complete picture.

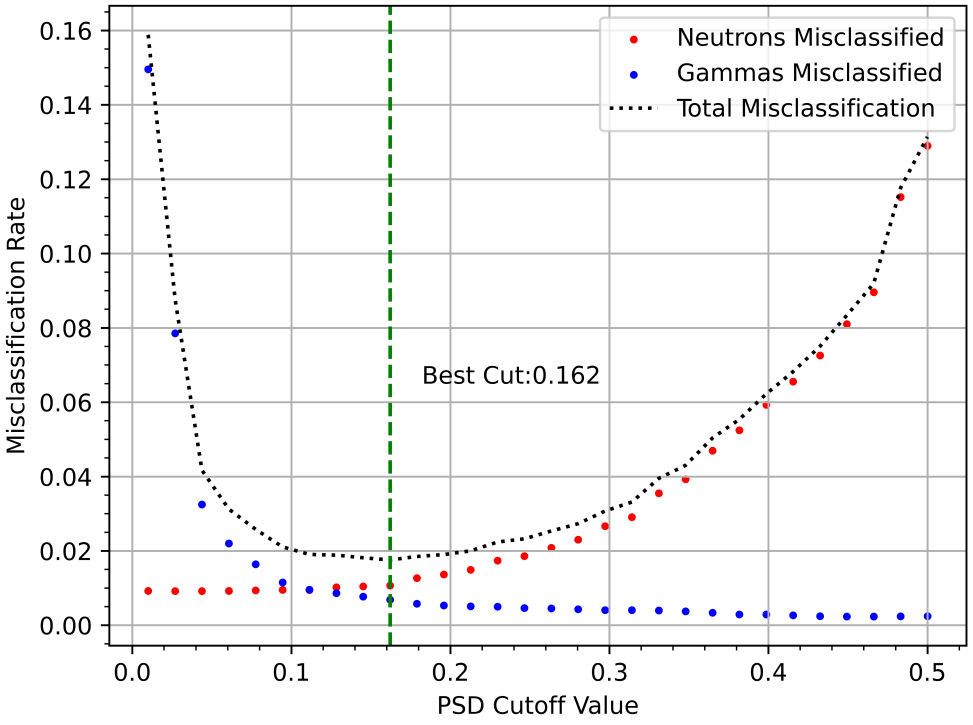

Figure 4.11: Variation in the misclassification rate for classification of neutrons and gammas as the PSD cut value is varied. The optimal value marked in green shows the lowest total misclassification for both classes at 1.8% when cutting at 0.162.

It is therefore evident that a direct readout system using plastic scintillator

coupled converter foils is capable of PSD with low misclassification error. This detector therefore shows promise as a low-cost combined neutron-gamma detector with customisable geometry. Low-cost mixed-field detection with opportunity for fast-prototyping of practically any geometry (considering size constraints) may be of interest within other areas of nuclear monitoring.

Simulated Fibre Readout

No issues were observed based upon simulations when reading out with the PMT coupled directly to the scintillator. The large coupled area would suggest ample light output for PSD, as confirmed by simulation. The proposed detector design in this work (Figure 4.2) however would not allow for direct readout upon the face of the scintillator. Light emitted by ZnS in the foil after a neutron capture event will be transmitted into the scintillator block, undergo scattering within the scintillator and be collected by a WLS optical fibre. This fibre can then transmit light onto the PMT at an extended distance from an optically isolated detector module.

Simulations were performed to examine the extent to which fibre readout would degrade light output from the combined neutron-gamma modules. It is important that the light output time profile from neutron and gamma events is suitably distinct, such that pulse shape discrimination is achievable with a good figure of merit and low levels of misclassification, as in the case of direct readout. The simulation geometry was set up as in Figure 4.13. This example shows a setup with just two fibres present. The prototype cast scintillator for this setup is shown in Figure 4.12 for comparison.

The BN:ZnS foils have a light output of 47,000 photons per MeV energy deposited. The event in Figure 4.14 shows a neutron capture event, towards the right of the block, followed by photons undergoing total internal reflection within four coupled WLS optical fibres. In the first instance, eight fibres were coupled to the detector module and directed towards a PMT in GEANT4. Fibres were then removed for subsequent simulations to observe degradation in the light output time profile.

The plot in Figure 4.15 shows the PSD histograms for 8, 6, 4, and 2 fibre configurations. Evidently, with fewer fibres present, the PMT collects fewer photons, and PSD suffers. The degradation in PSD quality is obvious from the smearing of the neutron and gamma distributions into one another - with worsening figure of merit.

At first glance, though the PSD appears to be worsening for fibre readout, it is possible to pick out separated populations, even in the case of just two fibres.

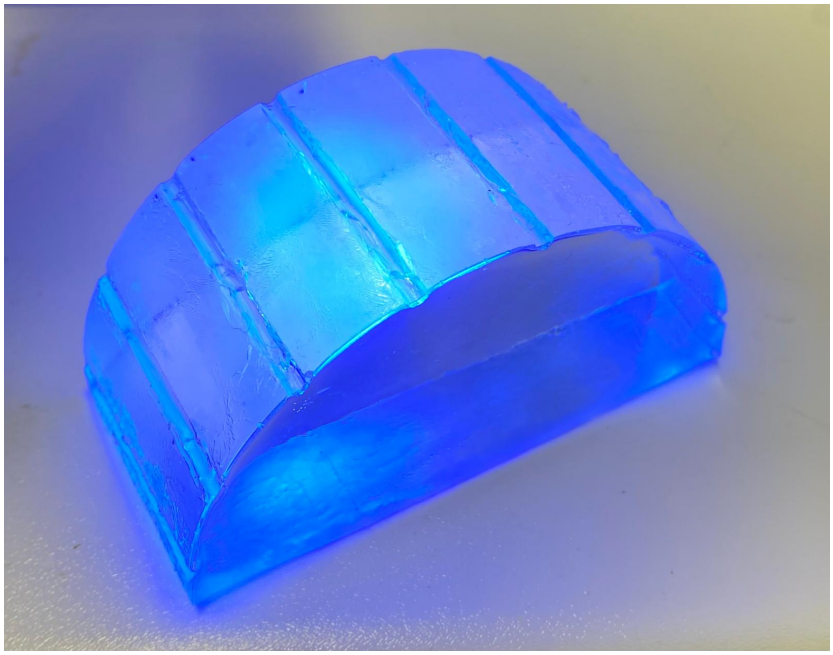

Figure 4.12: Prototype cast of scintillator geometry with fibre grooves.

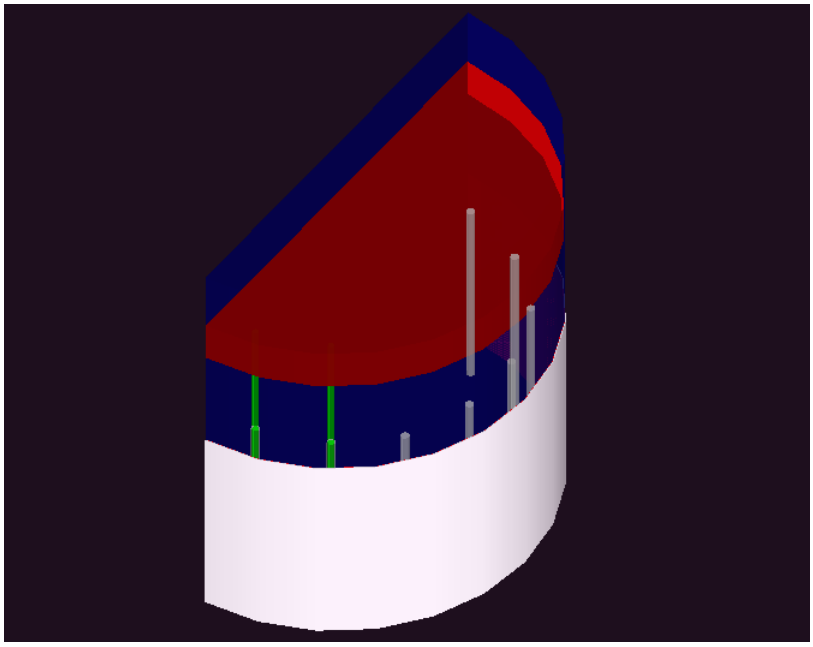

Figure 4.13: Simulation setup showing two of eight possible fibres within grooves. White exterior shows thermal neutron converter wrapping. PMT sensitive area in red caps all fibres.

However, as before, it is necessary to consider misclassification errors. A hint that misclassification is significant in the case of fibre readout is the ever growing low PSD

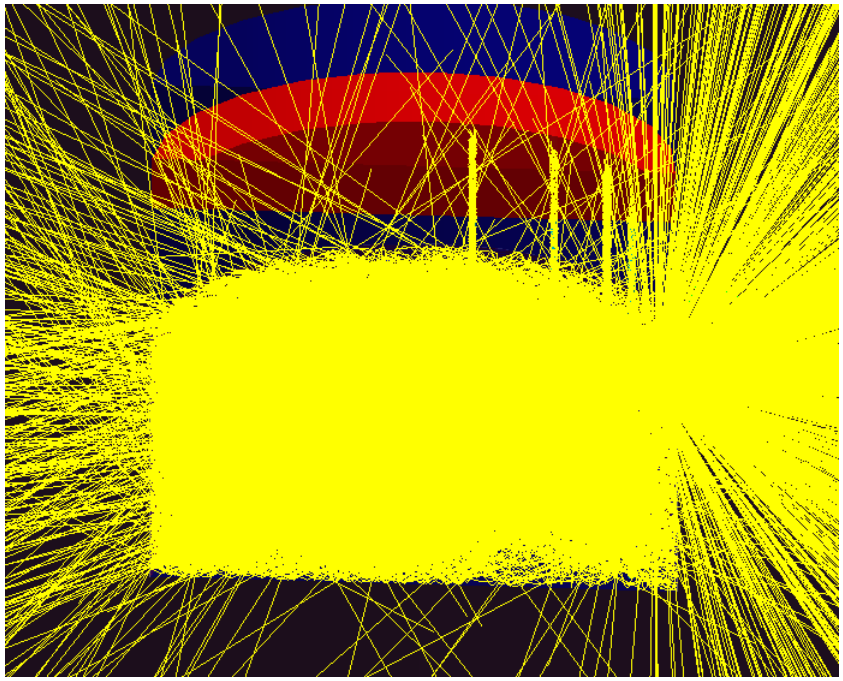

Figure 4.14: A neutron capture event within the foil produces scintillation photons (yellow). The photons travel through the bulk scintillator, and some travel into the optical fibres and undergo total internal reflection. This setup contained four fibres.

peak around zero in Figure 4.15. As the number of fibres is reduced, the first peak grows as the two populations smear together, suggesting that many neutron events are being misclassified. Instances of high light output neutron pulses decaying would trivially be expected to be higher where the potential for optical losses is greater (i.e fewer fibres available to transport light onto the PMT).

Plotting the misclassification rate for each particle, this time for an eight-fibre combination, shown in Figure 4.16, reveals issues with this method of readout. Notice the significant increase in misclassification rates when compared with direct readout in Figure 4.11. Another point of comparison should be considered where the PSD value is particularly low. It would be sensible to expect the neutron misclassification to die off to zero for low values of the PSD parameter, since these values should correspond to short, fast events typical of a gamma. In fact there is an uptick for low PSD values in the neutron misclassification rate, signifying a contamination of the low PSD value region with neutrons. Many of the neutrons detected have pulses which have degraded significantly due to optical losses, so much so that they now appear to be shorter gamma pulses, with the bulk of their area in the short time window.

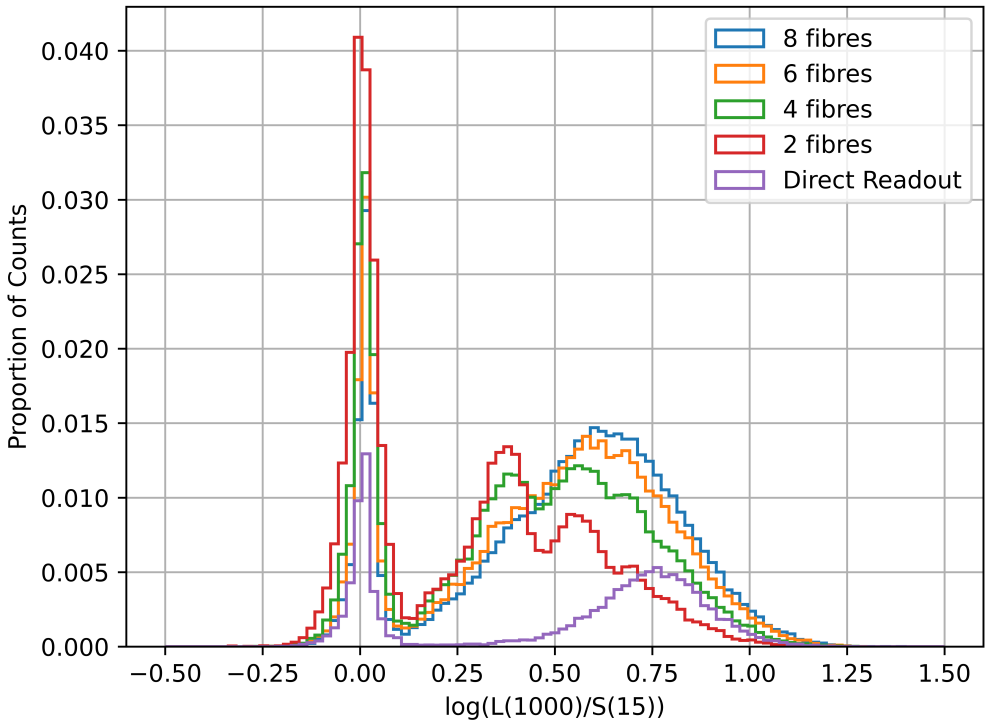

Figure 4.15: PSD histograms are shown for 8, 6, 4, and 2 fibre combinations. Also shown (in purple) are the noticeably better separated, more clearly Gaussian peaks yielded from direct PMT readout.

It is possible to plot misclassification rates for all fibre combinations and extract the best possible performance based on an optimal cut value. Table 4.1 shows the misclassification errors for the best PSD cut values available for different fibre combinations. Realistically, the maximum number of fibres that could be used per optical module is four. To use the multi-anode PMT pixels as individual channels, a single pixel must be connected to many fibres from a single module. The pixel size of 4.2 square mm, visible in Figure 4.17, could accommodate up to four 1.5 mm diameter fibres per pixel. Evidently, the detector response for such an arrangement is unacceptable. Large levels of misclassification occur, even within the perfect conditions offered by simulation.

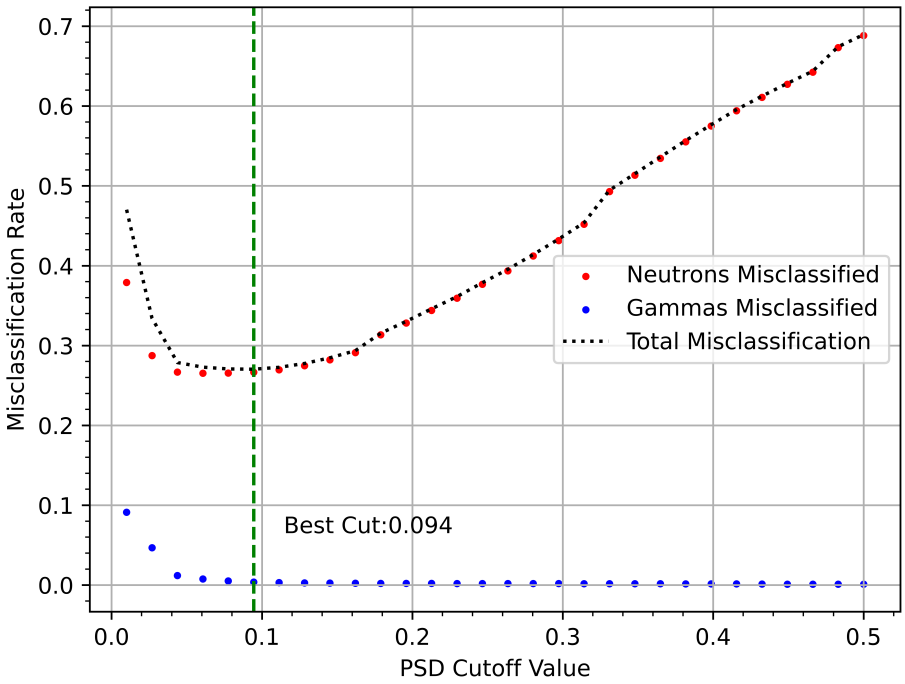

Figure 4.16: Misclassification in an eight fibre system. Many more neutron events decay to the point at which the long integral is equivalent to the short. This results in a 27% misclassification rate at the best cut value.

Detector Configuration	Optimal PSD Cut	Total Misclassification
Direct Readout	0.162	0.018 ± 0.03
8 Fibres	0.094	0.27 ± 0.01
6 Fibres	0.077	0.36 ± 0.01
4 Fibres	0.094	0.53 ± 0.01
2 Fibres	0.128	0.72 ± 0.01

Table 4.1: Detector PSD performance for different detector configurations. Errors rounded up to closest 1 percent.

Alternative LiF:ZnS(Ag) foils

This work also considered that there is potential for fibre readout if it was possible to improve the light output from thermal neutron captures. In fact, LiF:ZnS foils offer more energy from charged capture products (4.76 MeV for lithium-6 compared with 2.79 MeV for boron-10 [91]), and so are able to elicit emission of around twice the number of photons from ZnS. These foils are more commonly used over boron-10

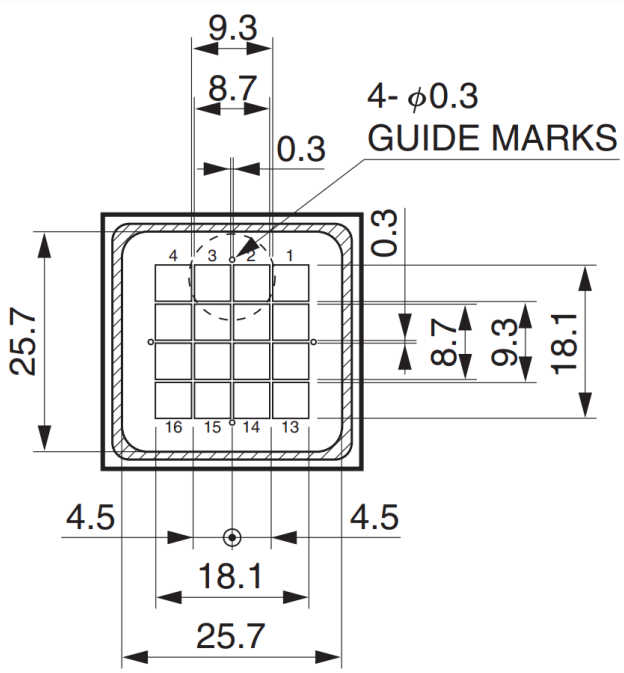

Figure 4.17: PMT dimensions for H8711A pixel layout.

based foils, though they are significantly more expensive. The same simulations were performed with LiF based foils. Though this would offer some improvement in the light output, it is unlikely to offer any significant fix to this issue.

Figure 4.18 shows that there is some improvement in the PSD for a detector configuration consisting of four fibres when using lithium foils, which would fit within a single pixel of the multi-anode PMT. Split peaks are no longer observed in the neutron population due to discretisation from low photon counts. Misclassification also improves by approximately a factor of 2, down to 26% from 53% in boron-10 foils. However, the misclassification (Figure 4.19) again reveals an unacceptable proportion of neutrons incorrectly identified as gamma events. Even with higher light output, the degradation of neutron pulses is such that the gamma population is contaminated.

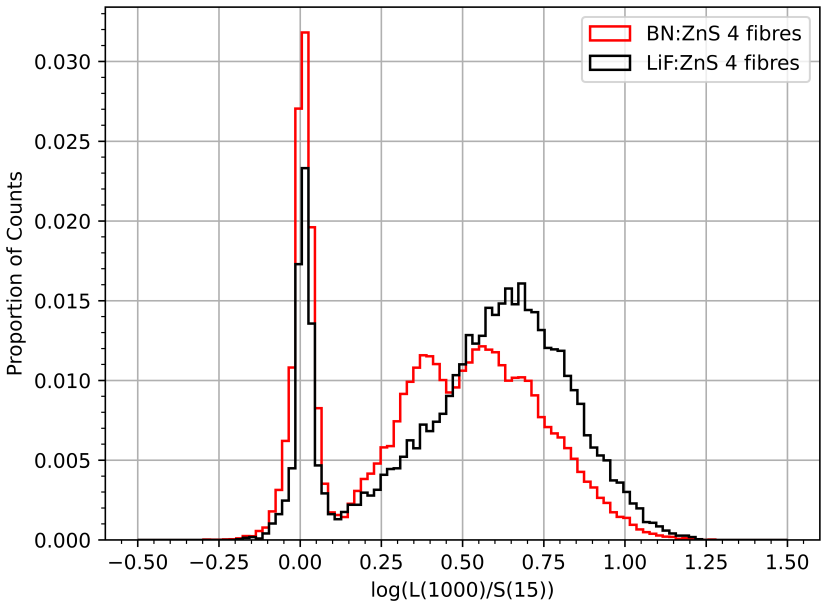

Figure 4.18: Relative performance of boron and lithium based foils.

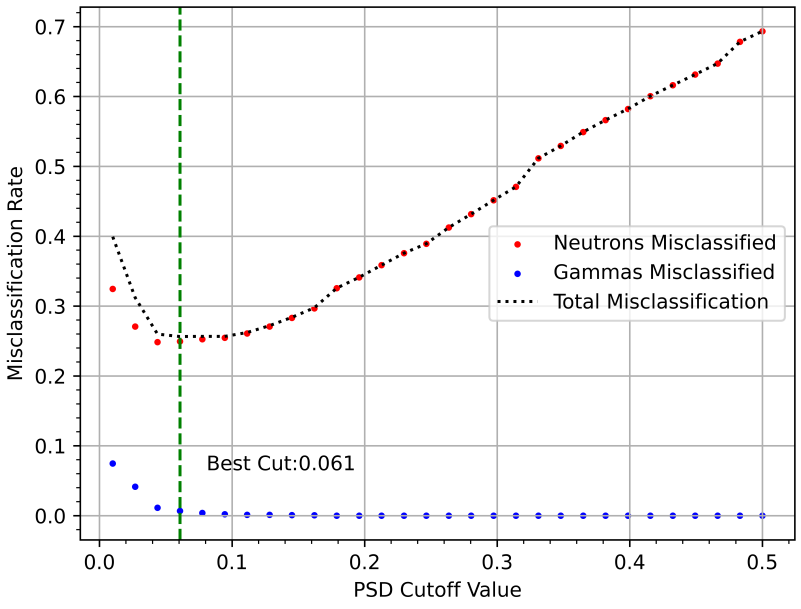

Figure 4.19: Misclassification for a four-fibre detector configuration using lithium-based foils. The additional light output was not sufficient to bring down misclassification to an acceptable level. Minimum total misclassification did improve to 26% from 53%.

These misclassification errors are unacceptably high for a combined neutron-gamma detector. Unfortunately, this conclusion means that the detector design should instead use direct PMT readout of foil-wrapped scintillator modules. This will prevent the detector from having higher levels of segmentation up to 16 channels using fibre readout. Without fibre-based readout, it is now necessary to also account for housing the physical volume of PMTs used as part of the detector tool, and so the sensitive detector volume available is reduced. The chosen detector design will be laid out as in Figure 4.3.

To summarise:

- Foil-wrapped plastic scintillator works well, with good figure of merit, as a low-cost combined neutron and gamma sensitive detector, provided light is read out directly with a PMT coupled to the bulk scintillator.
- In attempts to produce segmented detectors with this detection method, fibre readout introduces significant levels of misclassification in PSD due to poor light collection on the PMT, cutting out the long tail from neutron events.
- Fibre readout is therefore unfeasible for a detector with such dependence upon preservation of light output time profiles, and so direct PMT readout is necessary.
- SiPMs were considered as an alternative due to their small form-factor, but due to their well-documented performance degradation at higher temperatures [92], and the existence of readily available high-temperature ruggedized PMTs in industry, designs compatible with existing technology were considered more appropriate.
- Detector designs will proceed with larger sub-modules, and lower segmentation. Foil-wrapped scintillator will be coupled directly to PMTs.

4.3.2 Detector Sub-Module Length Simulation

With decisions made to move to directly-coupled PMT readout, it was necessary to explore the limits on the length of cylindrical detector sub-modules before casting. With around 1 metre of detector volume to occupy, part of the decision on detector composition (number of individual detectors/modules) will be informed by results from simulations on detector response to hydrogen content. However, it is necessary to also understand the optical limits for certain lengths of individual detectors. For example, a longer detector is likely to introduce pulses which could originate from captures at

longer distances from the PMT. These pulses may degrade or be absorbed completely along their path to the PMT, causing similar issues to those encountered with fibre readout. Therefore, simulations were performed to examine the PSD capability when events are read from different positions along the length of the detector, and understand any degradation.

Simulation Geometry

The EMI 9954 [93] PMTs available for this work have a diameter of approximately 5 cm. Therefore, the following section will examine optimal detector length for a scintillating cylinder of diameter 5 cm. This will allow for direct coupling of the full sensitive area of the PMT.

A geometry consisting of a foil-wrapped cylinder of plastic scintillator was bombarded with a thermal neutron flux. The setup was capped with a PMT of diameter 5 cm, matching the EMI 9954 PMTs which will be used in the detector prototype.

Initially, a 5 cm diameter cylinder of length 1 metre was simulated under thermal neutron flux. A length of 1 metre was estimated to be long enough to demonstrate the extreme case of very poor neutron discrimination. The same pulse processing procedure as outlined in Figure 4.7 was applied to events. The aim was to investigate the optimal length of a detector module. Events at an extended distance from the PMT are likely to encounter significant absorption, and so are at risk of optical degradation. Therefore, it is necessary to understand:

- How many neutron events fail to register a pulse in the PMT, and where do they originate relative to the PMT?
- Of the neutrons that do register a pulse, is the resulting waveform sufficient to reliably perform PSD?
- If not, how far away from the PMT did these events originate on average? Is there a limit beyond which misclassification grows significantly?

For optimal length, the ideal detector is large, such that it has as much active volume as possible, but the detector must also demonstrate accurate discrimination of neutrons. Therefore, total misclassification of neutron events as gammas is a sensible choice of metric. From this simulation, different detector lengths were examined to

investigate how length impacts misclassification. Here, smaller hypothetical detectors are sliced from a larger monolith. Therefore, any benefit from reflections at the far edge will not be observed. There may be some improvement to be observed in smaller detectors which are capped with reflective material.

Long tail neutron events in a 1 metre detector were selected specifically and the resultant pulses from these events integrated to generate a long/short ratio.Figure 4.20 shows a collection of neutron event hit positions (along the full 1 metre detector length) and their associated logarithmic PSD ratios from simulation. This shows the failure of neutrons hitting the detector farther from the PMT to register a significant pulse with a long-short ratio that would typically indicate a neutron.

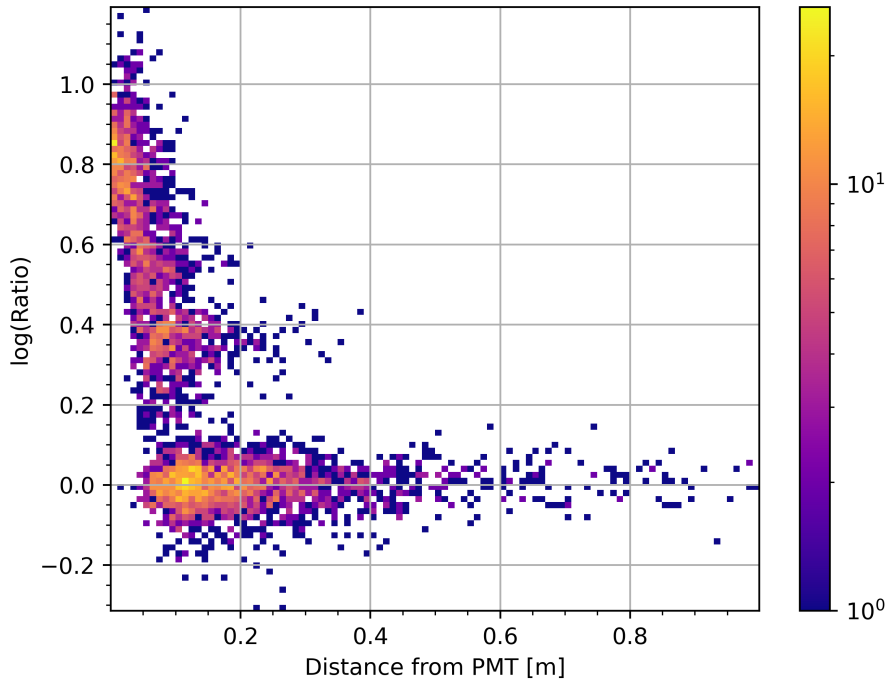

Figure 4.20: PSD ratios for neutron events arriving from different z positions along the length of the detector monolith. PSD suffers with distance from PMT. Ratios should be high for neutrons.

The heatmap, which shows neutron events, suggests poor PSD capability at lengths above around 5 cm. Neutron pulses, which should have characteristically high PSD ratios, begin to appear as short, fast events with low PSD ratios (with a long component around 0). At higher detector lengths the number of events recorded also

drops significantly. This is due to waveforms which decay to the extent that the PMT records no pulse. Figure 4.21 shows the fraction of neutron events failing to register a single photon hit on the PMT for each possible detector length. This increases linearly after around 10 cm in length.

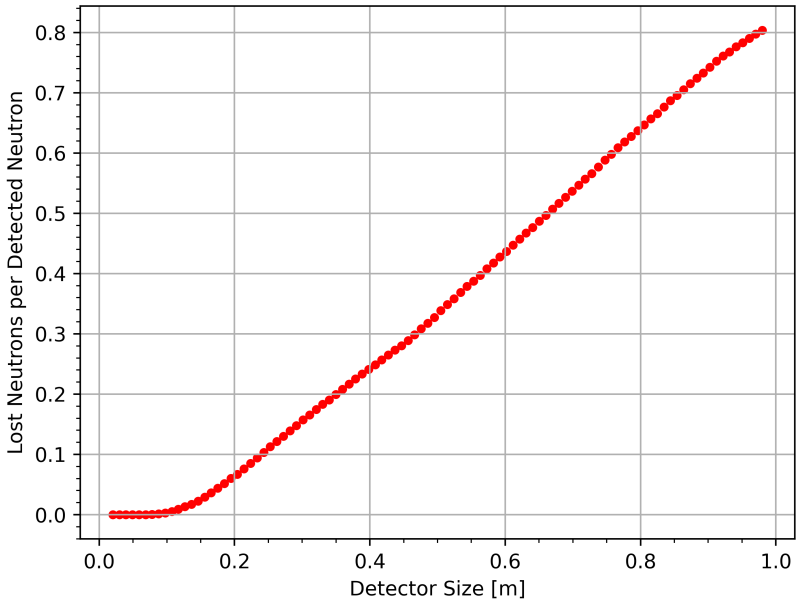

Figure 4.21: Fraction of neutron events depositing energy in foil that fail to register hits at the PMT versus detector length

There is a noticeable increase in lost events at 10 cm, but as seen in Figure 4.20, even for events registering pulses, discrimination may not be possible. For a standalone neutron detector, there is diminishing efficiency returns on increases in length. However this is a mixed-field detector. The main issue is that increasing the length of the detector introduces contamination of the gamma population with degraded neutron pulses. Therefore, it is necessary to look more closely at how misclassification grows with length to make decisions on detector geometry.

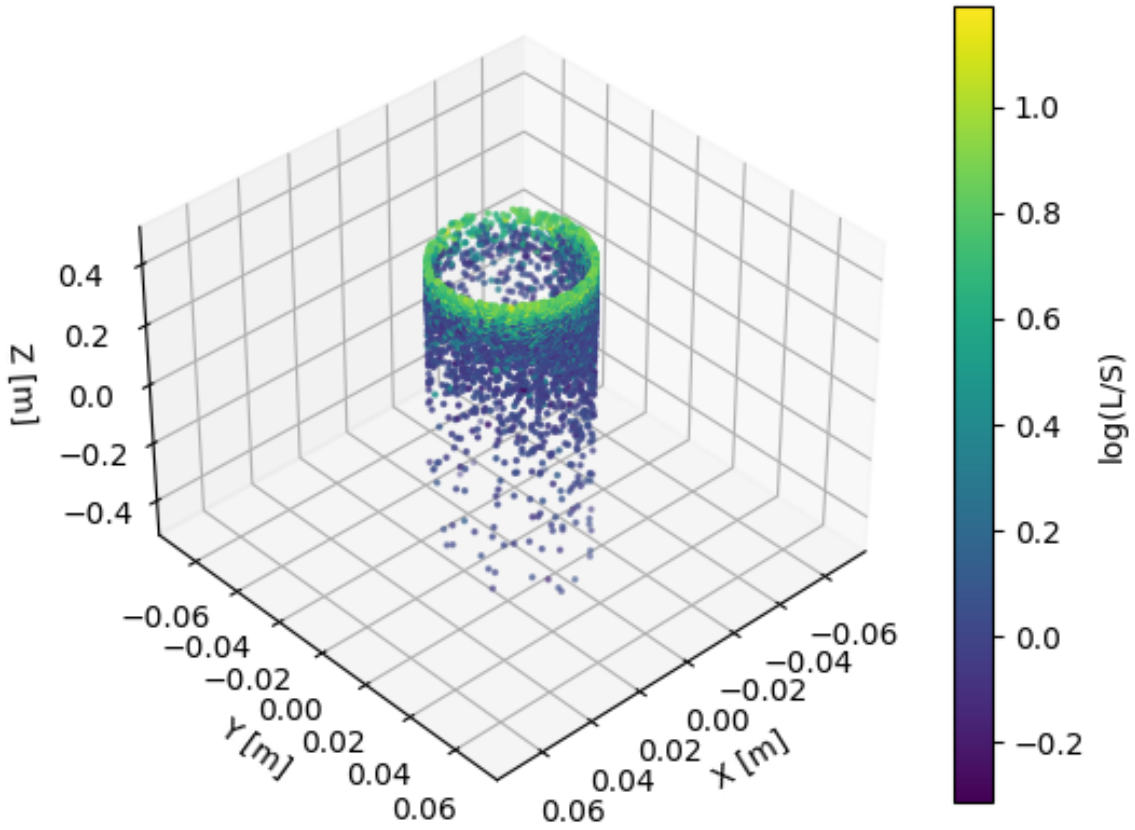

Figure 4.22: Marked neutron hit positions from simulation, colour coded according to the measured long-short ratio from the simulated pulse.

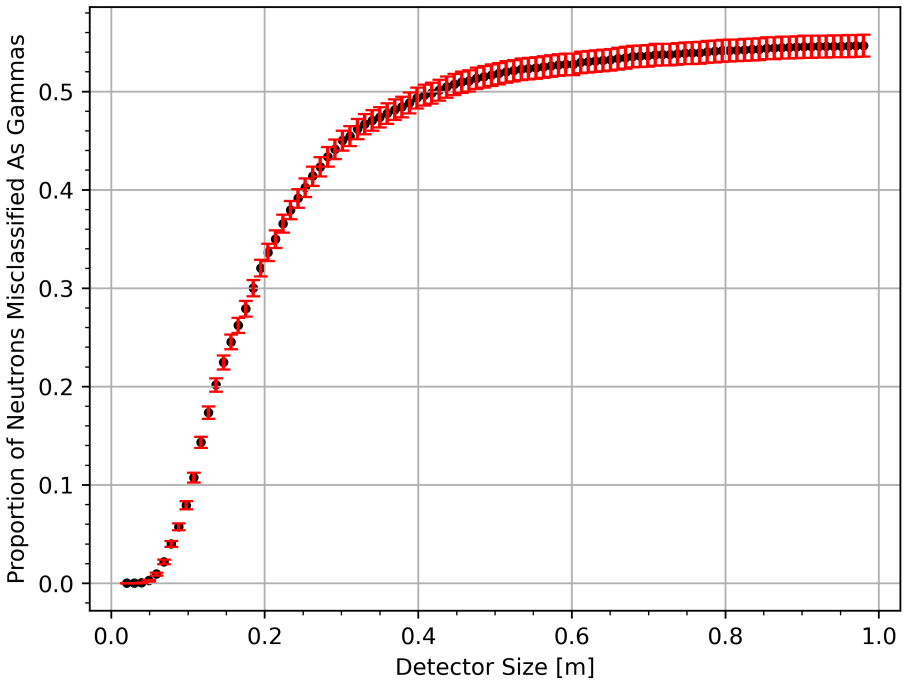

Figure 4.23: Misclassification rate starts to increase at 5cm detector length before growing sharply around 10 cm, contaminating the gamma population for discrimination

Figure 4.22 shows the hit positions for neutrons within the converter foil wrap, and is color coded for the measured ratio. It is evident that as events move further away from the PMT, they are far less likely to result in a sensible value of the PSD parameter for a neutron event. Also notice the reduction in event density with increasing distance away from the PMT (top). There is a discernible "ring" of good events below approximately 10cm. Figure 4.23 goes a step further to show the misclassification of neutrons against detector length, for a logarithmic long/short ratio cut of 0.2. Above 5 cm, the proportion of misclassified events begins to grow. Based on these simulations, with detector dimensions of 5 cm diameter and 5 cm length it is reasonable to have confidence in the pulse profiles for PSD. Therefore, 5 cm cylinders were selected for the detector modules in this work.

It may be possible to further improve these results by the addition of reflections. Currently, light from the foils that is not sent towards the PMT will be transmitted toward to the far end of the metre long detector. In practice, a smaller detector could benefit from reflections much earlier. A further set of simulations were performed, including edge reflections, in order to properly characterise the expected PSD performance in 5 cm cylinders wrapped with thermal neutron converter foils.

For these characterisation tests, 500,000 thermal neutrons were fired in the direction of the detector. 30,363 events recorded a simulated pulse. These events are displayed in Figure 4.24. Of all pulses recorded, 20,446 events recorded are discriminated from ratios as neutrons, using a PSD cut of 0.2. The remaining 9,917 events are marked as gammas from neutrons captured on hydrogen within the scintillator. Based on recorded neutron and gamma triggers, this detector will record one gamma from thermal neutron capture for every 2.06 neutrons detected in the foil. This unavoidable background to detected gammas should be considered in any further analysis using these detectors. As for the true number of each particle interactions, there were 20,422 true neutrons, and 9,941 true gammas. Table 4.2 shows the PSD performance.

Particle Type	**Detected based on PSD**	**True Count**	**Detected/True**
Neutrons	$20,446 \pm 143$	$20,422 \pm 143$	100.12%
Gammas	$9,917 \pm 100$	$9,941 \pm 100$	99.76%

Table 4.2: PSD performance based on correct identification of neutrons and gammas in the detector.

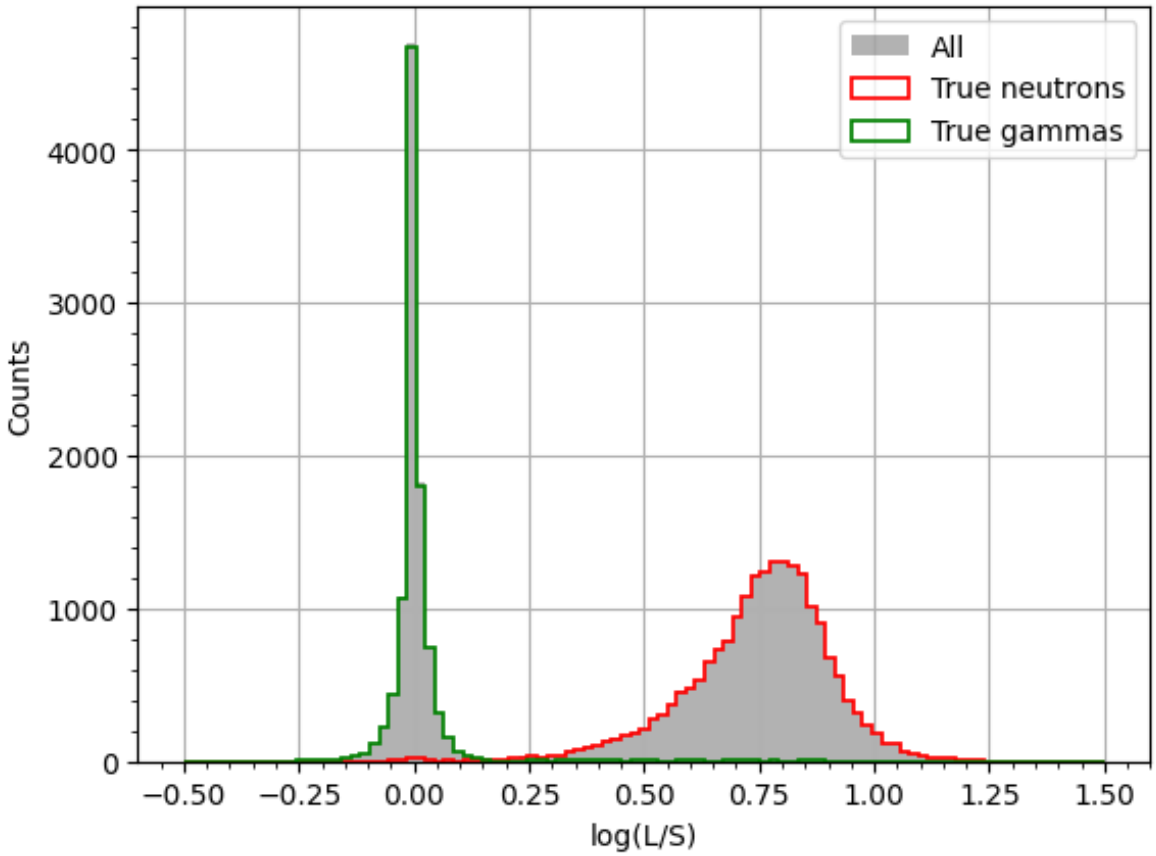

Figure 4.24: PSD histogram for recorded events in 5cm cylinder, after 500,000 simulated thermal neutrons incident on detector. 30,363 triggers occurred.

4.3.3 PSD Prediction Code

A key output of this detector development work was the production of code which works in parallel with GEANT4 and CRESTA to produce realistic waveforms and predictions of PSD figures of merit for novel detectors. The code developed here offers the flexibility to modify the properties of detectors and photosensors by importing optical data for emission profiles and quantum efficiency curves. For any geometry it is therefore possible to explore the potential for novel PSD based optical detectors. In this work, simulations informed on unfeasible detector prototypes using optical fibres, and suggested an ideal detector design capable of good neutron gamma discrimination. This code can be made available upon request for the investigation of novel scintillators for neutron and gamma detection.

4.4 Chapter Summary

Overall, this chapter has explored potential detector configurations for a mixed-field borehole detector, specifically with regards to the geometry of separated modules. The key decisions made were:

- Highly segmented designs using fibre readout are not feasible with the tested configuration of coupled scintillator and foil.
- GEANT4 optical simulations suggest that poor light collection on fibres contributes to the misclassification of particles creating light pulses within the detector.
- Fibre-readout is therefore not ideal for this application on account of contamination of the detected gamma population with misclassified neutrons.
- However, directly coupled PMT-scintillator-foil combinations perform well for mixed-field detection, showing good figure of merit with low misclassification rates.
- The optimal geometry for PMTs of 5cm diameter consists of a 5×5 cm cylinder. At this length, good confidence can be had in the light profile received at the PMT. Beyond this length, pulses degrade significantly.
- Software has been produced capable of working with CRESTA/GEANT4 to produce realistic PMT pulses based on optical data. These pulses can be used to predict PSD capability of novel detectors. In this case the code was used to investigate feasibility of mixed-field detectors made from plastic scintillator coupled to thermal neutron converter foils.

Chapter 5

Custom Manufactured Plastic Scintillators for Fast Prototyping

The plastic scintillator used in the prototype detector produced in this work was manufactured in-house using low-cost casting methods and little specialised equipment.There is no requirement for vacuum ovens or high temperatures, and most materials required can be purchased off-the-shelf. The methods to produce scintillator samples are outlined in this chapter, along with tests performed on samples to characterise their properties. It is hoped that others can find use for the low-cost casting methods in this thesis for prototyping in detector development projects. It is also considered that this prototyping could be coupled with simulation code from chapter 4 to explore potential for novel detectors.

5.1 Additive Manufacturing of Particle Detectors

Due to the variety of geometries proposed in this borehole detector, a technique was required which would allow for fast-prototyping of scintillator designs. Plastic scintillator manufacturing generally requires specialised equipment, and though much cheaper than their inorganic counterparts, the setup can be expensive. As a brief general overview, plastic scintillators are manufactured according to the following methods:

- Injection Moulding - Injection of heated thermoplastic under high pressure into purpose built metal moulds.

- Casting - Similar to injection moulding without the requirement of high pressure. The thermoplastic is simply allowed to settle into the shape of its container.
- Extrusion - Melted plastic is continuously forced through a hole, forming lengths of plastic in the desired cross-sectional shape.
- Less commonly, plastic scintillator has been 3D printed with some success, as in [94].

Approaching an external company to manufacture scintillators of a specified design is the first obvious option in any detector development project. However, the costs associated with a new non-standard geometry are high. In addition, if the design is likely to change for further testing, this price can multiply accordingly due to the required setup in manufacturing. Therefore, as a more flexible alternative, it was decided to explore the manufacture of custom scintillators in-house.

In-house Manufactured Plastic Scintillator

As discussed in chapter 2, a plastic scintillator consists of organic dopant molecules suspended within an aromatic base matrix. The first challenge was finding a suitable base material which balances the desired characteristics of a scintillator:

- Aromatic - Benzene rings are critical to the scintillation mechanism discussed in chapter 2.
- Transparency - Any base material must be sufficiently transparent to any scintillation light emitted. It is important to consider this over the relevant wavelength ranges of fluorophore molecules.
- Low Cost - For the purposes of this work in particlular, the base material, constituting over 90% of the scintillator, must have a low cost per cm^3.
- Simplicity of casting - Many plastics require complex manufacturing in highly controlled environments at high temperatures. These conditions can be difficult to replicate and contribute to additional costs. One of the main priorities here is fast-prototyping capability, and so a simple manufacturing process is vital.

Off-the-shelf, two-part bisphenol-A based epoxy was considered as a suitable base material. Available from £13.22/kg for a 30 kg kit, GlassCast50 epoxy [95] provides

	Price per kg	Amount used per kg of scintillator / g	Cost per kg of scintillator
Base material	£13.22	1000	£13.22
Primary fluorophore	£1286	10	£12.86
Secondary fluorophore	£6120	0.1	£0.61
Solvent	£34.39	303	£10.42
Total Cost			£37.11

Table 5.1: Cost of components for the scintillator manufactured in this work. All costs taken from [97]. This mixture assumes a scintillator doped with fluors at 1% by mass, with a PPO:POPOP ratio of 100:1.

a convenient low-cost material that is simple to work with. Provided as a liquid, it is not necessary to heat the mixture in order to create a pourable plastic, as it is with polystyrene beads for example. In order to assess its suitability for scintillators, testing was performed to investigate its transparency as a function of wavelength. This information was then used to inform upon ideal dopants for use in the scintillator cocktail.

Eljen sell a similar PVT-based product for scintillator casting (EJ-290), available for £616/kg, which casts over a period of 14 days at 47 °C, wth a post-cure at 80 °C. Full casting instructions for this product are available in [96]. To fully compare costs, Table 5.1 shows the costs of all components for the scintillator manufactured in this work. Clearly there is significant cost improvement compared with commercially available EJ-290. In addition, curing is simpler, and can be performed at room temperature. It is hoped that this low-cost method could be of use for others interested in fast prototyping of plastic scintillators.

Using a Shimadzu Spectrophotometer [98], an undoped sample of mixed epoxy was cast inside a cuvette and illuminated with photons of wavelengths ranging from 200 to 800 nm. Transmission was measured and observed to fall sharply around 400 nm. Figure 5.1 shows the transmission spectrum, overlaid with the emission profiles of the fluorophores selected for this work.

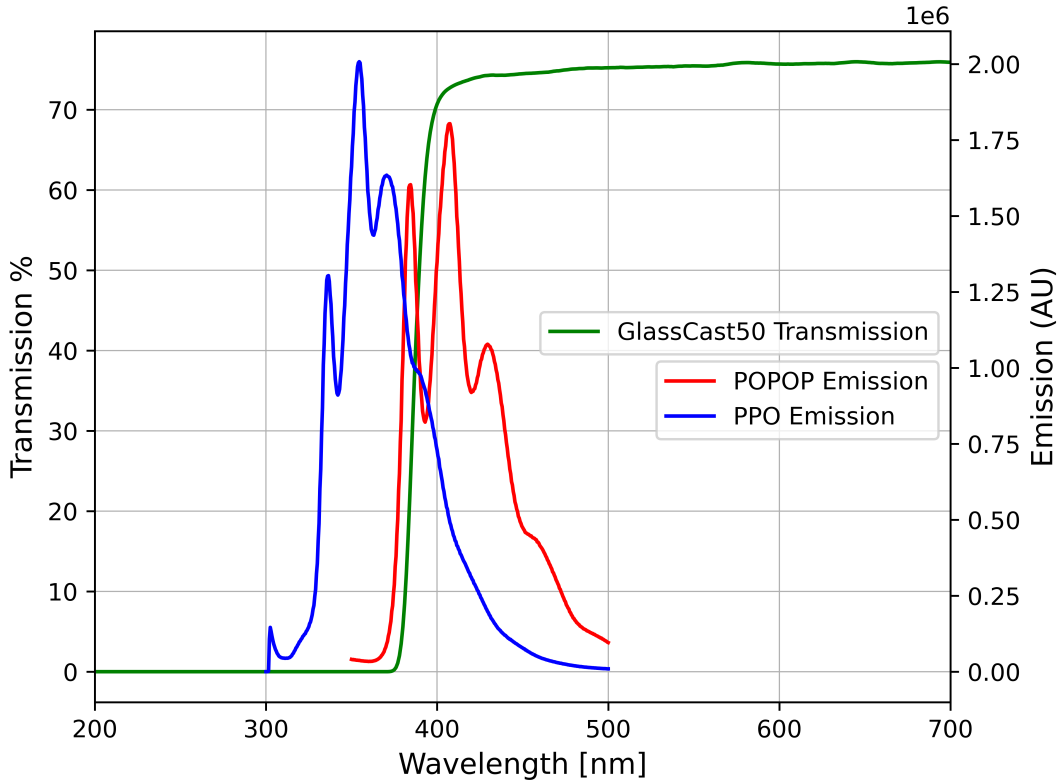

Figure 5.1: Transmission in 1cm cuvette of GlassCast50 base resin, overlaid with the emission profiles of PPO and POPOP

This transmission profile requires that any fluors used to dope this plastic scintillator must have at least some emission above 380 nm. This will ensure that sufficient light can escape the scintillator and be detected by the photosensor. 2,5-diphenyl-oxazole (PPO) is a suitable fluor for this purpose, with a tail extending into this region. However, the performance of plastic scintillators is commonly improved by the addition of a secondary fluor, in this case, 1,4-bis(5-phenyloxazol-2-yl) benzene (POPOP) is used. This can further extend the emission profile of the scintillator into longer wavelength regions. This is important for two reasons:

- It is possible to push the emission profile further into the highly transmissive region of the base material.
- It also pushes the emission profile closer to the wavelength region of highest quantum efficiency for most photosensors (> 400 nm).

The resin used is self-degassing to prevent bubble formation during the cure. This

allows for simple manufacturing of clear, consistent samples, with no vacuum equipment required. Curing occurs at room temperature and pressure with no additional gases, negating the need for additional equipment, and thus lowering manufacturing cost. The epoxy is compatible with solvents used for dissolving fluor molecules, with the final cured product unaffected. It is available at low-cost, off-the-shelf from many different manufacturers as a two-part mixing compound. The combination of all of these factors makes it suitable for fast prototyping of scintillation detectors.

5.1.1 Manufacturing Procedure

Dissolution of Fluors

The fluors selected in this work are PPO and POPOP, on account of their suitable emission profiles and low cost. PPO is the primary fluorophore in this scintillator system, with POPOP a secondary fluorophore or wavelength shifter to enhance transmission. The fluorophores are available from numerous suppliers as a fine powder.

In order for the final scintillator to be suitably transparent, the fluors must be well-dissolved in the base matrix. This is assisted by the addition of a xylene solvent, which will mostly evaporate during the cure. During tests, for a 100:1 PPO:POPOP mixture at room temperature, 0.060 g of fluors could be dissolved per cm^3 of xylene. Of course, this means for more highly doped scintillators, larger amounts of solvent are required. The required mass of fluors is weighed out, and added to a SpeedMixer compatible container. Xylene is then added to dissolve the fluors and the fluor-solvent combination is mixed in the SpeedMixer. Though a SpeedMixer was used in this work, the addition of xylene solvent lowers the viscosity of the mixture such that other mixing methods may also be suitable. The result is a fluorescent solvent mixture which alone could be used as a liquid scintillator. This mixture will be added to the epoxy and mixed again to form a solid plastic scintillator. The xylene solvent will evaporate during curing, reducing the volume of the final sample by this amount. This must be considered in the design of any mould.

Epoxy Base Preparation

The epoxy used is a GlassCast50 two-part resin provided by EasyComposites. Part A of the resin is measured and the fluor-solvent combination added. The resulting mixture

will remain a liquid until the hardener (part B) is added. It is therefore possible to make up a large batch of scintillator ahead of time, ready for use in future moulds. This was again placed in the SpeedMixer to ensure a homogeneous mixture.

Mould Preparation for Custom Geometries

For custom geometries, the scintillator must be cast in a mould of the required shape and later removed for deployment within a detector system. The first samples were cast in custom-made 5cm diameter silicone moulds. These moulds have smooth edges (required for good optical interfaces), and are flexible, which greatly assists removal post-cure. However, one of the main reasons for in-house manufacturing is customisability. Therefore, it is necessary that we are able to create moulds of suitable geometry with convenient and low-cost methods.

To create a mould of the necessary geometry, initial attempts were made using fused-deposition-modelling (FDM) 3D printing. FDM printers use thermoplastic filament to deposit layers onto a print bed, building up the desired shape one layer at a time. In the first instance, a mould was printed directly, in two parts which were held together during the curing process. This was quickly found to be unfeasible, with cured scintillator fusing directly to the printed mould.

Efforts therefore pivoted to silicone rubber casting. Silicone rubber can be cast from a two-part mixture, forming a flexible, reusable mould in the desired shape. This was used to create moulds based on a printed shape. The desired geometry was printed and enveloped in a two-part cure silicone rubber. After mould-curing, the 3D printed target shape can be removed from the mould easily, leaving a void into which scintillator mixture can be poured for curing.

When using an FDM printer, layer lines from the print are present on the generated mould. Therefore, scintillators cast from a mould using FDM negatives would also have layer lines on their surfaces. Options available include:

- Sanding FDM prints to remove layer lines - This is a time-consuming process, which requires working from coarse to fine grit sandpaper in stages. This is also not suitable for fine features in printed models.
- Chemical smoothing of FDM prints - acetone smoothing of ABS prints is a common technique.
- Resin printing - Due to alternative methods of printing, resin prints do not have

layer lines and are much smoother straight off the bed. This is a good option for complex geometries.

- Moulding around an existing metal or glass object - If the desired geometry is relatively simple, an existing part (i.e metal tubing, containers etc) may already exist of an ideal surface quality for creating a mould.

In this instance, a HDPE negative of suitable dimensions was sourced with smooth edges for the desired shape. Desired parts were glued face down to a sheet of material which would form the top of the mould. An enclosure was formed around the edge of the object (see Figure 5.2), allowing sufficient space for a sturdy mould edge, and sufficient coverage of the upturned base of the object. In a separate container, the silicone is mixed with hardener, before being poured into the mould container for casting around the desired scintillator shape Figure 5.3. Curing occurs over 24-48 hours, dependent on temperature.

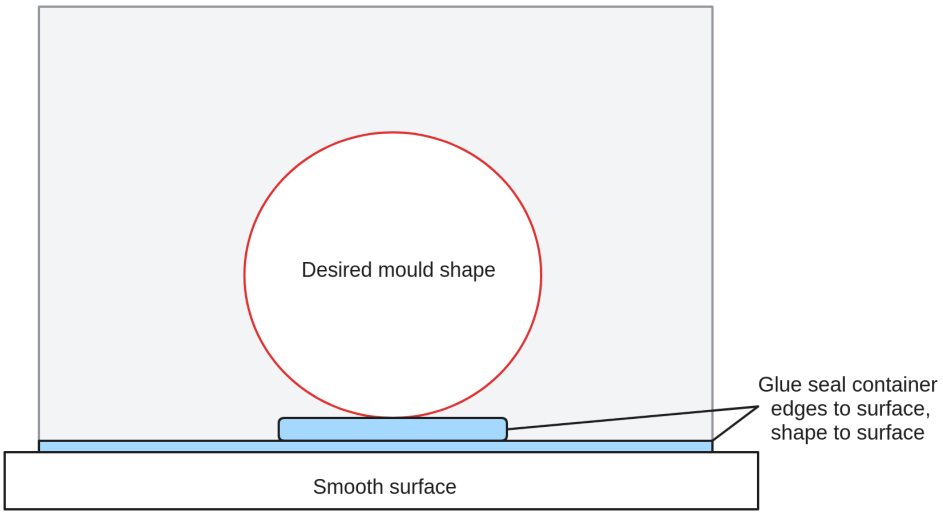

Figure 5.2: First step of creating a mould. A boundary is glued to a smooth surface to hold liquid rubber. The desired shape is then glued face down to the smooth surface.

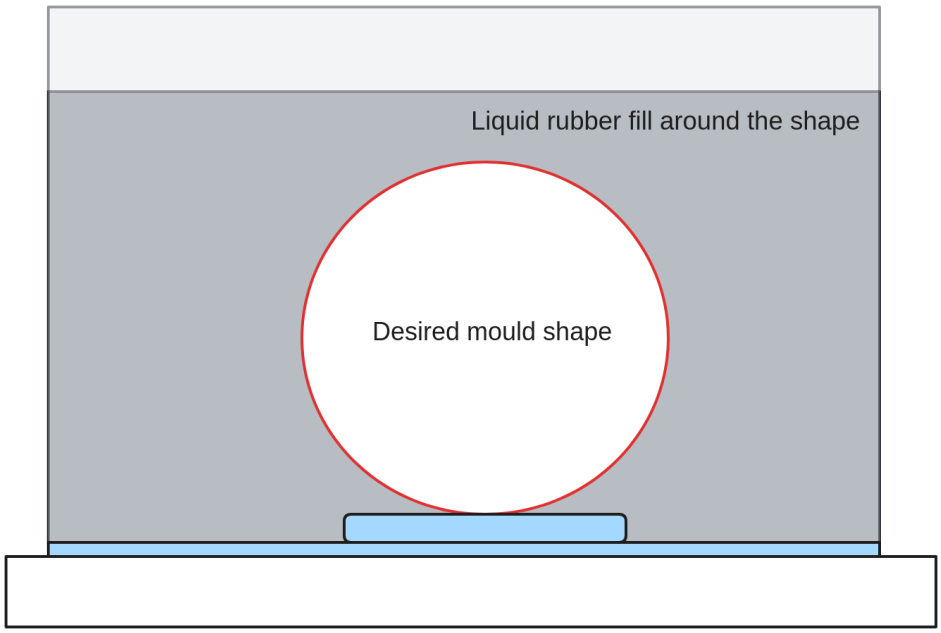

Figure 5.3: Liquid silicone rubber is poured around the mould negative.

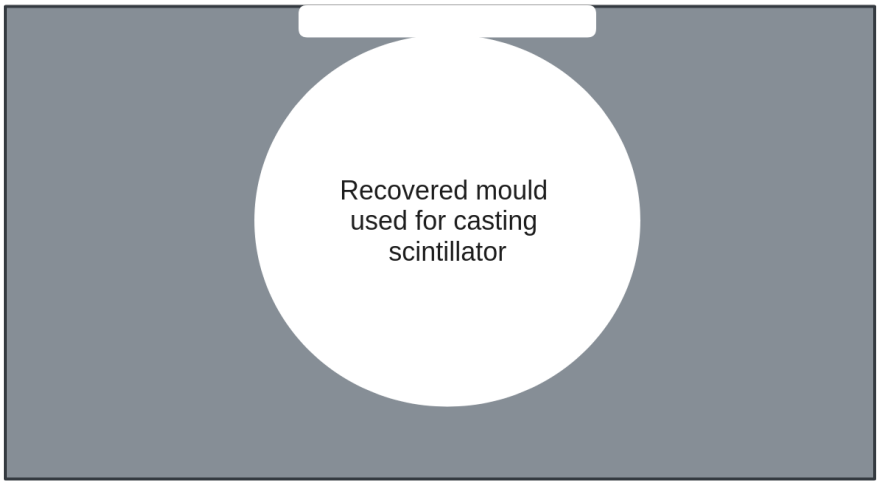

Figure 5.4: Reusable mould recovered for use in scintillator casting. Upturned, flexible mould can then hold scintillator mixture.

Casting

When a suitable mould is prepared, hardener can be added to the part A-fluor mixture to begin the polymerization process. The reaction will proceed at room temperature

with a pot-life of 60 minutes at 20 °C. This mixture is then added to the SpeedMixer for a final time, taking care to mix for no longer than a few minutes to prevent residual heat buildup. Heat will accelerate curing, therefore excessive mixing could result in the scintillator curing within its mixing container. In addition, excessive heat can cause epoxy resins to "exotherm", in which heat can build up within the epoxy, producing harmful vapours. The cured sample in this case can also exhibit yellowing due to excessive oxidation from the excessive heat. Due to the presence of xylene solvent and potential for exotherm, casting should always be performed in a fume cupboard. The specific epoxy used limits pour depth to 5 cm. It is possible that larger scintillators could be achieved by means of repeated pours.

After mixing, the scintillator mixture can be poured into a mould of the desired shape for curing. Care should be taken not to introduce air bubbles at this stage. However, the addition of xylene solvent significantly reduces the viscosity of the mixture, and the resin itself is self-degassing. Samples cured in tests very rarely had any bubbles present post-cure.

Curing time can then vary significantly, and will depend upon the volume and shape of the sample, as well as the volume of xylene added, but in general will take between 48-72 hours. The sample will also continue hardening beyond this time, reaching full hardness after one week. Figure 5.5 shows four examples of cast scintillators with different dopant percentages.

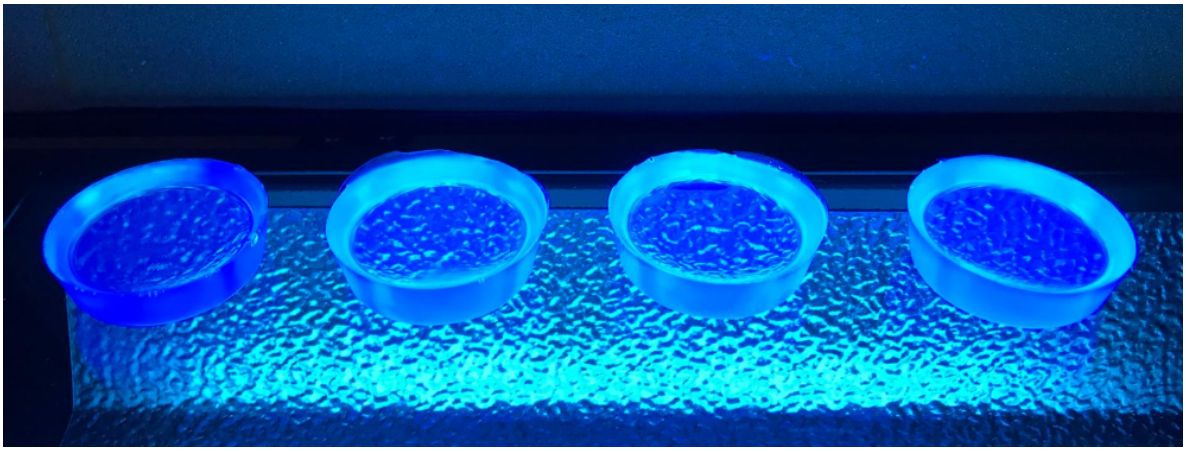

Figure 5.5: Four samples of cast scintillator with increasing dopant percentages (left to right) under UV illumination.

5.1.2 Dopant Variation Tests

For the prototype detector, it was important to consider the ideal composition of the scintillator to optimise its optical properties. Further tests were performed to examine the effects on transparency of different dopant percentages, within the wavelength regions of the chosen flurophore molecules. The non-radiative transfer from the matrix to the primary fluor is reliant on Förster Resonance Energy Transfer (FRET). The efficiency of this transfer is related to the average distance between molecules in the matrix and the fluorophore molecules [99]. Conversely, the addition of further fluorophore molecules can impact the transparency of the medium. It is a balancing act of these effects that determines optimal dopant loading. Typically, plastic scintillators for counting applications are doped at 1% by mass. Other compositions were explored here to examine if any clear trends were present in the response for different doping percentages.

A PPO:POPOP fluor mixture was used in the ratio 100:1 to dope eight samples with different levels of doping to examine how the transmission varies with dopant percentage. 1 cm thick samples were cast inside cuvettes, and transmission was measured using the same Shimadzu spectrophotometer. Figure 5.6 shows the changes in transmission spectrum for different dopant percentages.

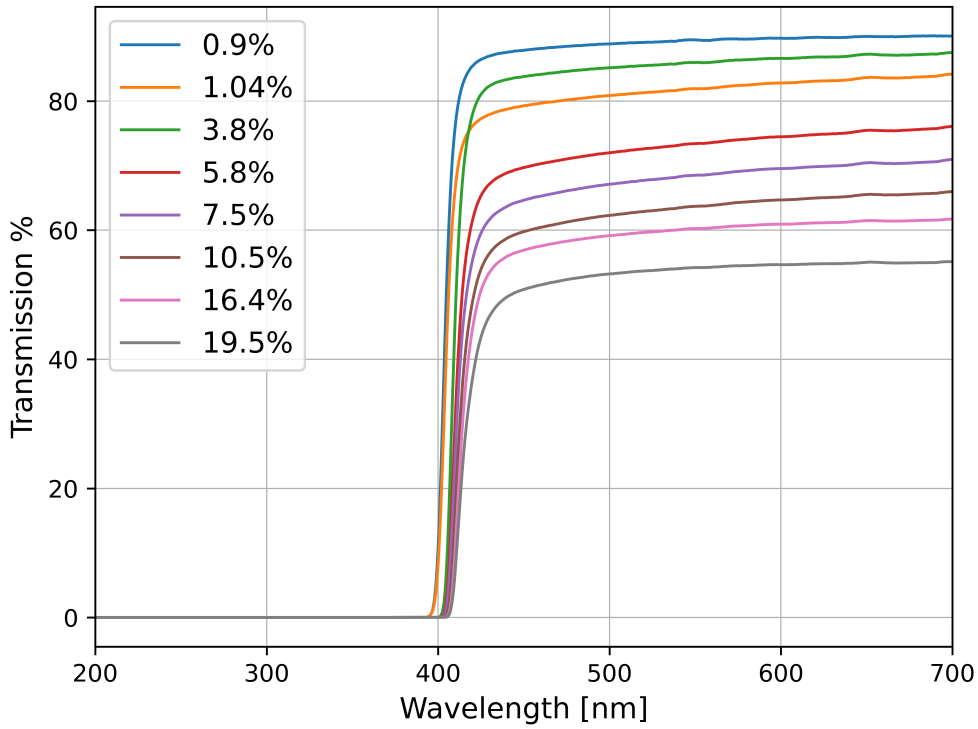

Figure 5.6: Transmission between 200 and 700 nm for different dopant percentages (PPO:POPOP 100:1).

The transmission above 400 nm generally appears to decrease for increasing dopant percentage, with the exception of 3.8% doping, which is thought to be due to an anomalously high quality sample. A closer look at the transmission between 400 and 450 nm in Figure 5.7 reveals the effects on transmission in more detail.

To help inform ideal dopant percentages, the transmission was compared with the emission profile of PPO, as in Figure 5.1. The PPO and POPOP emission parameters were multiplied by the transmission for all wavelengths to produce a weighted transmission spectrum for each sample, which is shown in Figure 5.8 and Figure 5.9.

Figure 5.9 suggests lower dopant percentages are most ideal for maximising emission. Of course, there are complex additional factors at play, which can be difficult to predict. Higher dopant percentage is expected improve the non-radiative transfer by reducing the mean distance between matrix and flurophore molecules. However adding more dopants can affect the optical clarity of samples. Therefore, in addition to spectrophotometry data, samples were tested for their response to

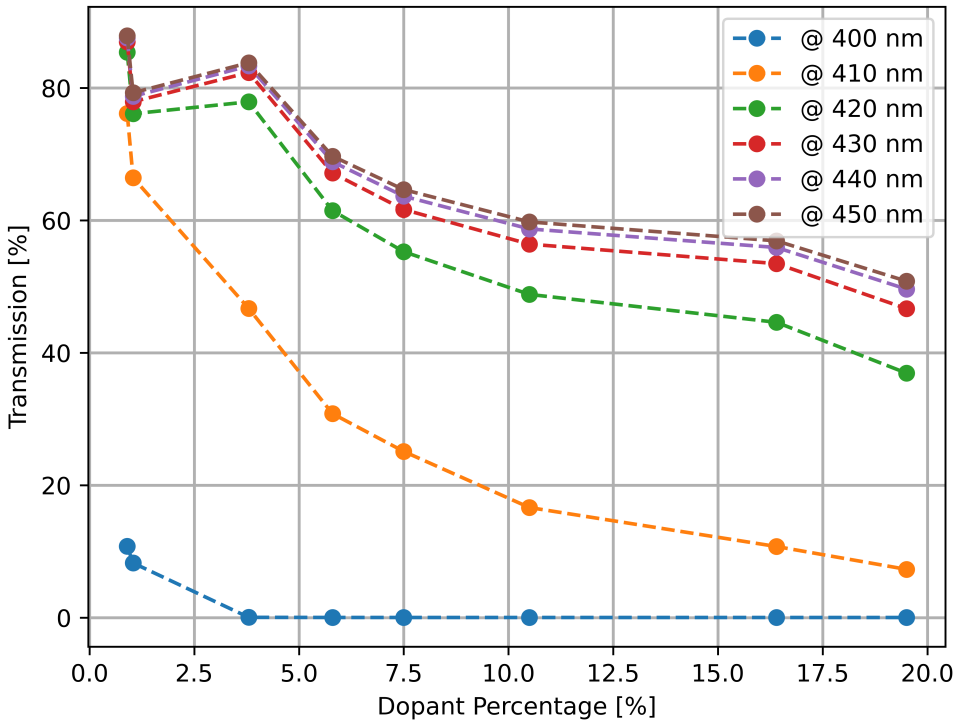

Figure 5.7: Transmission between 400 and 450 nm for different dopant percentages (PPO:POPOP 100:1).

radioactive sources to better compare performance.

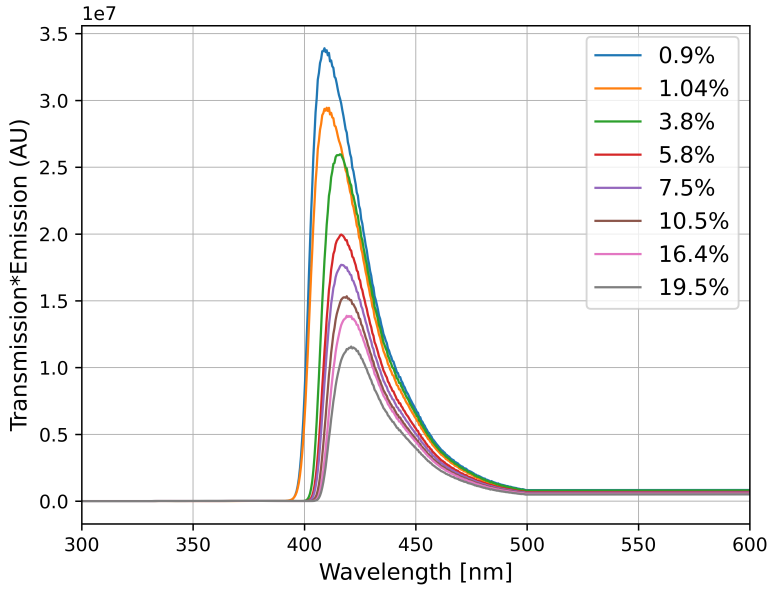

Figure 5.8: PPO emission weighted by transmission between 300 and 600 nm for different dopant percentages (PPO:POPOP 100:1).

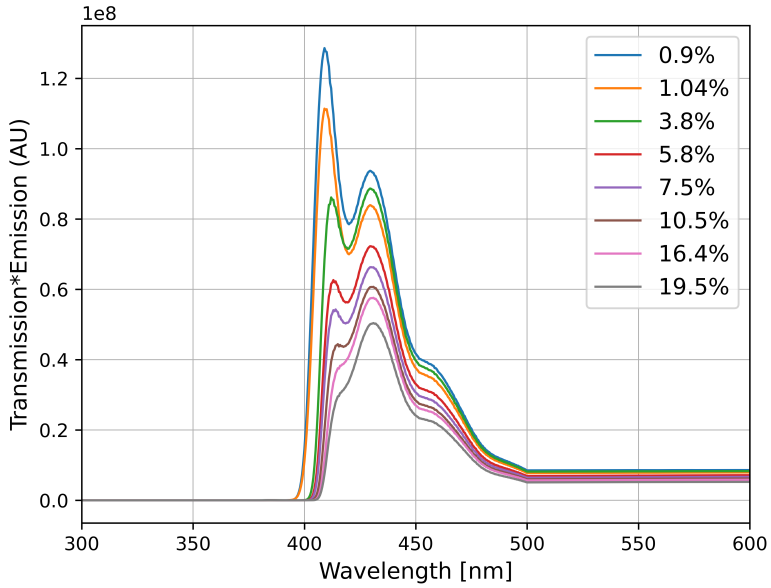

Figure 5.9: POPOP emission weighted by transmission between 300 and 600 nm for different dopant percentages (PPO:POPOP 100:1).

5.1.3 Testing of Plastic Scintillator

The following tests use the same scintillator samples tested in the spectrophotometer measurements in the previous section. All cast scintillators of different dopant concentration were coupled via optical coupling grease to a Hamamatsu R9880 PMT. Scintillator samples were exposed to a Sr-90 source placed directly atop the cuvette as in Figure 5.10.

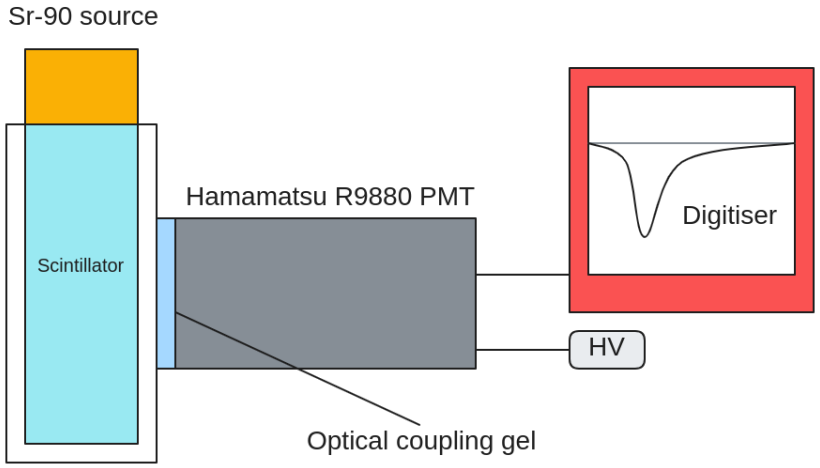

Figure 5.10: Source response testing setup with Sr-90. Full setup pictured is contained in a dark box.

Scintillators were exposed to the source for two minutes, and all recorded waveforms were digitised for offline analysis.

Count Rate Comparison

Figure 5.11 shows the count rate above background for all samples. There is no clear demonstrable increase in performance for increasing dopant percentage. The best performing scintillator was doped at 0.9%. Also of note is the anomalously poor performance at 5.8% doping. There are no obvious reasons for this upon inspection of the sample cuvette, and the scintillator appears transparent with no bubbles present.

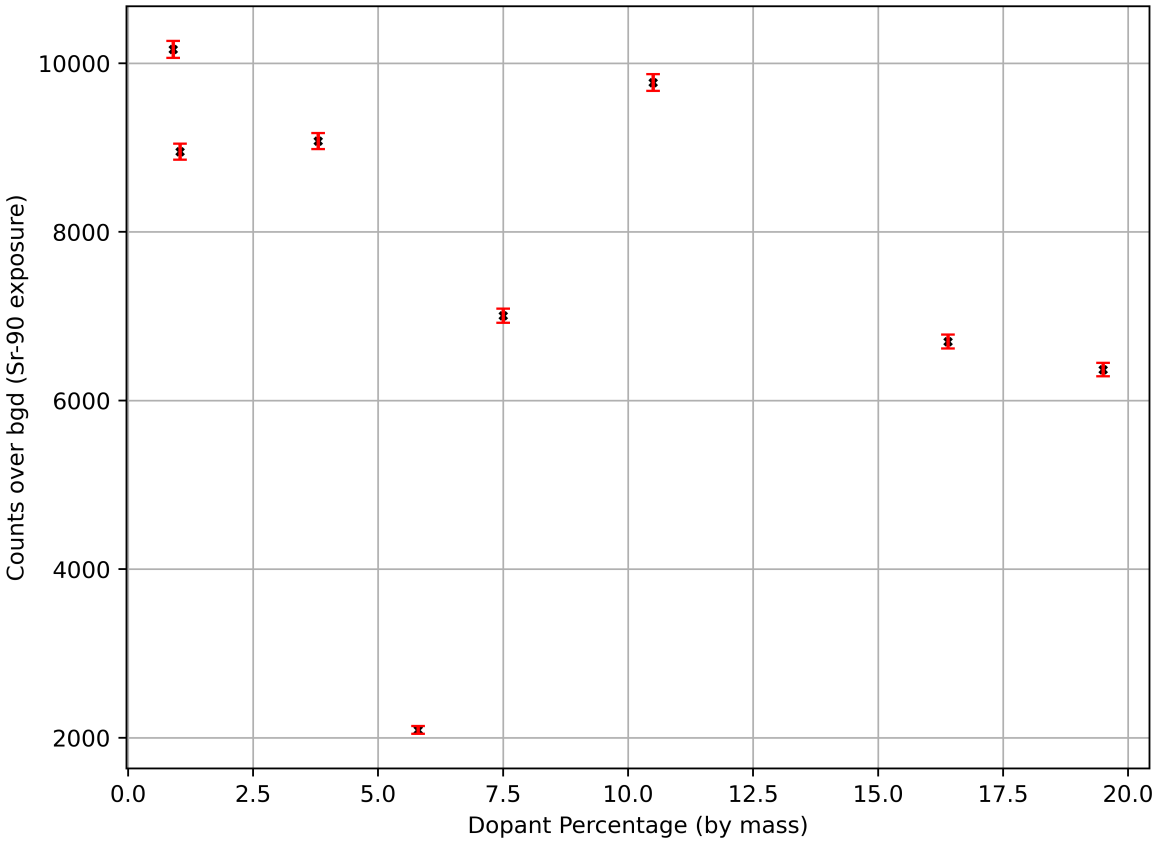

Figure 5.11: Counts above background for the full range of dopant percentages tested.

5.1.4 Dopant Composition for Prototype

Count rate data under source irradiation suggests there is no clear benefit for this application of higher doping with this cast scintillator mixture. In addition to scintillator performance considerations, it is also necessary for this work to consider the ease of manufacture. A higher doping percentage requires a proportional increase in the solvent required to properly dissolve fluors. During casting tests, it was found that 26.3 ml of xylene completely dissolved 1 g of PPO:POPOP fluor mixture. With this increase, the required volume for a mould to cast a scintillator increases, as it must hold the full mixture. As well as count rate data with source irradiation, the optical data was also considered in the selection of ideal compositions. With the eventual goal to couple this scintillator to BN:ZnS converter foils, it is also important to consider transparency in the emission range of ZnS, which peaks around 450 nm. Figure 5.7 shows how at lower dopant percentages, transmission in this range is much higher. On account of these factors, it was chosen for the prototype detector to use a

low doping percentage of 1%, as is used in commonly available polystyrene based plastic scintillators [100]. It was believed that this composition would offer the best combination of both optical characteristics and ease of manufacture.

5.2 Chapter Summary

This chapter outlines the motivations and process behind in-house manufacture of custom geometry scintillators from low-cost, off-the-shelf materials. The processes used in this work could be of benefit to any detector development projects requiring fast prototyping of geometries with flexibility in scintillation properties. Coupled with the work in chapter 4, scintillators could be simulated to understand their light output properties and tested against like-for-like models cast over the course of a few days at low-cost. The key results in this chapter were:

- Plastic scintillator has been manufactured in-house from low-cost materials, with a simple manufacturing procedure. This work was driven by the potential for many different geometries and the requirement for their testing.
- In-house manufactured scintillator has been successfully produced from off-the-shelf, low-cost epoxy, mixed with primary and secondary fluorophores. This mixture can be cured at room temperature requiring no additional vacuum equipment, producing a solid plastic scintillator in virtually any desired geometry.
- The manufacturing procedure is outlined for reproduction in other prototype detector development projects.
- Spectrophotometer data along with Sr-90 source tests have been used to select ideal dopant amounts for this work.
- On account of optical data, source testing, and manufacturing requirements, the choice was made to dope scintillators for this work at 1%.

Chapter 6

Prototype Detector Testing

This chapter will outline construction, characterisation, and testing of the detector prototype with Californium-252 and DT PNG sources to understand potential issues with detectors. It will demonstrate the PSD approaches required when using the DT PNG, and the necessary DAQ for event timestamping. In additon to full detector characterisations, tests were performed with the sand-based testbench from simulations to replicate the borehole environment. Problems were encountered in the practical implementation of the sand-based testbench which ultimately hindered the original test plans for the detector prototype. Despite this, the detector shows good sensitivity to neutron and gamma radiation at low-cost, along with the ability to timestamp events relative to the DT PNG pulse. The detector was tested in the case of a filled and partially-filled test container and observed clear changes in the detector response.

6.1 Single Module Tests and Characterisation

First, four single detector modules were cast from 1% doped plastic scintillator as outlined in the previous section, and wrapped with BN:ZnS(Ag) foils. These detectors were to be coupled to EMI 9954 PMTs, and stacked in a four-detector system. Before testing for PSD, gain calibrations were performed to improve uniformity across detectors. Following this, modules would be constructed into a four-detector prototype.

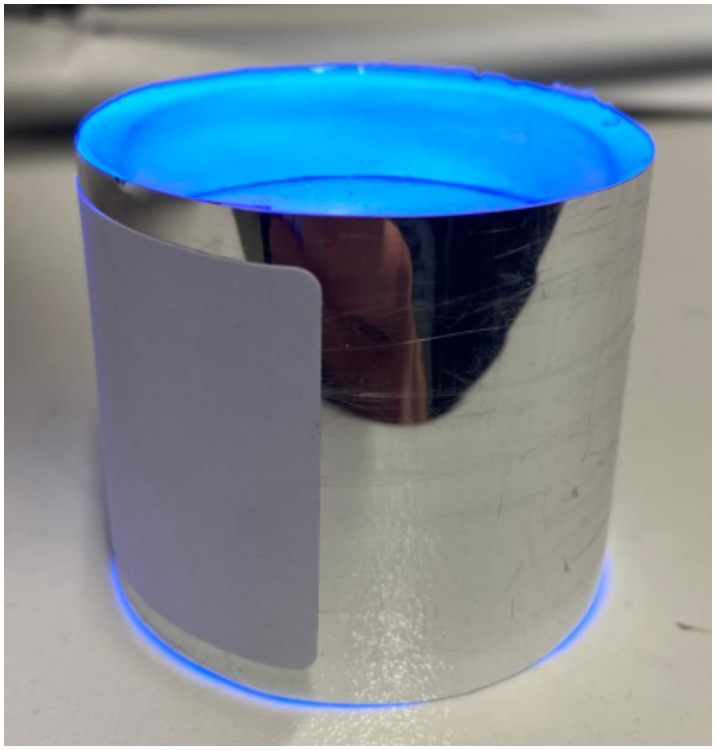

Figure 6.1: Plastic scintillator, cast in-house using methods in chapter 5, wrapped in thermal neutron converter foil. This detector module is ready for coupling to a photosensor. Blue light visible from scintillator due to UV lamp illumination.

6.1.1 PMT Calibration

In order to ensure consistent response across individual detector modules, a PMT gain calibration was performed. Four B20 socket compatible divider bases were available for use with EMI 9954KA PMTs. Each PMT-base pairing was coupled to a 3-inch sodium iodide crystal, which was exposed to a Cs-137 source (along with a Co-60 source of low activity). The resulting pulses were digitised and integrated to produce a spectrum for calibration. The relative position of the Cs-137 photopeak was used to match the gain of all PMTs by adjustment of their operating voltage. PMTs were numbered 1-4 and divider bases labelled A-D.

An initial run was performed scanning between 1700 and 1900 V operating voltage on all PMT-base combinations based on recommended operating voltages from datasheets. The peak from Cs-137 can be clearly observed moving to higher pulse areas as the voltage is increased. Figure 6.2 shows an example for PMT-base combination 1A between 1700 V and 1850 V. Also notice broadening of the peaks at higher gain. This is likely due to increased fluctuations in the secondary electron yield

being of larger magnitude at higher gain. In other words, at higher gain there is a broader selection of possible pulse areas that can arrive at the digitiser for a gamma of a certain energy.

The aim here was to calibrate the detectors to be of comparable gain, and obtain ideal running voltages for each PMT. PMT combination 3-C had noticeably lower gain at similar voltages to the other PMTs, so further runs were taken with this PMT at higher voltages to more closely match other PMT responses. The maximum operating voltage of the 9954 model is 2000V, so 3-C was pushed up to 2000V, and all other PMT voltages were selected to closely match this maximum gain from PMT 3-C. Figure 6.3 shows the photopeak positions for all PMTs as a function of operating voltage. The black dotted line shows the selection of ideal operating voltages. PMT voltages were selected to within 50 V intervals.

The table below shows the selected operating voltages of each PMT combination based on Figure 6.3, with the position of the Cs-137 (integrated charge) peak used for this calibration. With ideal operating conditions set, testing then progressed onto single module tests under Cf-252 irradiation.

PMT-Base	**Optimal voltage / V**	**Cs-137 peak / ADC*samples**
1-A	1800	2.87×10^5
2-B	1850	2.94×10^5
3-C	2000 (max)	2.91×10^5
4-D	1800	2.82×10^5

Table 6.1: Optimal operating voltages for each PMT in the detector for calibrated gain responses.

6.1.2 Relative Efficiency Measurements

To measure the relative efficiency of cast scintillator blocks coupled to foils, a series of tests were performed under Cf-252 irradiation. Scintillator-foil combinations were coupled to photomultipliers and exposed to a Cf-252 source in a thermal shielding container at a fixed distance. Pulses were digitised using the CAEN DT5725 and analysed offline using the long-short integration methods discussed previously, and PSD plots produced.

The PSD plots below show 10 minute exposures of the four detectors under background and Cf-252 irradiation. Short integrals are plotted against the logarithm

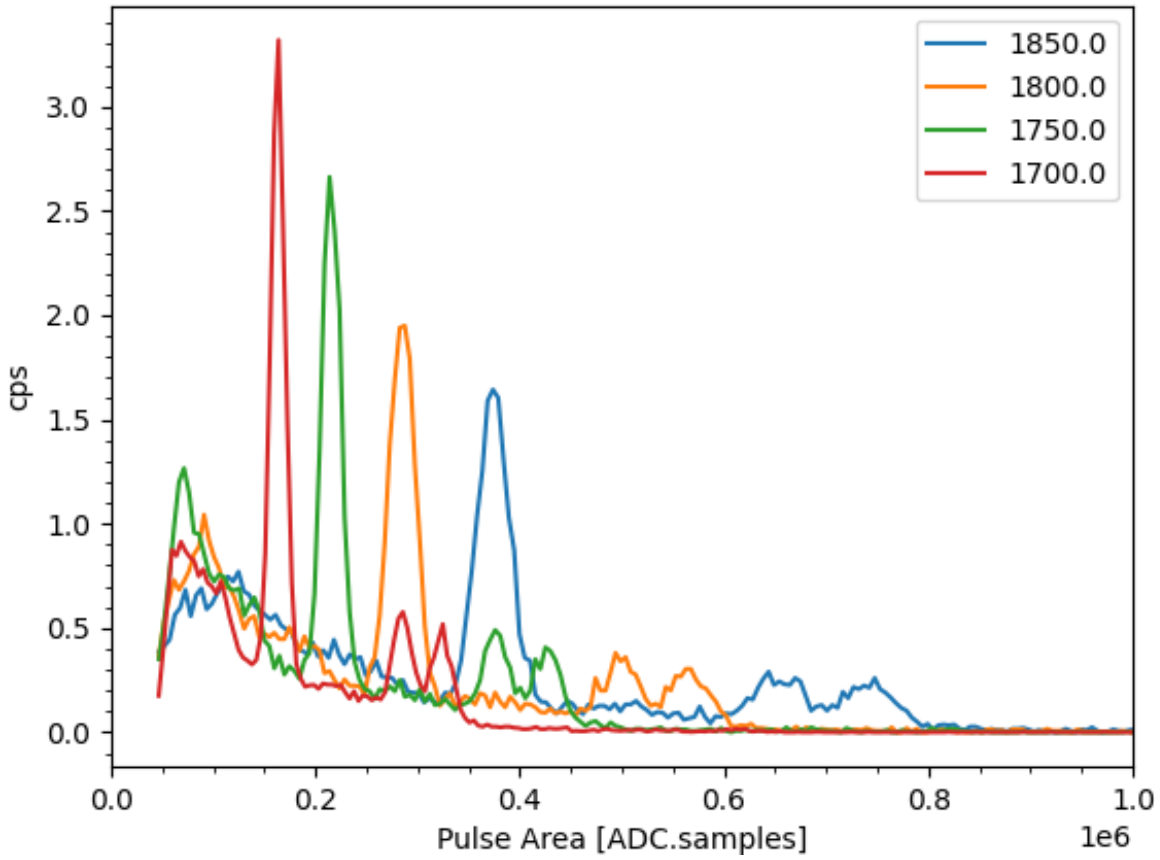

Figure 6.2: Spectrum from sodium iodide crystal coupled to PMT for different operating voltages. The peak positions will be matched for the four-detector system. Large peak visible is Cs-137, with smaller peaks from low-activity Co-60 source.

of long-short ratios.

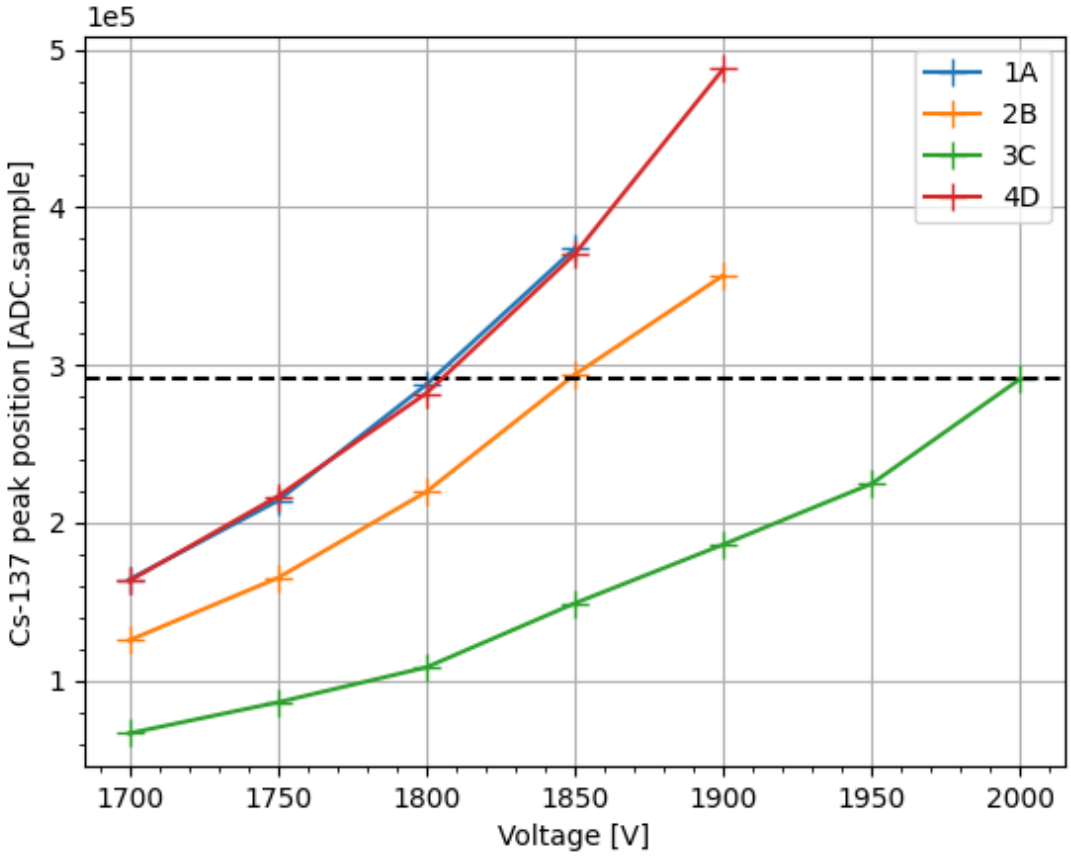

Figure 6.3: Cs-137 photopeak position vs operating voltage for all PMTs to be used in four-detector system.

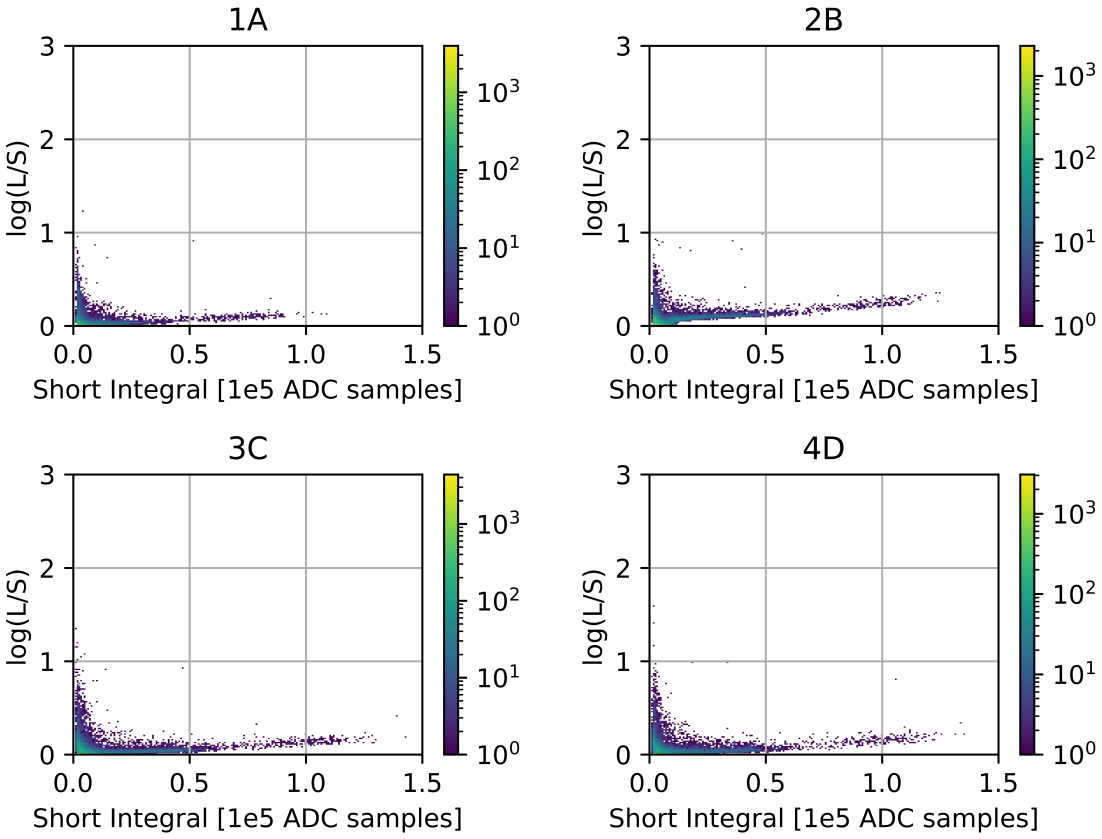

Figure 6.4: PSD plot comparison (background).

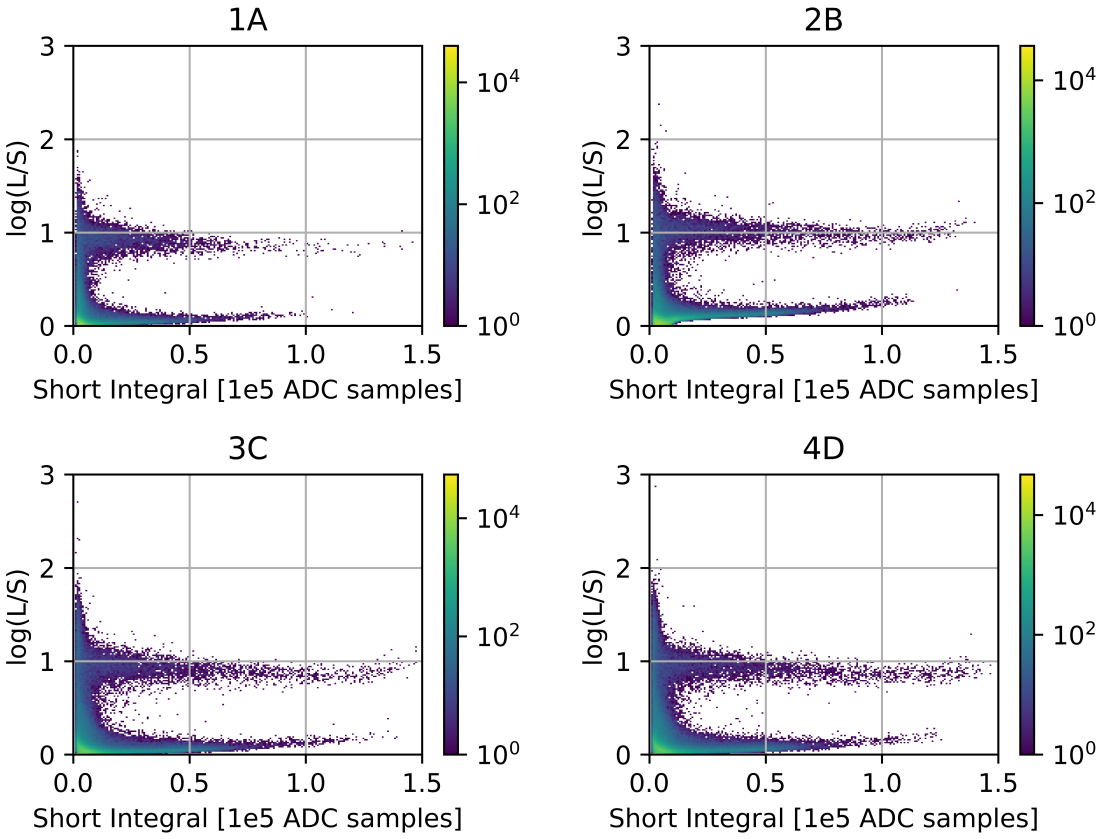

Figure 6.5: PSD plot comparison under Cf-252 irradiation for all four detectors to be used in the combined tool.

Two bands are clearly visible in the case of Cf-252 irradiation, in which the upper band corresponds to thermal neutron events with a higher long-short ratio. Due to overlap in the region containing smaller short integrals, a cut was applied on the short integral axis for all detectors to ensure proper separation of the neutron and gamma populations. This should separate the bands completely, removing overlap, though care must be taken not to cut out more events than necessary. To investigate optimal short integral cut values, a figure of merit was calculated for individual detectors after applying short integral cuts. The figure of merit was calculated as:

$$FoM = \frac{PSD_n - PSD_\gamma}{FWHM_n + FWHM_\gamma} \tag{6.1}$$

Gaussian fits were performed to the neutron and gamma populations in a long-short ratio plot (example in Figure 6.6) with different cut values on the short integral. This was performed for all four detectors. If fitting failed, the figure of merit was scored as 0. Despite good separation of the bands, double Gaussian fitting fails until the low short integral noise is removed. As the short integral cut increases, this also has the effect of reducing overlap between the neutron and gamma distributions. Figure 6.6 shows the gradual improvement for increasing cut values. Also notice that in the leftmost peak, increasing cuts slowly reveal a Gaussian once very low amplitude (or low short integral) noise is removed. This explains the sharp rise in figure-of-merit above an acceptable short-integral threshold.

The following plots show the improvement in figure of merit with increasing cut, along with the reduction in neutron count rate for these cuts. Observe the sharp increase for certain cuts in each detector, this is the lowest short integral cut at which it is possible to then go on to discriminate the two populations. Cutting at integrals lower than this leaves too much noise in signals, preventing proper discrimination, as shown in Figure 6.6. Then, the figure of merit starts to increase as more of the smaller pulses are removed.

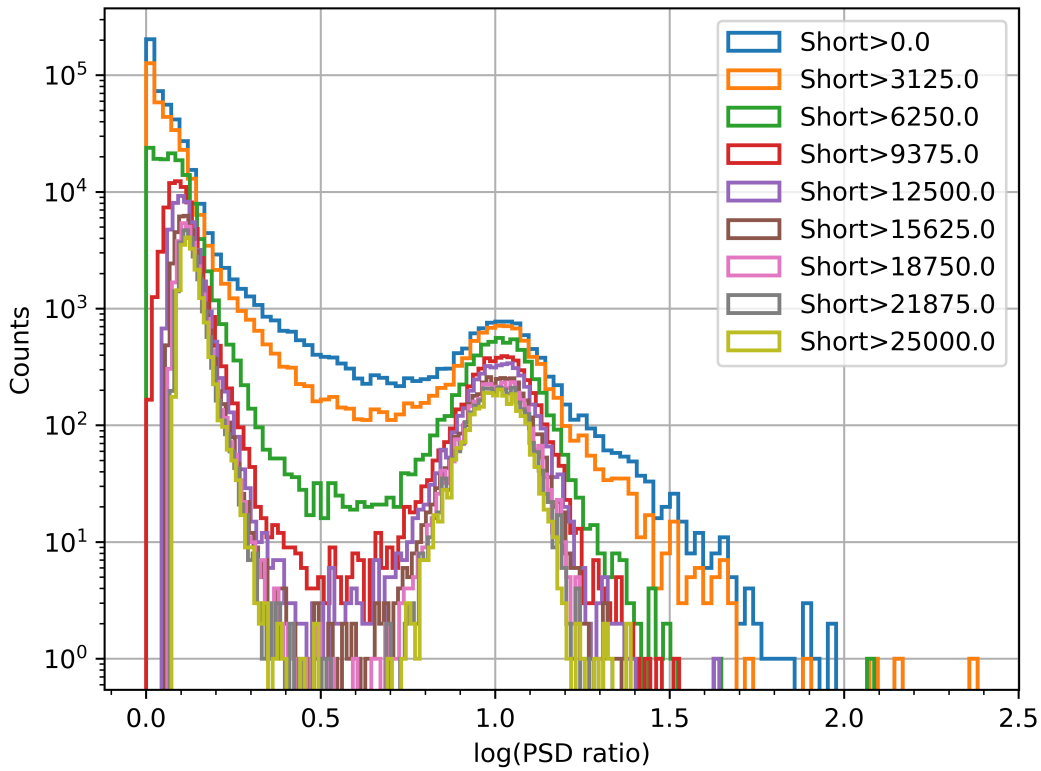

Figure 6.6: Short integral thresholds gradually improve first peak by removing low pulse height noise, allowing fit and figure-of-merit calculation. Plot shows example PSD spectrum from detector 2B.

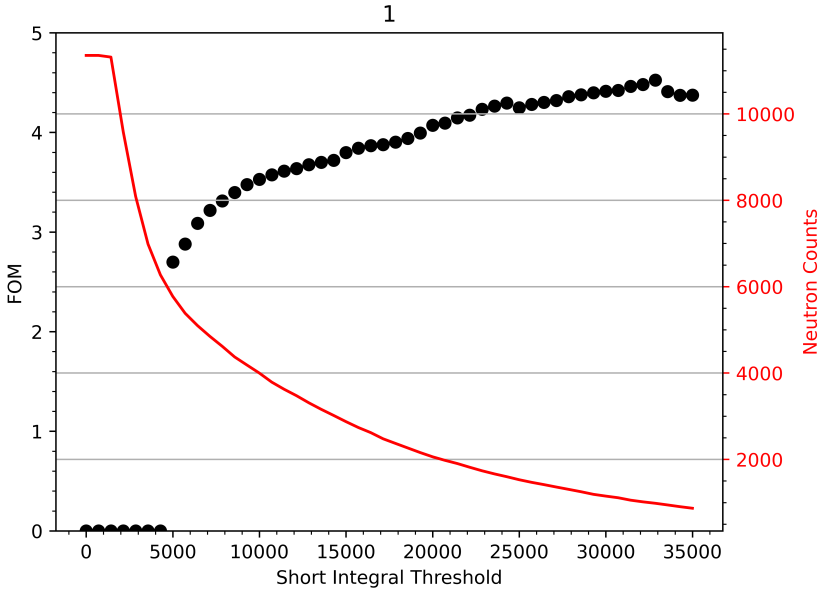

Figure 6.7: Detector 1A - PSD figure-of-merit (black) and neutron counts (red) as a function of short integral threshold. There is a general improvement in the figure-of-merit with increasing threshold at the expense of neutron counts.

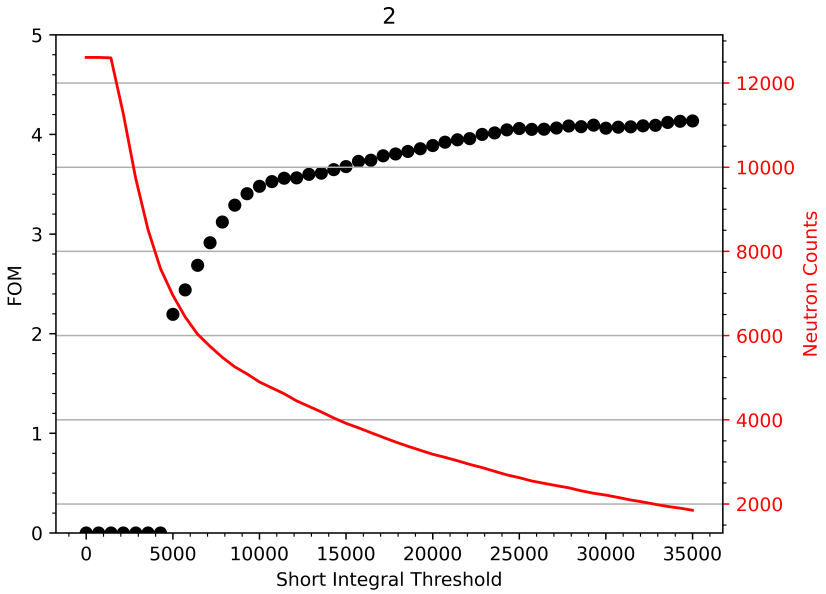

Figure 6.8: Detector 2B

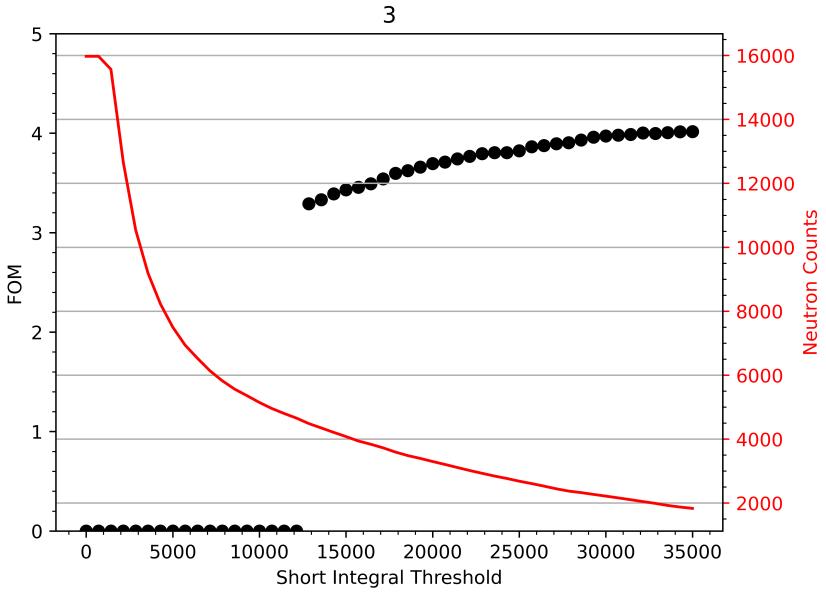

Figure 6.9: Detector 3C.

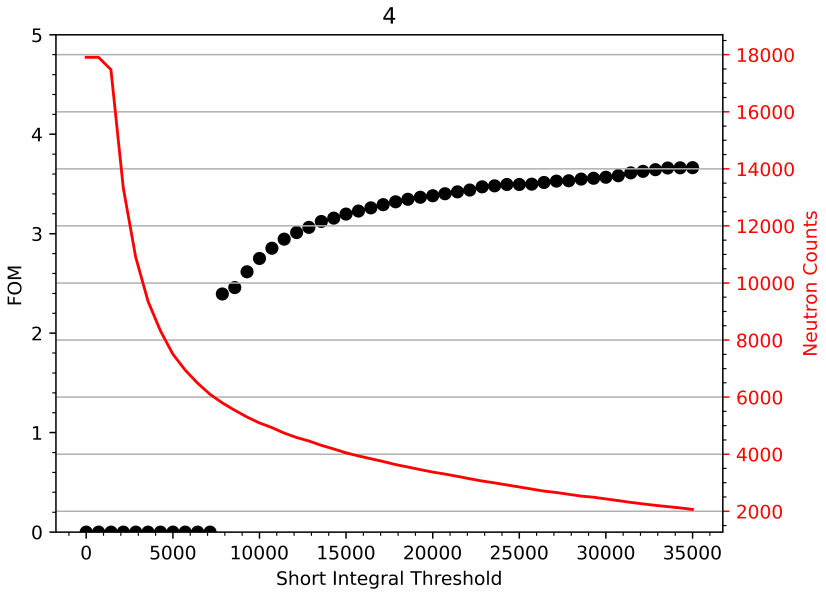

Figure 6.10: Detector 4D

Short integral cuts were selected for each detector and applied to the PSD plots. Cuts were selected such that successful fitting was performed showing good figure of merit, with some additional allowance. Though there was no specific condition required to be met in short cut selection, the resulting neutron and gamma counts would then be used to normalise relative detector efficiencies. This gave detector-specific correction factors to be used for the selected cut to correct the overall detector response in the combined four-detector system. The relative efficiencies for the selected cuts are shown in Table 6.1.2.

Detector	**Short Int. Cut**	**Neutrons**	**% max**	**Gammas**	**% max**
1A	8,000	$4,622 \pm 68$	$94.0 \pm 1.4\%$	$32,121 \pm 180$	$56.5 \pm 0.3\%$
2B	10,000	$4,918 \pm 71$	$100 \pm 1.4\%$	$56,871 \pm 239$	$100 \pm 0.4\%$
3C	15,000	$4,054 \pm 64$	$82.4 \pm 1.3\%$	$42,670 \pm 207$	$75.0 \pm 0.4\%$
4D	12,000	$4,598 \pm 68$	$93.5 \pm 1.4\%$	$49,463 \pm 223$	$87.0 \pm 0.4\%$

Table 6.2: Short integral cut values selected for each detector, along with associated neutron and gamma count rates.

6.2 Four-Detector Prototype

Following initial characterisations, the four detector system was assembled and placed inside an aluminium housing, with 3D printed supports to centralise detectors within the container (see Figure 6.11). A custom endcap was printed for separated high voltage power provision, and four BNC signal cables for reading out pulses from detectors. These signals were routed to a CAEN DT5725 digitiser for offline processing. The final detector, without housing, measures 113 cm in length. Within the aluminium housing the total detector length is 120 and diameter 10 cm (see Figure 6.12).

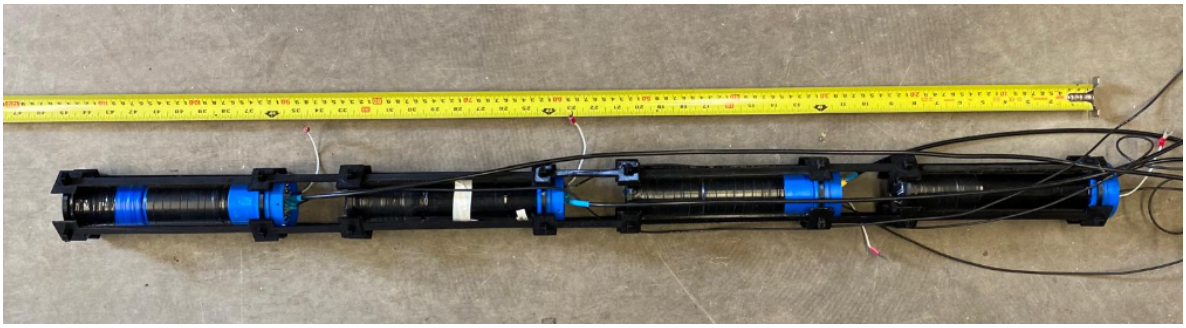

Figure 6.11: Four-detector system. Each detector held in position with lightweight 3-D printed clips ready for housing in aluminium tube.

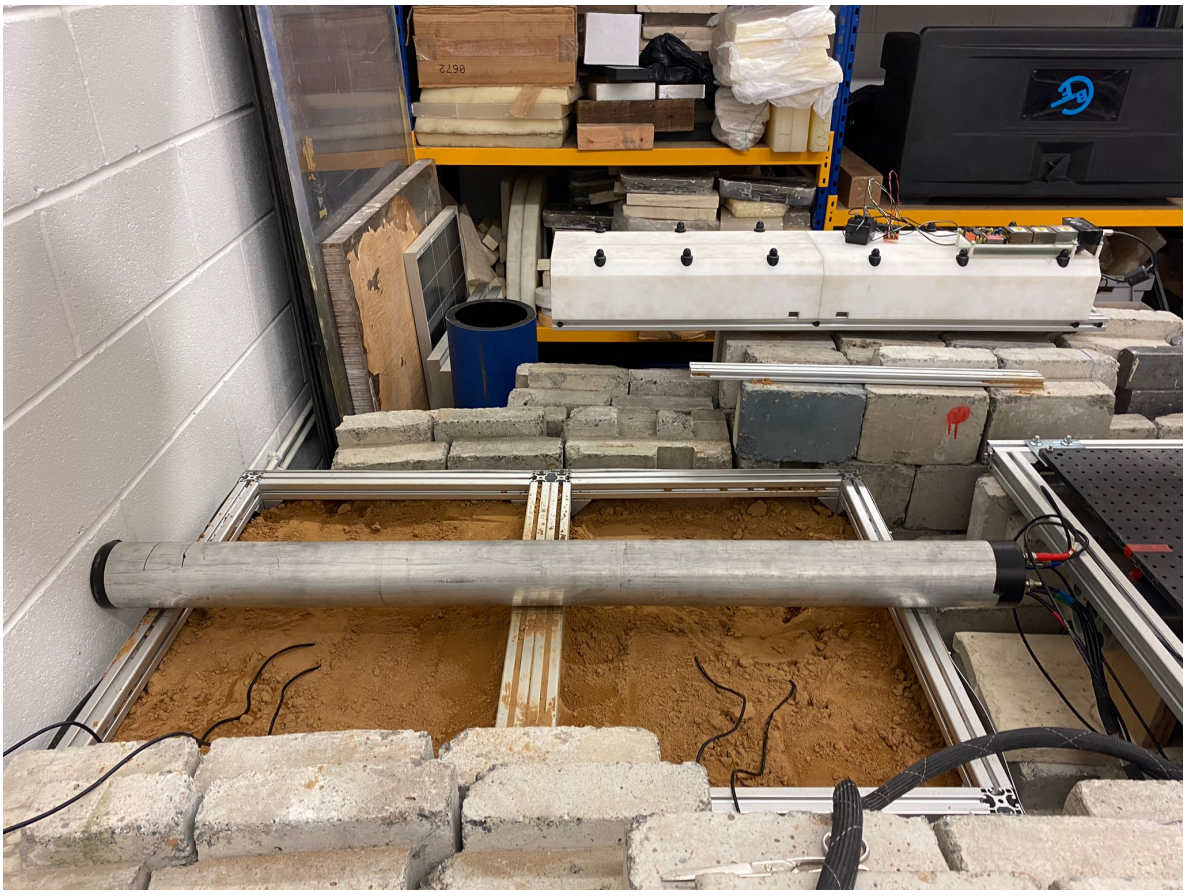

Figure 6.12: Detector in aluminium tube housing.

6.2.1 Data Acquisition

Signals were routed from the generator room up to the control room and into a CAEN DT5725 Digitizer. CAEN's Wavedump software provides event timestamps in event headers as a 31 bit integer plus an additional overflow bit. With the DT5725's trigger clock running at 8ns, this corresponds to a total available "time from zero" of 17.18 seconds of runtime. It is therefore necessary for long pulsed runs to reset the trigger time stamp on the event of a neutron pulse from the D-T PNG's pulser unit. The DT5725 accepts both NIM and TTL format pulses as trigger time tag resets to the GPI input of the digitizer. This was achieved by inputting the PNG pulse into a CAEN discriminator with TTL output.

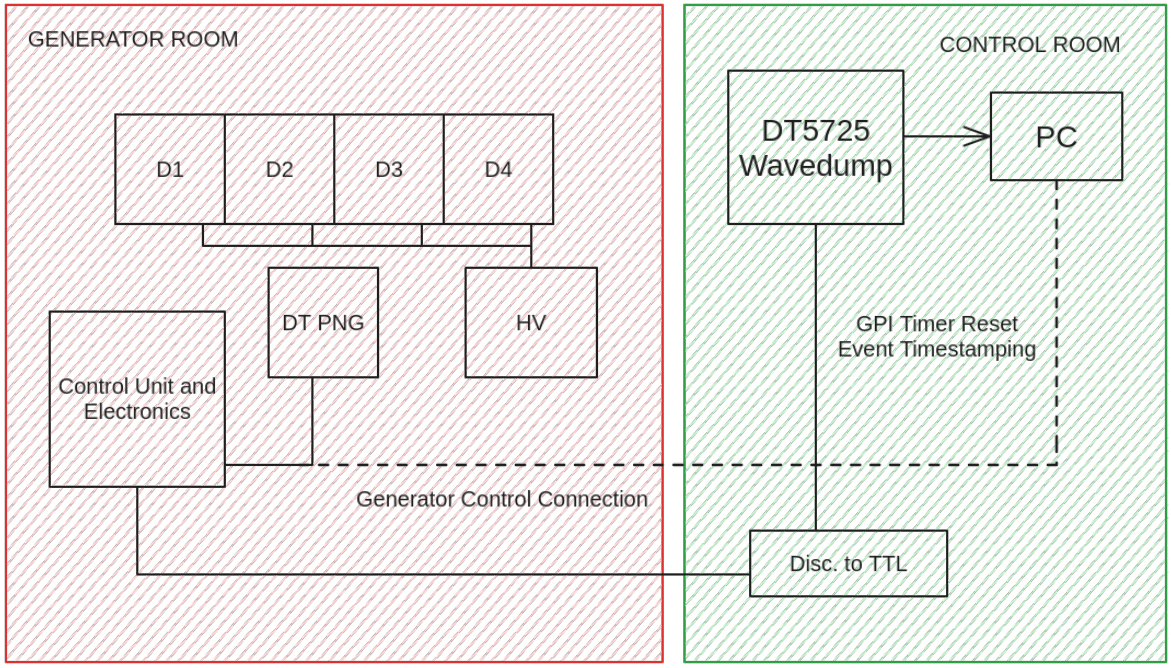

Figure 6.13: Block diagram of the DT neutron facility setup.

Each record from the digitizer then has a timestamp relative to the leading edge of the neutron pulse from the PNG. Timestamped pulses were then subject to PSD analysis (long-short method), and assigned as neutrons or gammas with an associated detector and timestamp.

6.2.2 Early Tests with D-T PNG

Preliminary data taking commenced to investigate the detector response to the DT PNG. In contrast to testing with a simpler radioisotope source, there are more considerations to be made in testing with the DT PNG. In the first instance, it was important to become familiar with the DT PNG operating procedures, and to reliably propagate the generator neutron pulse for time relative measurements. Second, pulsed emission was found to cause significant pileup shortly after a neutron pulse, and so experiments were performed to understand this behaviour to remove the pileup.

NSD Gradel Fusion Neutron Generator

The DT PNG within the Sheffield Neutron Facility is an inertial electrostatic confinement (IEC) based fusion generator. The concept is based on a low pressure DT gas in the reaction chamber, to which a high voltage of up to 120 kV is applied. This voltage is applied between an outer anode and a central hollow cathode, designed in such a way as to allow ions to travel through the cathode grid [101]. Throughout this motion, collisions will occur between Deuterium and Tritium nuclei, generating neutrons via the reaction:

$$^{2}\mathrm{H} + {}^{3}\mathrm{H} \rightarrow {}^{5}\mathrm{H}^{*} \rightarrow {}^{4}\mathrm{He} + n + Q \tag{6.2}$$

The Q-value of this reaction is 17.6 MeV of which 14.1 MeV is carried away by the neutron. Figure 6.14 shows the energy dependent cross-section of the DT reaction, showing that the threshold for reaction is 4 keV peaking around 60 keV. The relatively high cross-section of the DT reaction makes it an ideal candidate for fusion based neutron sources. Figure 6.14 also highlights how it can be expected that there is some contribution to the neutron flux from DT generators from the DD fusion reaction. The NSD Gradel Fusion Generator in the Neutron Facility produces $\approx 0.3\%$ DD neutrons.

The generator is controlled remotely from the generator control room, and first the getter (a material containing the DT gas mixture) must be heated to release the DT gas mixture at sufficient pressure. After heating and additional stabilisation time, the generator can be pulsed at high voltage. This accelerates Deuterium and Tritium ions in the chamber, with the goal of causing the reaction in Equation 6.2.2 to occur. This produces a pulse of neutrons, with a minimum pulse width of 6.5 µs.

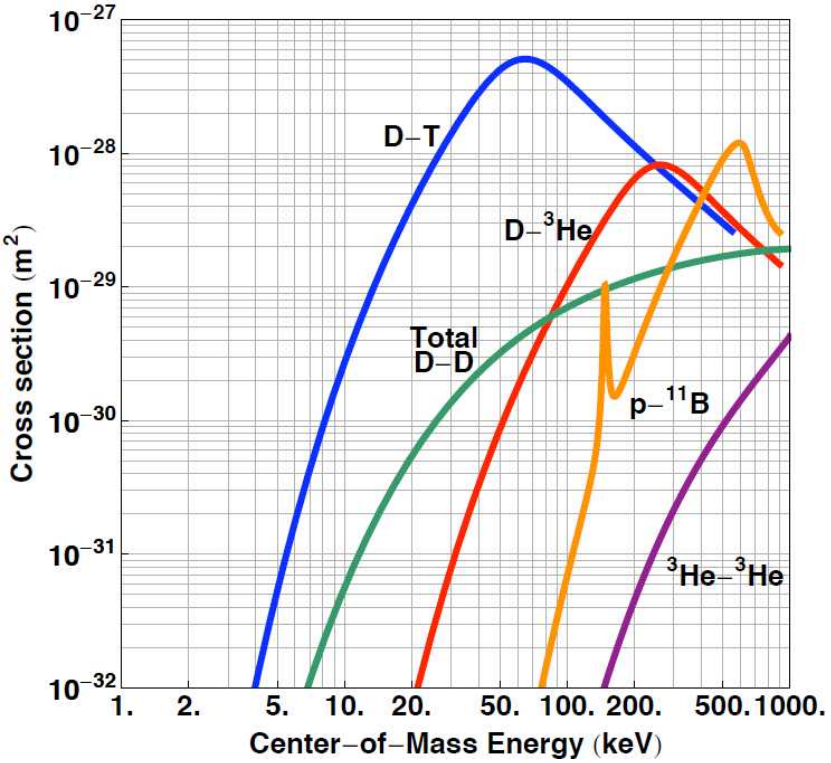

Figure 6.14: Fusion cross-section for a variety of common reactions. DT (blue) shows the highest cross-section over the largest energy range. Image from [102]

6.2.3 Pileup Corrections

With preliminary data taking, significant pulse pile-up of neutron events was observed at short times after the initial neutron pulse (on the order of a few 10s of µs). The PNG operates emitting 2×10^6 neutrons/s. In a typical radioistope source, neutrons are emitted at a constant rate. In the case of the PNG, these neutrons are emitted in short 6.5 µs bursts, with interspersed periods of no emission. Therefore, it follows that one should expect the pileup that would be encountered with a significantly more active radioistope source shortly after these pulses. Figure 6.16 shows an example pulse resulting from pile-up. The timing of these events is much too soon after the neutron pulse to be from thermalised neutrons. It is believed that this pulse is not a convolution of capture events in the foils, but rather a convolution of fast neutron pulses from simultaneous proton recoil events in the foils. Fast DT neutrons can undergo elastic collisions with hydrogen in the foil binder, which go on to cause scintillation in the surrounding ZnS scintillator. For many, almost simultaneous, fast neutron collisions, this could lead to a pileup pulse at short times after the neutron pulse. The decay of

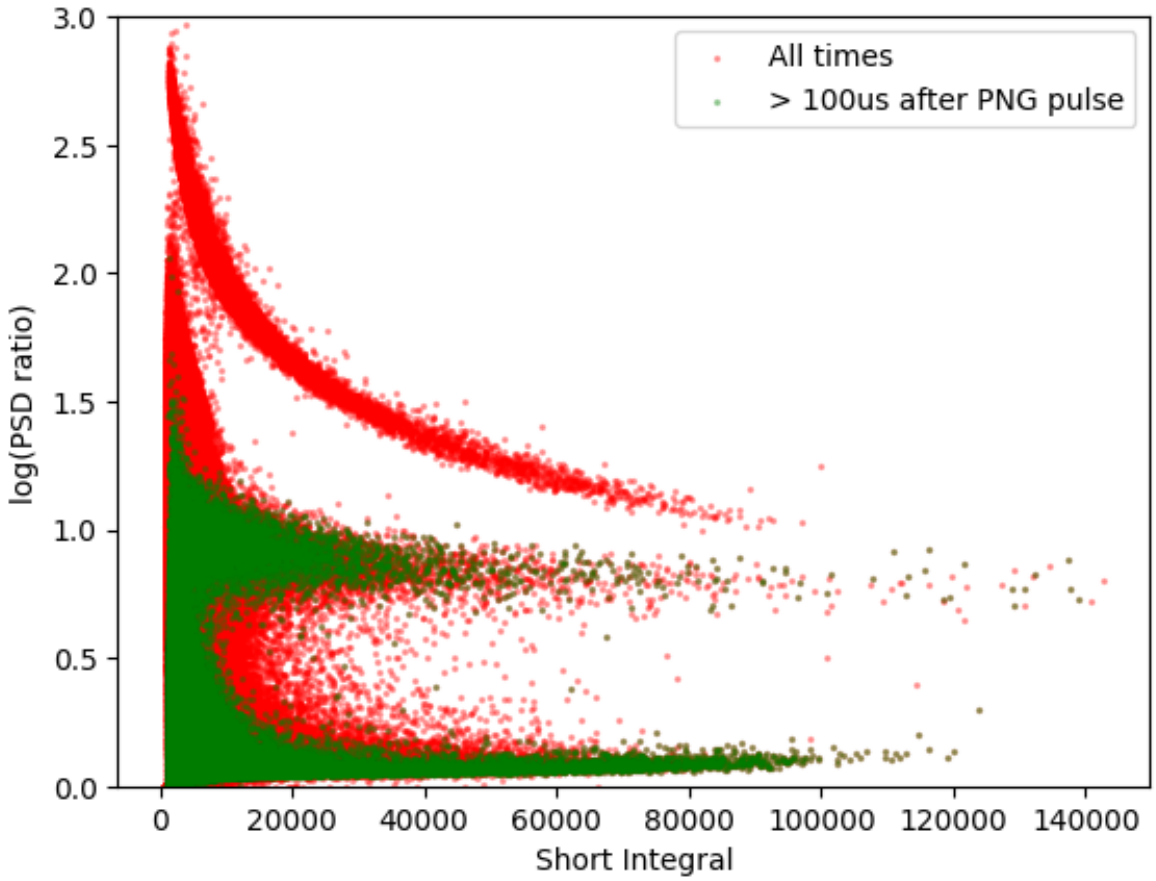

Figure 6.15: Pileup mitigation using time holdoff following DT PNG neutron pulse

this pulse extends over several records. Figure 6.17 shows what would be expected of a typical single neutron capture pulse to compare against the pile up pulses observed at a short time after neutron emission from the generator.

To solve this issue a constraint was applied on the minimum allowed elapsed time before counting hits after the neutron pulse. A holdoff time of 100 µs was introduced before events were accepted. Without this constraint, PSD would be significantly hindered by the presence of these pileup pulses. In addition to this time cut, checks were performed on early samples in event records to ensure that no previous pulses encroached on new triggers.

One other potential cause for concern was noise from the generator pulser, as ripple was observed in early samples from pileup pulses. As a time cut was deemed necessary to avoid pileup issues, pulser noise was cut out of any data used for PSD and therefore was not an issue for these experiments. For any data taken shortly after the generator

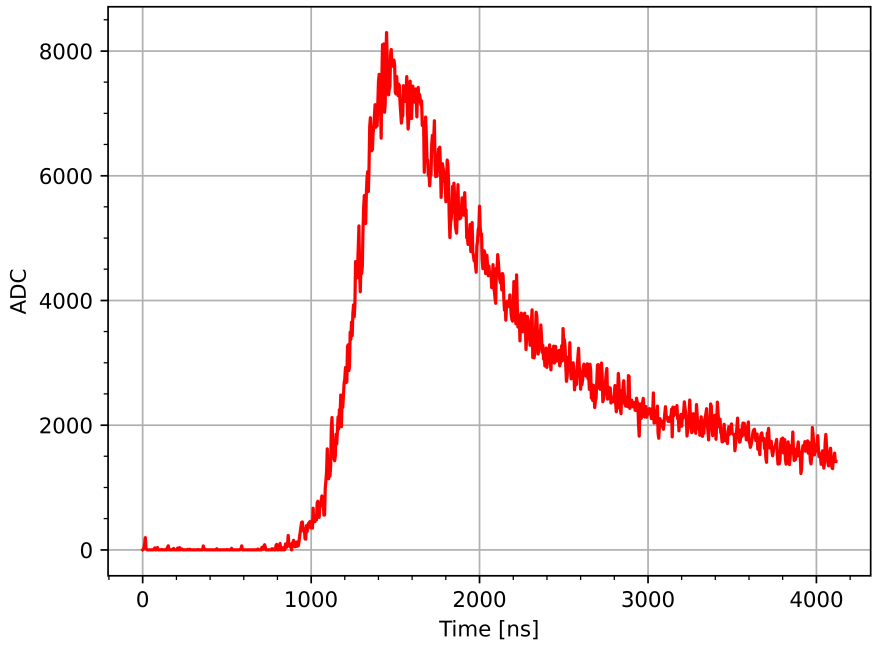

Figure 6.16: A pile up pulse detected 6 µs following the leading edge of the neutron pulse

pulse, in prompt-gamma ray analysis for example, this could be a potential issue.

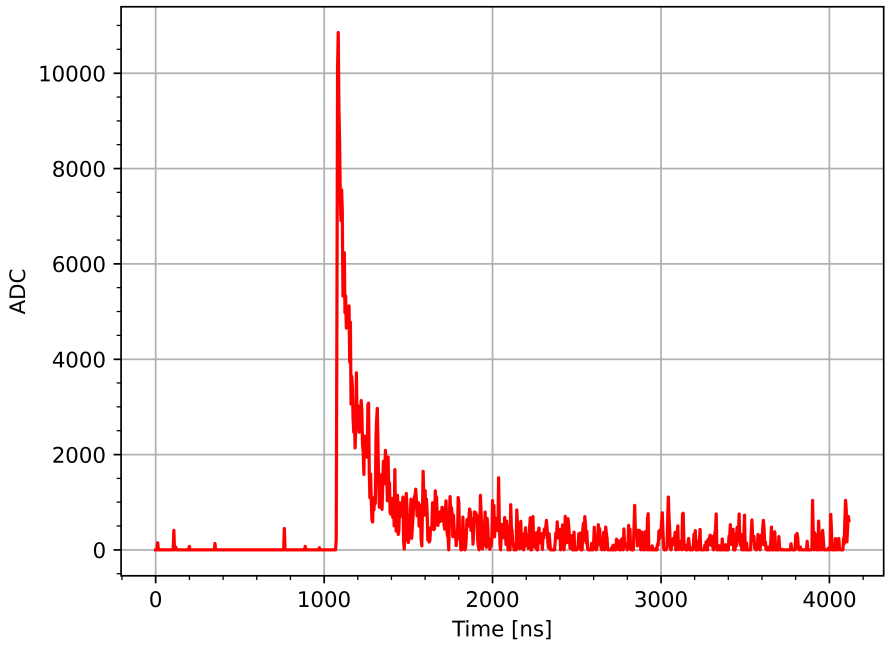

Figure 6.17: A single neutron capture pulse

6.3 Sand-based Test Setup

In order to test the response of the detector to changes in hydrogen index, the mock rock testbed discussed in previous chapters was constructed within the D-T neutron facility, with the detector placed directly on top of the moderator material. A custom aluminium frame (see Figure 6.18) was constructed of 135 × 80 × 90 cm to hold large volumes of material analogous to those encountered in logging scenarios. This is the same setup that was simulated in the GEANT4 simulations in chapter 3, which is expected to be large enough to produce a measurable detector response for detector studies. The testbench was placed into position at the rear of the neutron generator room, in line with the DT PNG. The setup is shown in Figure 6.19. The container was then filled completely with over 1.2 tonnes builders sand, and instrumented with TEROS moisture sensors for continuous monitoring. The filled box is shown in Figure 6.20.

A large quantity of builders sand was used to fill the container as in simulations. It was planned to add water to the sand to increase the hydrogen content and elicit a detector response, replicating the simulations from earlier chapters. The sand that was delivered however had significant moisture content. In these tests, due to limitations

Figure 6.18: Aluminium box constructed to hold variable water content sand volume.

Figure 6.19: Aluminium box in position at rear of generator room.

Figure 6.20: Filled aluminium box containing over 1.2 tonnes of builders sand.

on the source activity and possible runtimes, it was required to work within the 0 to 0.08 range, before the response to hydrogen index plateaued as in simulations. With a higher activity detector, it may well be possible to use this detector to probe higher moisture regions, but within the capabilities of the DT PNG at Sheffield, 0 to 0.08 was the ideal range for planned tests. The delivered sand arrived well above this hydrogen content range. Attempts were made to dry the sand, but due to the volume this was ultimately unsuccessful, preventing the originally planned tests. Given time constraints, as an alternative, tests were performed with a completely filled and a partially filled test container, to show extreme differences in detector response. This experiment aims to demonstrate that with a larger volume of sand, the detector begins to observe an increase in neutron counts on account of the presence of moderating material in the presence of a DT source. This would show a viable demonstration that this detector is suitable for detection of neutrons (and gammas) from a DT PNG source after moderation from an external environment. Future source upgrades may allow for further testing and development of this detector setup, following these initial demonstrations of viability. This is a limited demonstration, assuming homogeneous distribution of water throughout the sand. It is more likely that the water collects closer to the bottom of the container, however the sand sample used was collected from different patches of sand, and so one would assume a representative, averaged hydrogen index.

6.3.1 Experimental Testing

The filled sand container and partially emptied sand container were both tested with the detector placed on top of the custom aluminium frame. In both cases, a lower time cut of 100 μs was applied to remove pileup. Counts were scaled according to calibration factors calculated in the previous section.

Tests were performed with the DT generator to explore the detector response. With the generator running, an hour-long run was taken using a full container with sand of hydrogen index 0.155, which was calculated using a drying method from a sample of sand taken from the test pit. Sand was then removed from the pit to a depth of 60 cm. The detector remained in its original position, on top of the aluminium container which holds the sand. A detector run was performed with this reduced volume of sand. In each case the DT PNG was run using the same operating conditions (505 °C and 505 V).

6.3.2 Detector Response

The plot in Figure 6.23 shows the distribution of neutron counts in each detector for the experimental tests. In all detectors, higher count rates were recorded in the case of the filled sand container. Detector 1 shows the highest counts in both cases, and the distribution of counts across detectors follows the same general trend in each case. Detector 1 having the largest neutron count rate suggests that this detector is closest to the average slowing down length of DT neutrons with this geometry configuration. This effect is pronounced in the case of a filled box. This demonstrates an increase in counts with the presence of additional moderating material, as a demonstration of the detectors response to external moderator with a DT PNG source. Count rate drops off significantly in detectors 2 and 3, as fewer neutrons reach far detectors. Detector 0 sees fewer events than Detector 1, as fewer DT neutrons are able to reach thermal energies in this shorter distance. PSD plots across all four detectors in each setup are shown in Figure 6.21 and Figure 6.22.

Figure 6.24 shows the distribution of gamma counts in each detector. Again, higher count rates are observed in the filled test container case overall. There is a significant dip in the detected gammas in detector 1, before gamma counts rise again significantly in detector 2.

The mean detection time of neutrons in the filled container was $638\,\mu s \pm 23\,\mu s$ compared with $730\,\mu s \pm 21\,\mu s$. The filled container, with more hydrogen present in water, appeared to slow neutrons to thermal energies more quickly for detection in the converter foils.

Figure 6.25 shows simulated data for both 60 cm and 90 cm height test formations, showing the neutron counts as a proportion of simulated neutrons. These setups are roughly analogous to the final tests performed in the testbench, as shown in Figure 6.23 and Figure 6.24. The simulation data is for a formation with a hydrogen index of 0.16, compared with 0.155 (measured based on a dried sand sample). In simulated data, the count rate distribution across detectors differs from the experimental setup. Simulations predict a very high count rate in the first detector, closest to the source. Experimentally, a slightly lower count rate was observed in detector 0 compared with detector 1, the next closest detector to the source. There are several potential reasons for this disparity. The most likely reason for this is an oversimplification in the simulation geometry compared with the experimental setup. The simulation geometry assumes a mostly homogeneous stack of moderator material, but as is visible in Figure 6.20, there are more complicated

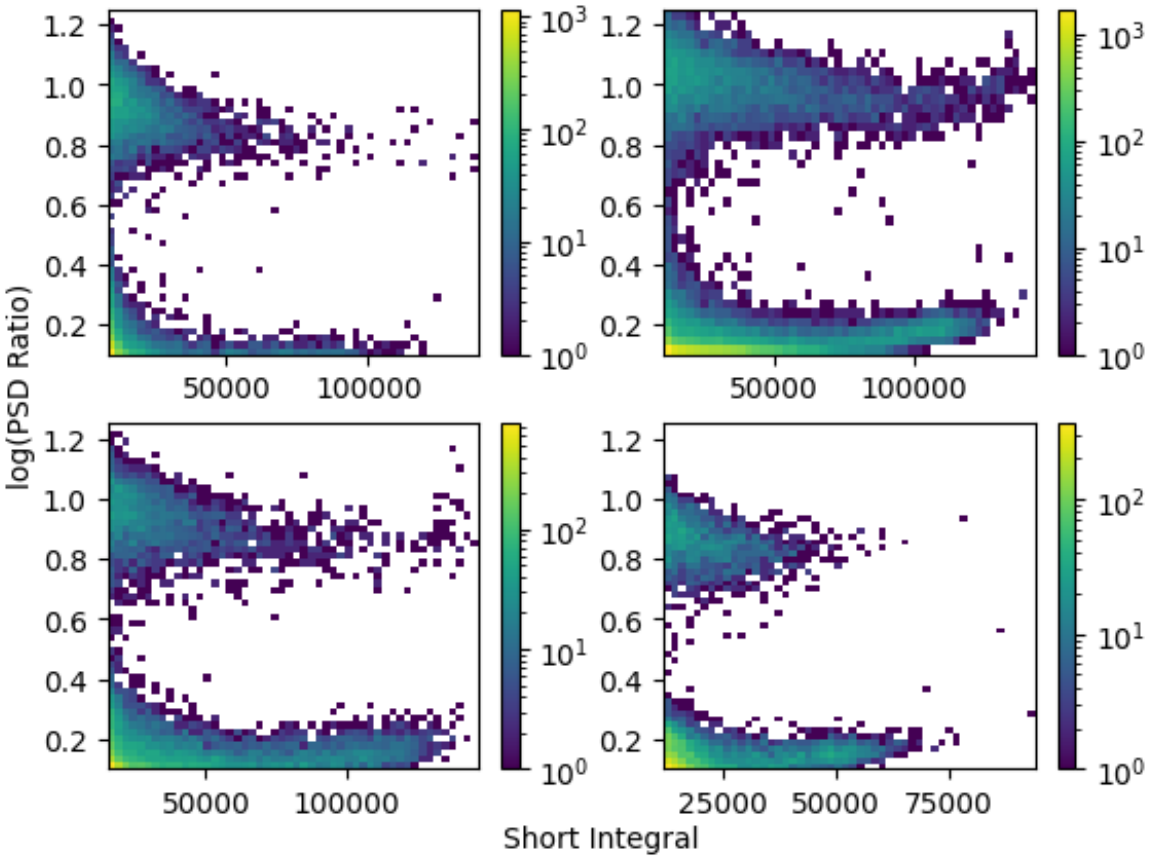

Figure 6.21: PSD plots for detectors 0 to 3, for the case of a filled test container.

geometries present in the shielding. This could lead to channeling of neutrons away from detector 0, and unpredictable neutron scattering. Additionally, it was noticed during filling of the box with additional water that it had a tendency to pool at the bottom of the container. This could mean that in the experimental case, neutrons are actually able to travel further before being thermalised in the sand, on account of lower moisture contents in the upper sections of the sand. An alternative method of experimentally producing homogeneous materials of known hydrogen content may instead choose to opt for high density polyethylene beads dispersed in sand. This would be less likely to separate, and could potentially produce more reliable experimental results.

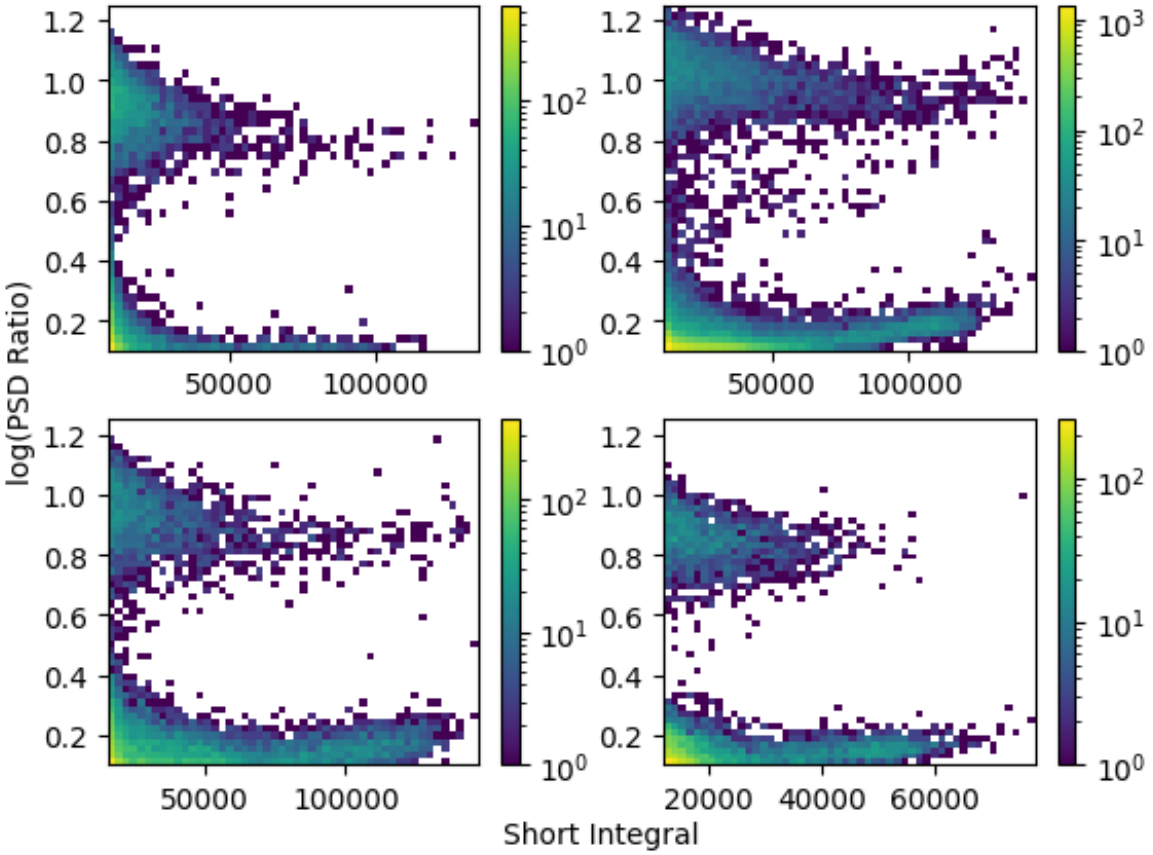

Figure 6.22: PSD plots for detectors 0 to 3, for the case of a partially filled test container filled up to a height of 60 cm.

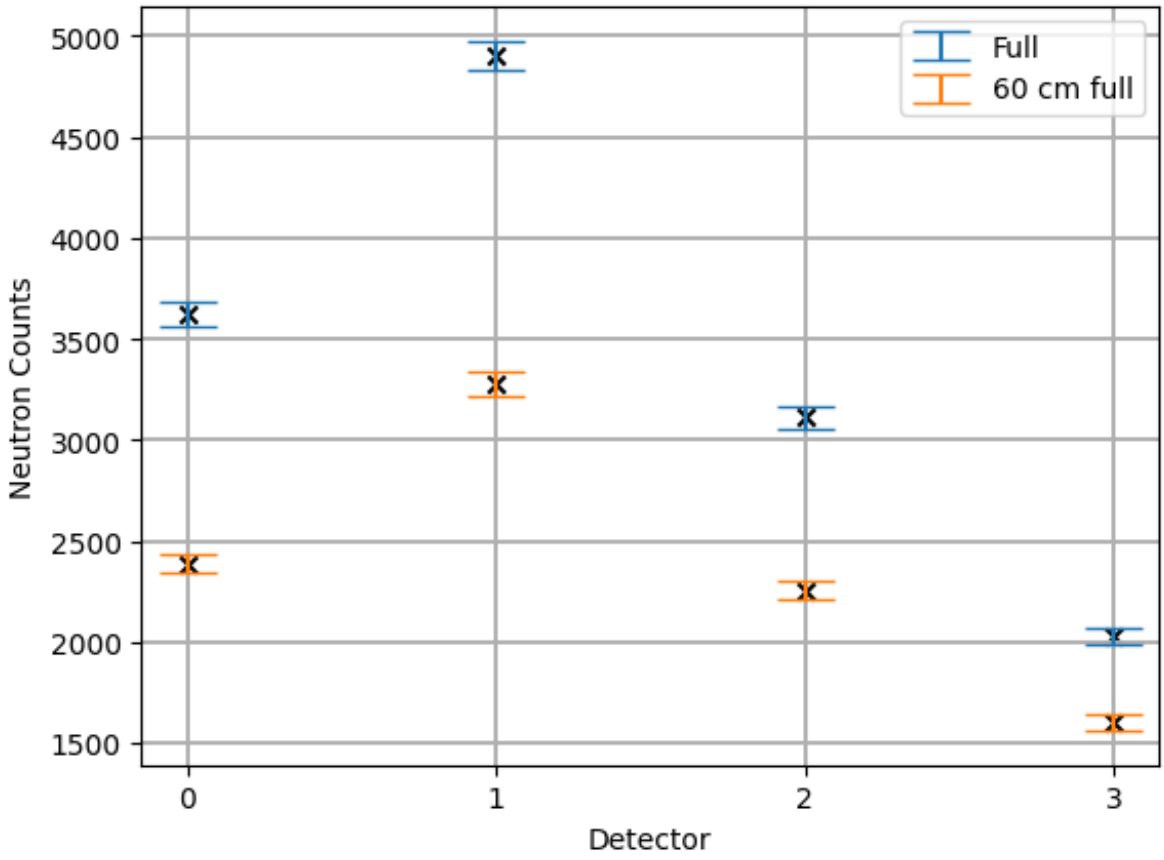

Figure 6.23: Neutron counts across all four detectors with a filled and 60 cm filled sand container.

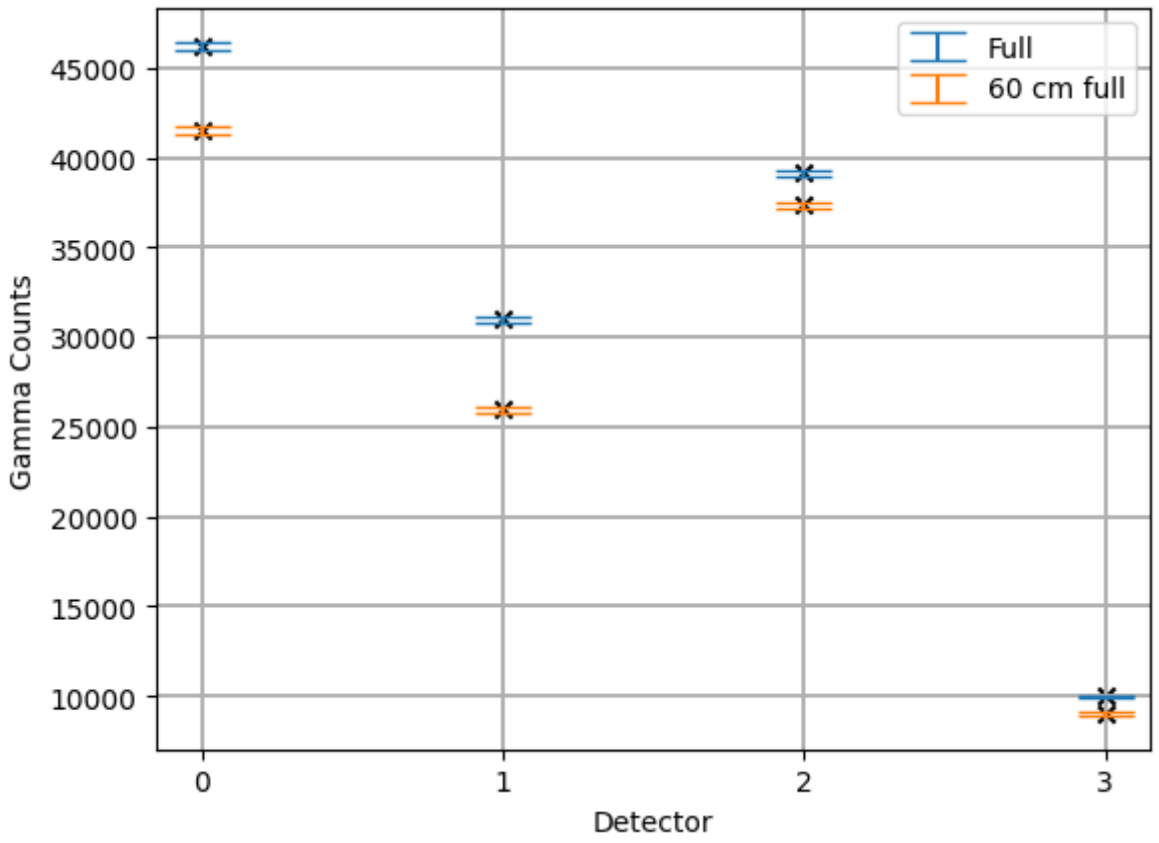

Figure 6.24: Gamma counts across all four detectors with a filled and 60 cm filled sand container.

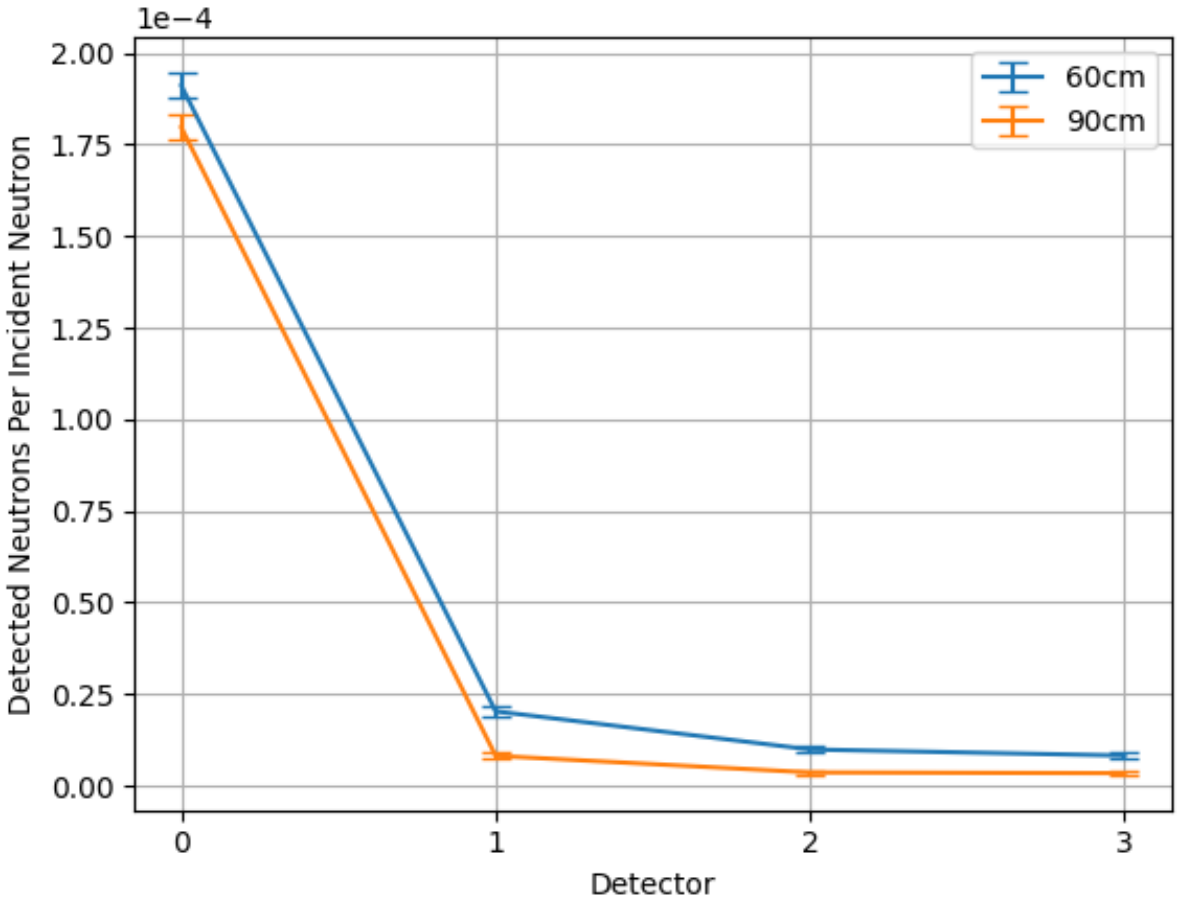

Figure 6.25: Neutron counts per incident neutron for simulated setup with 60cm and 90cm filled containers. There is a disagreement with experimental data, likely due to inhomogeneity in the hydrogen distribution.

6.3.3 Chapter Summary

In this chapter, the construction, characterisation, and calibration of a prototype detector was discussed, based on in-house manufactured low-cost detectors. The detector shows good neutron-gamma discrimination in all detector modules, forming a mixed-field detector with four-position sensitivity and event timestamping relative to a PNG pulse. Initial plans to test the detector in a sensitive range of hydrogen indices was not possible, and so alternative tests were performed to demonstrate the detector response to a modified test container. In summary:

- A four-detector system was constructed, with four low-cost detector modules made from plastic scintillator wrapped in BN-based thermal neutron converter foils.
- PMT gains were calibrated, and efficiency calibration factors calculated from data taken with a Cf-252 source.
- All detectors demonstrate good figures of merit for PSD, provided a suitable short integral cut is applied.
- Original plans to test the detector over a low to high hydrogen index range were not possible, on account of the builders sand in the test sand having a hydrogen index outside of ideal range. Efforts to dry the sand failed due to the large volume of sand required.
- Instead, more rudimentary tests were performed using the available test stand with filled and partially filled containers.
- These configurations were tested with the DT PNG. The experimental tests demonstrated a difference in response in terms of overall detector counts and time distributions.
- Simulated results showed disagreement with the experimental results, likely due to inhomogeneity of hydrogen within the sand, and resulting inaccuracies in the simulation geometry. Future work should aim to use a different method of simulating materials of varying hydrogen contents, perhaps through the use of HDPE beads or alternatives.

Chapter 7

Concluding Remarks

In this work, a prototype borehole detector was constructed, capable of mixed-field detection using low-cost materials. This detector was designed based on the results of optical simulations which hoped to produce a highly segmented detector with fibre readout. This was shown through GEANT4 simulations to be unfeasible in the demonstrated configuration due to poor light collection on coupled fibres, and resulting misclassification of particles using PSD. Though other designs could potentially improve the PSD performance (larger fibres or alternative geometrical configurations) this work chose to focus on low-cost mixed-field detector modules directly coupled to PMTs. The PSD optimisation and prediction code was developed to work in tandem with CRESTA/GEANT4 to produce realistic PMT pulses based on optical data, and response data for target photosensors. It is believed that this code could be of use in future for the development or feasibility testing of novel detector configurations for PSD. This set of simulations informed on the selection of directly coupled mixed-field detectors for this work. These detector modules were cast from in-house manufactured scintillator made from low-cost epoxy base material and easily available fluorophores. The overall cost of this scintillator mixture was shown to be competitive with existing scintillation cocktails from well-established manufacturers. The cast detector modules, when coupled to (BN)-based converter foils, show the capability to detect mixed radiation fields with good PSD performance at very low cost. The manufacturing procedure is reported here for use in other work, which may have applications in fast prototyping of scintillation detectors. These detector modules were then constructed as part of a four-detector borehole system for use with a DT PNG, though they could have applications in any area of radiation

detection requiring neutron and gamma sensing at low-cost. This four-detector system was shown to be capable of measuring the positional and temporal distribution of radiation following a DT neutron pulse. Complications are present in the immediate time following a neutron pulse from the generator. Pileup complications were explored and found to significantly hinder PSD at early times. Though alternative detectors may be capable of avoiding these effects, in this case it was necessary to apply a holdoff time before acceptable PSD performance is attainable. ZnS has a long pulse train and for the convolution of many pileup pulses this requires a significant holdoff. A sand-based testbench was simulated and constructed in attempts to replicate a borehole formation scenario based on simulations in chapter 3. Unfortunately issues were encountered in the control of moisture in the test material. Future attempts to create test pits may have more success with a more sophisticated method of controlling moisture content in the material. In this work the goal was to test with the on-site source at the University of Sheffield pulsed neutron facility, but sophisticated test pits are used by major logging companies. Despite issues with the test formation, the construction and testing of the detector demonstrated its ability to detect neutrons and gammas over four detectors with DT pulse-relative timestamping. This suggests that a mixed-field detector could be constructed at lower-cost for formation evaluation applications, though further testng is required to ensure ruggedisation for particular extremes encountered in the borehole environment. Photomultipliers have already been deployed in harsh environments for many years, with ruggedised PMTs sold by major manufacturers to stand up to the high temperature and high vibration environments present in drilling operations. As mentioned, new organic scintillators are in development such as polysiloxanes, which are suitable for use at much higher temperatures than conventional plastics. Future work may also consider coupling boron-based capture foils to spectroscopic scintillators. Though this may require further development and tuning of PSD algorithms, it is possible that spectroscopic measurements could be made within a mixed-field detector, allowing for the combination of other existing measurements into one mixed-field tool.

Bibliography

[1] N. J. Hyne, *Nontechnical Guide to Petroleum Geology - pennwell books*, 3rd ed. (2012).

[2] Statista, *Global crude oil demand 2023*, www.statista.com/statistics/271823/global-crude-oil-demand.

[3] SLB, *Wildcat - Energy Glossary*, glossary.slb.com/terms/w/wildcat.

[4] SLB, *1920s: The First Well Log*, www.slb.com/about/who-we-are/our-history/1920s.

[5] B. Pike and R. Duey, *Logging History Rich with Innovation*, (2002) https://www.spwla.org/documents/spwla/Logging-History.pdf.

[6] L. Allaud and M. Martin, *Schlumberger: the history of a technique*, A Wiley-Interscience publication (Wiley, 1977).

[7] G. Asquith et al., *Basic well log analysis* (American Association of Petroleum Geologists, January 2004).

[8] H. M. Johnson, "A history of well logging", GEOPHYSICS **27**, 507–527 (1962).

[9] T. Huang et al., "Radioactivity of Soil, Rock and Water in a Shale Gas Exploitation Area, SW China", Water **9**, 299 (2017).

[10] B. Pontecorvo, *Neutron well logging*, (1941) archive.org/details/sim_oil-gas-journal_1941-09-11_40_18/page/32/mode/1up.

[11] G. Knoll, *Radiation detection and measurement* (Wiley, 1980), p. 71.

[12] W. Wu et al., "Porosity sensitivity study of the compensated neutron logging tool", Journal of Petroleum Science and Engineering **108**, 10–13 (2013).

[13] D. V. Ellis and J. M. Singer, "Basic neutron physics for logging applications", in *Well Logging for Earth Scientists* (Springer Netherlands, Dordrecht, 2007), pp. 325–349.

[14] Z. Bassiouni, *Theory, Measurement, and Interpretation of Well Logs*, SPE textbook series (Henry L. Doherty Memorial Fund of AIME, Society of Petroleum Engineers, 1994).

[15] S. A. Murawski et al., "Deepwater oil and gas production in the gulf of mexico and related global trends", in *Scenarios and responses to future deep oil spills: fighting the next war*, edited by S. A. Murawski et al. (Springer International Publishing, Cham, 2020), pp. 16–32.

[16] A. Nikitin and S. Bliven, "Needs of well logging industry in new nuclear detectors", in (October 2010), pp. 1214–1219.

[17] D. M. Dana A. Shea, *The Helium-3 Shortage: Supply, Demand, and Options for Congress*, R41419 (2011).

[18] N. Kawaguchi et al., "Temperature dependence of scintillation responses in rare-earth-ions-doped LiCaAlF6 single crystals", Nuclear Instruments and Methods in Physics Research Section A: Accelerators, Spectrometers, Detectors and Associated Equipment **954**, Symposium on Radiation Measurements and Applications XVII, 161518 (2020).

[19] NRC.gov, *Collection of Source Abandonment Reports*, (2018) `https://www.nrc.gov/docs/ML1802/ML18029A090.pdf`.

[20] J. Beyer et al., "Environmental effects of the deepwater horizon oil spill: a review", Marine pollution bulletin **110**, 28–51 (2016).

[21] W. J. Dircks, *SECY-81-516: Risk Analysis for Previously Abandoned Well-Logging Sources*, 1981.

[22] C. Park and M. Allaby, *A Dictionary of Environment and Conservation* (Oxford University Press, January 2013).

[23] P. Hernandez, "Notification of source abandonment", Halliburton Energy Services (2019).

[24] U. C. Mishra and A. S. Pradhan, *Loss and Recovery of XA9949014 Radiation Sources in India*, `https://inis.iaea.org/records/n3bem-vv145/files/30008061.pdf?download=1`.

[25] *Hazmat General Warning - Australian Emergency Warning, Lost Cs-137 Capsule*, https://ia601602.us.archive.org/32/items/hazmat-radioactive-capsule-emergency-wa-27-jan-2023_202301/HAZMAT%20-%20Radioactive%20Capsule%20-%20Emergency%20WA%20-%2027Jan2023.pdf.

[26] C. Ho and A. Searson, *Abc news - prime minister slams 'ridiculously low' penalty for mishandling radioactive material*, https://www.abc.net.au/news/2023-02-01/anthony-albanese-lost-radioactive-capsule-western-australia/101915640.

[27] *The Ionising Radiations Regulations 2017 - Schedule 3*, https://www.legislation.gov.uk/uksi/2017/1075/contents.

[28] *IAEA Safety Standards for protecting people and the environment Specific Safety Guide No. SSG-57 Radiation Safety in Well Logging*, https://www.iaea.org/resources/safety-standards.

[29] H. Rosoff and D. Von Winterfeldt, "A Risk and Economic Analysis of Dirty Bomb Attacks on the Ports of Los Angeles and Long Beach", Risk Analysis **27**, 533–546 (2007).

[30] *QSA Global Well Logging Sources (AmBe)*, https://www.qsa-global.com/ambe-neutron-sources-owl.

[31] C. Frankle and G. Dale, "Unconventional neutron sources for oil well logging", Nuclear Instruments and Methods in Physics Research Section A: Accelerators, Spectrometers, Detectors and Associated Equipment **723**, 24–29 (2013).

[32] A. Badruzzaman, A. Schmidt, and A. Antolak, "Neutron generators as alternatives to am-be sources in well logging: an assessment of fundamentals", Petrophysics - The SPWLA Journal of Formation Evaluation and Reservoir Description **60**, 136–170 (2019).

[33] A. Chen, A. Antolak, and K.-N. Leung, "Electronic neutron sources for compensated porosity well logging", Nuclear Instruments and Methods in Physics Research Section A: Accelerators, Spectrometers, Detectors and Associated Equipment **684**, 52–56 (2012).

[34] *Alternative Technologies for Radiation Sources for Well Loggers* (Nuclear Security Science Network, AWE, 2018).

[35] *Ruggedized High Temperature Photomultiplier Tubes*, https://www.hamamatsu.com/content/dam/hamamatsu-photonics/sites/documents/99_SALES_LIBRARY/etd/High_temp_PMT_TPMH0004E.pdf.

[36] A. Mozhayev et al., *A Fission-like Neutron Spectrum Shaping Assembly based on D-T Generator*, en, tech. rep. PNNL–34339, 1987308 (June 2023).

[37] *Radiation Protection Glossary - AmBe neutron source*, en-GB, https://ionactive.co.uk/resource-hub/glossary/ambe-americium-beryllium-neutron-source (visited on March 22, 2024).

[38] R. Burkhart, "Neutron generators and well logging.", (2006).

[39] J. Arrue et al., "Impact of temperature on light yield and pulse shape discrimination of polysiloxane-based organic scintillators formulated with commercial resins", Nuclear Instruments and Methods in Physics Research Section A: Accelerators, Spectrometers, Detectors and Associated Equipment **1056**, 168650 (2023).

[40] *EJ-244, EJ-248 - High Temperature Plastic Scintillators - Eljen Technology*, https://eljentechnology.com/products/plastic-scintillators/ej-244-ej-248-ej-244m-ej-248m (visited on March 19, 2024).

[41] S. M. Carturan et al., "Flexible scintillation sensors for the detection of thermal neutrons based on siloxane 6lif containing composites: role of 6lif crystals size and dispersion", Nuclear Instruments and Methods in Physics Research Section A: Accelerators, Spectrometers, Detectors and Associated Equipment **925**, 109–115 (2019).

[42] Epic-Crystal, *Epic-Crystal - Bismuth Germanate*, (2024) https://www.epic-scintillator.com/BGO-crystal-scintillator.

[43] N. J. Carron, *An introduction to the passage of energetic particles through matter* (CRC Press, 2006).

[44] R. M, *Neutron Cross-Sections, Lecture Notes*, https://mragheb.com/NPRE%20402%20ME%20405%20Nuclear%20Power%20Engineering/Neutron%20Cross%20Sections.pdf.

[45] G. Mauri et al., "Fast neutron sensitivity for 3he detectors and comparison with boron-10 based neutron detectors", EPJ Techniques and Instrumentation **6**, 10.1140/epjti/s40485-019-0052-x (2019).

[46] J. E. Turner, *Atoms, radiation, and radiation protection* (Wiley, May 2007), p. 217.

[47] P. Rinard, *Neutron Interactions with Matter*, `https://sgp.fas.org/othergov/doe/lanl/lib-www/la-pubs/`.

[48] T. Gozani, "Principles and Applications of Neutron-based Inspection Techniques",

[49] *Database of Prompt Gamma Rays from Slow Neutron Capture for Elemental Analysis*, Non-serial Publications (INTERNATIONAL ATOMIC ENERGY AGENCY, Vienna, 2007).

[50] T. D. Malouff et al., "Boron neutron capture therapy: a review of clinical applications", Frontiers in Oncology **11**, `10.3389/fonc.2021.601820` (2021).

[51] C. Zhou et al., "Neutron detection performance of gallium nitride based semiconductors", en, Scientific Reports **9**, Publisher: Nature Publishing Group, 17551 (2019).

[52] J. Hearst and P. Nelson, *Well Logging for Physical Properties* (McGraw-Hill, 1985).

[53] P. W.J Glover, *MSc Petroleum Geology Course Notes* (University of Aberdeen, September 2000).

[54] *Reservoir Performance Monitor service - Baker Hughes*, `https://www.bakerhughes.com/evaluation/wireline-casedhole-logging/casedhole-formation-evaluation-services/reservoir-performance-monitor-service` (visited on March 28, 2024).

[55] S. Zaker et al., "Prediction of new perforation intervals in a depleted reservoir to achieve the maximum productivity: a case study of pnn logging in a cased-well of an iranian oil reservoir", Petroleum **6**, 170–176 (2020).

[56] J. G. Szűcs and L. Balázs, "Sensitivity study of C/O logging measurements by Monte Carlo method", Applied Radiation and Isotopes **188**, 110400 (2022).

[57] H. Tan et al., "A digital spectrometer approach to obtaining multiple time-resolved gamma-ray spectra for pulsed spectroscopy", Nuclear Instruments and Methods in Physics Research Section B: Beam Interactions with Materials and Atoms **263**, Industrial Radiation and Radioisotope Measurement Applications, 63–66 (2007).

[58] F. D. Amaro et al., "Novel concept for neutron detection: Proportional counter filled with 10 B nanoparticle aerosol", Scientific Reports **7**, 10.1038/srep41699 (2017).

[59] *Handbook of Chemistry and Physics*, v. 79, pts. 1998-1999; v. 80, pts. 1999-2000 (CRC Press).

[60] *AAAS Workshop Explores How to Meet Demand for Helium-3 in Medicine, Industry, and Security*, https://www.aaas.org/news/aaas-workshop-explores-how-meet-demand-helium-3-medicine-industry-and-security (visited on April 12, 2024).

[61] *BF3 Counter Tubes Proportional Counter Tubes*, en, https://www.mirion.com/products/technologies/reactor-instrumentation-control/neutron-flux-monitoring-systems/in-core-ex-core-neutron-flux-detectors/bf3-counter-tubes (visited on April 5, 2024).

[62] P. Egelstaff, "Glass scintillators for prompt detection of intermediate energy neutrons", Nuclear Instruments **1**, 197–199 (1957).

[63] *GS20 Scintacor - Li6 doped glass*, https://scintacor.com/technologies/neutrons/.

[64] *EJ-276D - Pulse Shape Discrimination Plastic Scintillator - Eljen Technology*, https://eljentechnology.com/products/plastic-scintillators/ej-276 (visited on April 5, 2024).

[65] *Gamma-Neutron Scintillator Properties - CLLBC*, (2024) https://www.rmdinc.com/product-category/products/cllbc-gamma-neutron-scintillator/.

[66] *CLYC:Ce Gamma/Neutron Scintillators, Radiation Detection - Berkeley Nucleonics*, https://www.berkeleynucleonics.com/clycce (visited on April 12, 2024).

[67] *NaIL Scintillation Crystals - Crystals*, en, https://www.luxiumsolutions.com/radiation-detection-scintillators/crystal-scintillators/nail-scintillation-crystals (visited on April 12, 2024).

[68] *EJ-600 - ZnS:Ag Phosphor Powder - eljen technology*, https://eljentechnology.com/products/zinc-sulfide-coated/ej-600 (visited on April 12, 2024).

[69] A. C. Stephan et al., "Modelling of composite neutron scintillators", Radiation Protection Dosimetry **116**, 165–169 (2005).

[70] E. Marsden, "Large area thermal neutron detectors for security applications" (University of Sheffield, 2016).

[71] *MSE PRO Hexagonal Boron Nitride 1-2 micron*, (2024) `msesupplies.com`.

[72] Merck, *Enriched LiF Powder*, (2024) `https://www.sigmaaldrich.com/GB/en/product/aldrich/601411`.

[73] L. Swiderski et al., "Measurement of Compton edge position in low-Z scintillators", Radiation Measurements **45**, Proceedings of the 7th European Conference on Luminescent Detectors and Transformers of Ionizing Radiation (LUMDETR 2009), 605–607 (2010).

[74] P. D'Alessandris, *Spiral Modern Physics* (LibreTexts Libraries).

[75] D. D. Patton, "Roentgen and the "new light" - roentgen's moment of discovery part 3: the genealogy of roentgen's barium platinocyanide screen", Investigative Radiology **28**, 954–961 (1993).

[76] *Lanthanum Bromide Scintillation Detector, Berkeley Nucleonics*, `https://www.berkeleynucleonics.com/lanthanum-bromide`.

[77] B. Löher et al., "High count rate gamma-ray spectroscopy with labr3:ce scintillation detectors", Nuclear Instruments and Methods in Physics Research Section A: Accelerators, Spectrometers, Detectors and Associated Equipment **686**, 1–6 (2012).

[78] A. Iltis et al., "Lanthanum halide scintillators: properties and applications", Nuclear Instruments and Methods in Physics Research Section A: Accelerators, Spectrometers, Detectors and Associated Equipment **563**, TRDs for the Third Millenium, 359–363 (2006).

[79] M. J. Weber, "Inorganic scintillators: today and tomorrow", Journal of Luminescence **100**, 35–45 (2002).

[80] G. Bizarri, "Scintillation mechanisms of inorganic materials: from crystal characteristics to scintillation properties", Journal of Crystal Growth **312**, The 17th American Conference on Crystal Growth and Epitaxy/The 14th US Biennial Workshop on Organometallic Vapor Phase Epitaxy/The 6th International Workshop on Modeling in Crystal Growth, 1213–1215 (2010).

[81] T. J. Hajagos et al., "High-Z Sensitized Plastic Scintillators: A Review", en, Advanced Materials **30**, 1706956 (2018).

[82] E. Horszczaruk, P. Sikora, and P. Zaporowski, "Mechanical properties of shielding concrete with magnetite aggregate subjected to high temperature", Procedia Engineering **108**, 39–46 (2015).

[83] S. Agostinelli et al., "Geant4—a simulation toolkit", Nuclear Instruments and Methods in Physics Research Section A: Accelerators, Spectrometers, Detectors and Associated Equipment **506**, 250–303 (2003).

[84] C. Steer, P. Stowell, and L. Thompson, "CRESTA: Cosmic rays for engineering, scientific, and technology applications", `https://gitlab.com/cosmicraysim/cresta`.

[85] *SLB Energy Glossary, available at: https://glossary.slb.com/*, `https://glossary.slb.com/`.

[86] R. Smith et al., "A novel, low-cost, position-sensitive neutron detector to support thick-target inverse kinematics experiments for nuclear data measurements", Universe **9**, `10.3390/universe9060274` (2023).

[87] *BCF-91A - wavelength shifting fibres*, `https://www.phys.hawaii.edu/~idlab/taskAndSchedule/HMBv3/fiber-product-sheet.pdf`.

[88] *EJ-200 - Eljen Technology*, `https://eljentechnology.com/products/plastic-scintillators/ej-200-ej-204-ej-208-ej-212` (visited on April 12, 2024).

[89] *Hamamatsu h8711 multi-anode pmt*, `https://www.hamamatsu.com/jp/en/product/optical-sensors/pmt/pmt-assembly/metal-package-type/H8711.html`.

[90] *OMLC Spectra, POPOP Emission Spectrum*, `https://omlc.org/spectra/PhotochemCAD/data/020-ems.txt`.

[91] R. D. Breukers, C. M. Bartle, and A. Edgar, "Transparent lithium loaded plastic scintillators for thermal neutron detection", Nuclear Instruments and Methods in Physics Research Section A: Accelerators, Spectrometers, Detectors and Associated Equipment **701**, 58–61 (2013).

[92] S. Piatek, *How does temperature affect the performance of an SiPM?*, (2017) https://hub.hamamatsu.com/us/en/technical-notes/mppc-sipms/how-does-temperature-affect-the-performance-of-an-SiPM.html.

[93] *9954B Series PMT - ET Enterprises, formerly EMI*, https://et-enterprises.com/products/photomultipliers/product/p9954b-series.

[94] Y. Yamashina et al., "Development of a cost-effective plastic scintillator for cosmic-ray muon radiography of a volcano", en, Earth, Planets and Space **62**, Number: 2 Publisher: SpringerOpen, 173–177 (2010).

[95] *GlassCast50 Clear Epoxy Casting Resin*, https://www.easycomposites.co.uk/glasscast-50-clear-epoxy-casting-resin.

[96] *EJ-290 Scintillator Casting Resin - Eljen Technology*, https://eljentechnology.com/products/plastic-scintillators/ej-290 (visited on April 12, 2024).

[97] *Fisher Scientific*, https://www.fishersci.co.uk/gb/en/home.html (visited on April 12, 2024).

[98] *Shimadzu UV-2700i*, https://www.shimadzu.com/an/products/molecular-spectroscopy/uv-vis/uv-vis-nir-spectroscopy/uv-2600i-uv-2700i/index.html.

[99] H. Schneckenburger, "Förster resonance energy transfer-what can we learn and how can we use it?", eng, Methods and Applications in Fluorescence **8**, 013001 (2019).

[100] A. Yilmaz et al., "Towards a better understanding of detection properties of different types of plastic scintillator crystals using physical detector and mcnpx code", Nuclear Engineering and Technology **54**, 4671–4678 (2022).

[101] *NSD Fusion Manual - Internal Document, University of Sheffield.*

[102] R. Bonomo, *Inertial electrostatic confinement fusion*, (2007) https://iec.neep.wisc.edu/operation.php.